Drying behaviour of ceramic green bodies : experimental characterization and numerical modelling

Siham Oummadi

UNIVERSITÉ DE LIMOGES

École doctorale n ° 609 : Sciences et Ingénierie des Matériaux, Mécanique, Energétique - SIMME

Institut de Recherche sur les Céramiques (IRCer)

Thèse

pour obtenir le grade de

DOCTEUR DE L'UNIVERSITÉ DE LIMOGES

présentée et soutenue par

Siham OUMMADI

le 16 décembre 2019

Drying behaviour of ceramic green bodies: experimental characterization and numerical modeling

Thèse dirigée par David Stanley SMITH

Benoit NAIT-ALI et Arnaud ALZINA

JURY :

Friedrich RAETHER	Directeur de recherche, Fraunhofer-Institut für Silicatforschung ISC	Rapporteur
Didier BOUVARD	Professeur, Grenoble INP-SIMAP	Rapporteur
Alexis BÉAKOU	Professeur, SIGMA Clermont	Examinateur
Fabienne PENNEC	Maitre de conférences, Université Clermont-Auvergne	Examinateur
David Stanley SMITH	Professeur, IRCer, ENSIL-ENSCI	Examinateur
Benoit NAIT-ALI	Maitre de conférences, IRCer, ENSIL-ENSCI	Examinateur
Arnaud ALZINA	Maitre de conférences, IRCer, IUT Limousin	Examinateur

Contents

Symbols

X	moisture content on dry basis
X'	moisture content on wet basis
w	sample weight in g
w_d	dry sample weight in g
w_{init}	initial weight of the sample in g
RH	relative humidity
T	temperature in K
T_w	wet temperature in K
T_{air}	air temperature in K
T_s	surface temperature in K
P_v	partial pressure of the water vapour in Pa
p_s	saturated vapour pressure of water in Pa
q	heat flux in $W\ m^{-2}$,
J_L	flux of the liquid in units of volume per unit area per unit time in $m\ s^{-1}$
D	permeability in m^2
η_L	viscosity of the liquid in $Pa\ s$
P_L	force per unit area of the liquid in Pa
J_D	diffusion flux in $mol\ m^{-2}\ s{-}1$
D_w	diffusion coefficient in $m^2\ s^{-1}$
C	concentration of water in $mol\ m^{-3}$
$C_{s-b.l}$	water vapour concentration just above the surface in $mol\ m^{-3}$
C_{air}	water vapour concentration in the air in $mol\ m^{-3}$
$C_{b.l}$	water vapour concentration in the boundary layer in $mol\ m^{-3}$
k	mass transfer coefficient in $m\ s^{-1}$
a_w	water activity
ϕ_c	evaporation rate in $g\ m^{-2}\ s^{-1}$
ϕ_{C-exp}	experimental drying rate per unit area in $g\ m^{-2}\ s^{-1}$
ϕ_{C-anal}	analytical drying rate per unit area in $g\ m^{-2}\ s^{-1}$
R	ideal gas constant in $J\ mol^{-1}\ K^{-1}$
h	heat transfer coefficient in $W\ m^{-2}\ K^{-1}$
M_w	water molar mass in $g\ mol^{-1}$
L_w	latent heat of vaporization in $J\ kg^{-1}$
C_p	heat capacity in $J\ kg^{-1}\ K^{-1}$
Cp_{air}	air heat capacity in $J\ kg^{-1}\ K^{-1}$
Cp_{water}	water heat capacity in $J\ kg^{-1}\ K^{-1}$
Cp_{solid}	solid heat capacity in $J\ kg^{-1}\ K^{-1}$
Le_f	Lewis number
P	capillary pressure in Pa
γ	liquid/vapour interfacial energy

R_c	curvature radius of the meniscus
Sh	linear shrinkage
L	sample length in cm
L_d	sample length at the end of drying in cm
S	surface area exposed to drying in m^2
t	drying time
$J_{x=0}$	outgoing water flux in $mol\ m^{-2}\ s^{-1}$
λ	thermal conductivity in $W\ m^{-1}\ K^{-1}$
λ_{eff}	effective thermal conductivity in $W\ m^{-1}\ K^{-1}$
λ_{water}	thermal conductivity of water in $W\ m^{-1}\ K^{-1}$
λ_{solid}	thermal conductivity of the solid in $W\ m^{-1}\ K^{-1}$
v_{solid}	volume fraction of solid
$\lambda_{solid\ matrix}$	solid matrix thermal conductivity in $W\ m^{-1}\ K^{-1}$
$\lambda_{second\ phase}$	second phase thermal conductivity in $W\ m^{-1}\ K^{-1}$
λ_{air}	thermal conductivity of air in $W\ m^{-1}\ K^{-1}$
λ_{grain}	thermal conductivity of a grain in $W\ m^{-1}\ K^{-1}$
ρ_{air}	air density in $kg\ m^{-3}$
ρ_{bulk}	bulk density in $kg\ m^{-3}$
ρ_{solid}	solid phase density in $kg\ m^{-3}$
v'_{air}	volume fraction of air
v_p	pore volume fraction
$R_{contact}$	thermal resistance in $m^2\ K\ W^{-1}$
Ω	domain of the wet body
$\partial\Omega$	boundary at the surface
C_{test}	test function of heat transfer
T_{test}	test function for the mass transfer

List of Figures

List of Tables

Introduction

Drying is a ubiquitous operation found in technological processes used in the pharmaceutical, paper, mineral, polymer, ceramic, textile, food and agricultural industries. Depending on the particular sector and quality criteria of products, drying will be managed in different ways by controlling its kinetics.

In the case of the ceramic industry, the drying step is necessary before firing ceramic bodies at high temperature. This step is complicated due to simultaneous and coupled heat and mass transfers, often accompanied by dimensional variations. It presents a permanent challenge for manufacturers mainly due to two aspects. First, it requires a significant consumption of energy. As an example, for manufacture of ceramic and building materials in France and the United Kingdom, 11% of energy consumption is due to the drying operation [1]. In this respect, according to the French law (number 2015-992) and various European directives, industry will be complied to reduce energy consumption by 50% before the end of 2050 [2]. The second important point is that mechanical stresses that occur within the material during drying may create damage in the final product if the drying conditions are not carefully chosen and controlled. It is worth mentioning here that most drying defects and cracks appear due to water removal and the body shrinkage. However this is not necessarily due to a poor choice of drying conditions, but also can be the result of other steps in the fabrication processes before drying such as, raw material selection, blending and shaping.

In the building industry, for fabrication of clay bricks for example, water (ranging between 15 and 30%) is added to aid forming the basic shape. Therefore, drying becomes a necessary step in order to obtain products containing 1 to 2% of residual moisture before final firing. In such a case, when drying conditions are not well controlled, several defects can be created. They are summarized in the table below with their likely causes [3]:

Defect	**Cause**
Warping	Condensation of moist air on cold bodies during initial drying
Cracks	High drying rate resulting large moisture gradients and heterogeneous shrinkage
micro-cracks	Unsuitable drying rate, too dry body before firing
Moisture spots on body surface	Lack of air stream to sweep away vapour in certain locations

Table 1: Defects related to the drying step for clay bricks [3].

In certain other ceramic fabrication techniques, the drying step can occur during the shaping method (tape casting, additive manufacturing) which makes the control of drying more complicated. As an example, in tape casting, continuous large sheets are produced by depositing a suspension on a supporting surface. Then because the tapes adhere physically to the support, evaporation takes place only at the upper surface and shrinkage occurs in the cross plane direction. Consequently, drying stresses occur and the probability of unwanted deformations, like edge cracks, warping or air bubbles, increases [4–6].

Investigating the physical drying phenomena in ceramic materials is then a necessity to optimize this step and obtain high quality samples for industrial applications while minimizing drying costs. In other words, one of the keys in development of ceramic processing is to improve the drying step. In this respect, real-time control systems offer potential since by monitoring drying parameters, they can detect abnormalities during the process and provide corrective action. Indeed, by controlling the wet product state in real time during drying, the drying air conditions (temperature, relative humidity and airflow rate) can be adjusted. Therefore, an appropriate selection of drying conditions should improve the quality of products and reduce operation time, thus saving energy.

Given this general motivation, the present work is based on two complimentary parts as summarized in the following chart diagram (figure 1). The first part deals with the measurement of the sample temperature, moisture content and dimension changes which are very important to determine the drying behaviour of ceramic green bodies in real time. Furthermore, the ultimate objective of the thesis work is to construct a robust numerical model of heat and mass transfer, that will be able to predict the drying behaviour of the ceramic green body. To this end, the model needs to inject realistic physical properties of the ceramic in the green state. These depend strongly on the moisture content. That is why a major part of this work is dedicated to an experimental study to identify the evolution of physical properties with water content and distribution as drying proceeds.

We focus the current study on two technologically important materials frequently used in the ceramic industry which are alumina and clays. Alumina is one of most common raw materials used in different domains, such as, abrasives, refractories, glass and advanced or technical ceramics. On the other hand, for traditional ceramic products, clay minerals like kaolin are typically used.

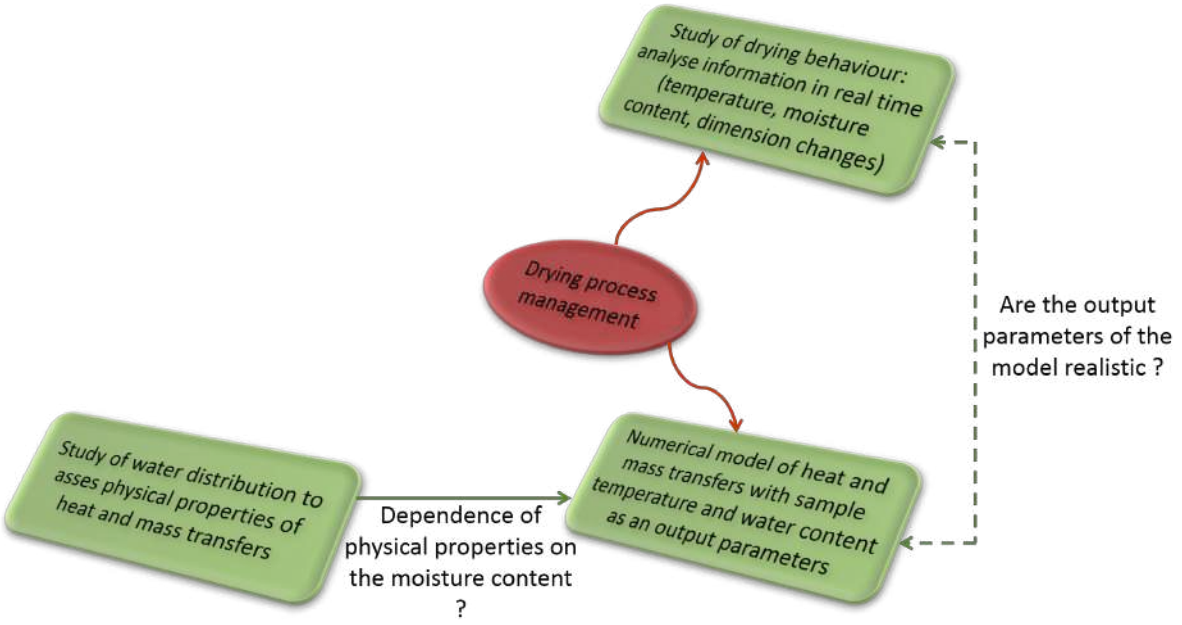

Figure 1: Schematic representation of the main topics examined in the current work.

This thesis is then organized as follows:

Chapter 1 reviews the state of art concerning drying of ceramic green bodies. First a reminder of the different water forms that can exist within a ceramic porous body and the mechanisms supplying heat to evaporate water are given. Then since drying is a coupling of heat and mass transfers, a mathematical description of heat and mass equations is made with particular emphasis on the involved physical properties. Based on this knowledge, the particular case of drying porous ceramic green bodies is examined through the mechanisms involved during the different stages including the initial shrinkage. Finally, the effect of certain parameters such as the material composition, external conditions, shape and size on the drying behaviour is reviewed.

In chapter 2, the raw materials used in this thesis (alumina, kaolin and montmorillonite) and their shaping method are first presented. Then, in order to characterize the macroscopic behaviour of our ceramic green bodies during drying: the drying rate, the sample temperature and the dimensional changes are measured. Furthermore, for more detail on the dimensional changes, an optical method based on tracking of marks was developed to characterize materials with possible anisotropic shrinkage.

The main objective of the experimental work, described in chapter 3, is to understand how the mechanisms of drying operate at different scales by using three different techniques to observe how the spatial distribution of water evolves with time. These are

simple mass measurements, magnetic resonance imaging and environmental scanning electron microscopy .

In chapter 4, the variations of certain physical properties as a function of moisture content are presented. First, water activity is assessed. Then based on results of chapter 3 the evolution of the diffusion coefficient for transport of water is estimated. After this, calculations of heat capacity as a function of moisture content are made. Then the evolution of the thermal conductivity of the ceramic green body during drying is presented and explained using the results of chapter 3.

After having studied experimentally the physical properties involved during drying, a numerical model, which takes into account the dependence of water diffusion coefficient, heat capacity, and thermal conductivity on moisture content is developed in chapter 5. This model based on coupling of heat and mass equations is solved using finite element method (FEM). Thus, in order to validate the numerical model, predictions are compared to the experimental results.

Chapter 1 :

General background: drying of ceramics

Chapter context

The purpose of this first chapter is to introduce the reader to the general state of the art concerning drying which has been established in the literature. In this respect, since we deal with wet products, it is instructive to start by examining the different forms of water that exist within a porous body and to describe the mechanisms supplying heat to evaporate water. Then the heat and mass transfers involved during drying are discussed more precisely. These transfers involve physical properties which depend strongly on moisture content. The role of water on the relevant physical properties is then discussed. Using this background, the particular case of drying porous ceramic green bodies is described through a series of stages related to the mechanisms involved. This insight into drying mechanisms helps to answer the questions as to how certain parameters such as, the material composition, external conditions, shape and size, can influence the drying behaviour.

1.1 General considerations

Except for a few methods, the fabrication of ceramic products, traditional or technical, requires forming the basic shape of the body with a solid/liquid paste or suspension. Therefore, removal of excess water within the body is necessary in order to obtain products which are sufficiently rigid for firing at high temperature. In certain production technologies, mechanical methods can be used to extract water from ceramic products before the firing step, e.g. centrifugation and filter-pressing. For our purposes, these methods will not be considered and the study will focus particularly on drying by supplying heat. In that case drying can be considered as the removal of water by evaporation.

Two forms of water can be identified during drying: bound and unbound water [7]. Bound water corresponds to the layers of water molecules adsorbed at the body surface. Unbound water is the moisture that moves through the solid pores during drying. This unbound water is present within the pores in two distinguishable states: liquid and/or vapour.

1.1.1 Defining the moisture content of a ceramic green body

Since the ceramic green bodies contain a liquid phase which is usually water in addition to the solid, it is necessary to determine the proportion of the liquid phase. In many situations, as for the work of this thesis, the moisture content can be defined as the water mass divided by the dry mass of the sample after complete drying at 110 $°C$. It is always accompanied by the designation DB which means dry basis. It can be expressed

with the following relation:

$$X = \frac{w(t) - w_d}{w_d} \tag{1.1}$$

X is the moisture content on dry basis,
$w(t)$ is the sample weight at time t during drying, and
w_d is the sample weight dried at 110 $°C$ until a constant weight is achieved.

There is another way to express the moisture content which is called wet basis (WB). It is defined as the water mass divided by the initial total weight of the solid and water (w_{init}):

$$X' = \frac{w(t) - w_d}{w_{init}} \tag{1.2}$$

where X' is the moisture content on wet basis.

1.1.2 Heat transfer

The evaporation of water requires heat input. For example, the enthalpy of vaporization at 0 $°C$ is 2500 $kJ\ kg^{-1}$. Three mechanisms can supply heat in order to evaporate water: convection, conduction and radiation or mostly, by a combination of two or three of these [8]. These are discussed in greater detail below:

- **Heat transfer by convection**: this involves a flow of hot air passing over the moist surface of the body. The hot air flow supplies energy to evaporate the water and also ensures the transportation of water vapour out of the drying zone. Two types of convection are distinguished, depending on the external conditions. First, forced convection with turbulent or streamlined flow of air driven by a fan. Then, natural convection where the movement of air is induced due to density differences in the gas phase caused by the temperature gradient present between the surrounding medium and the wet surface.

- **Heat transfer by conduction**: a part of heat required for water evaporation from the ceramic body can be provided through a temperature difference by direct contact with a hot surface.

- **Heat transfer by radiation**: heat transfer from an outside source takes place by radiation. It does not require direct contact with the moist body and concerns essentially the surface zones.

The present study focuses particularly on convective drying due to its frequent use in ceramic industry. Different mechanisms of convective drying involving evaporation are now examined.

1.2 Physical principles of drying

1.2.1 Evaporation of water

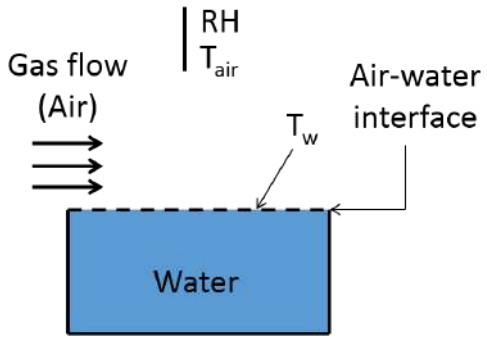

Figure 1.1: A schematic representation for the evaporation of water in given air conditions.

Consider first a body, constituted of uniquely water, exposed to air. The evaporation rate depends on the relative humidity (RH) and air temperature (T_{air}). The relative humidity can be defined by the following relation:

$$RH(\%) = 100 \times \frac{p_v}{p_s} \tag{1.3}$$

where p_v is the partial pressure of the water vapour present at a given temperature and p_s is the partial pressure of the water vapour present at saturation for the same temperature. This pressure at saturation can be related to temperature by:

$$p_s(T) = 133,322 \exp(46,784 - \frac{6435}{T} - 3,868 \ln(T)) \tag{1.4}$$

- If RH = 100%, the air is saturated in water vapour, i.e. the air is in equilibrium with the liquid phase. Thus no evaporation takes place.
- If RH < 100% liquid water transforms into vapour and diffuses into air.

A way to determine the relative humidity is to measure the ambient air and wet temperatures (T_{air} and T_w, respectively). From these temperatures, assuming an evaporation with a constant enthalpy of the humid air, the partial pressure of water vapour can be calculated and then the RH can be deduced from equation 1.3. The relative humidity can also be calculated directly from the difference between these temperatures using expressions found in the literature as for example [9]:

$$RH = 10^{-(23.5518+[\frac{-2937.4}{T_{air}}])}(T_{air})^{4.9283}[10^{(23.5518+[\frac{-2937.4}{T_{air}}])}(T_w)^{-4.9283} - (6.6 \times 10^{-4} + 7.57 \times 10^{-7} T_w)p(T_{air} - T_w)] \tag{1.5}$$

The wet temperature or also called wet bulb temperature is the equilibrium temperature of the wet surface when the water evaporates by convection. The wet temperature is lower than that of air, but if RH = 100% both temperatures are equal.

1.2.2 Heat and mass transfers

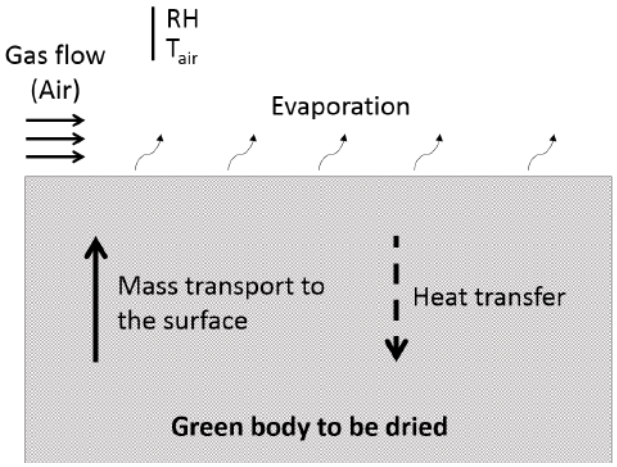

Figure 1.2: A schematic representation of the liquid transport out of the porous body through heat and mass transfers.

Consider now a porous solid with pores entirely filled with water. Drying of the porous solid involves a coupling of two types of transfer: heat transfer from the surroundings towards the moist sample and mass transfer from the sample towards its surface and then to the surrounding air (figure 1.2). These two transfers can be described using the fundamental laws describing heat and mass transport:

- Heat transfer obeys Fourier's law which corresponds to the conduction of heat in the system. Its equation, which must be respected throughout the body, can be written as [10]:

$$q = -\lambda \nabla T \tag{1.6}$$

  where q is the heat flux in $W\ m^{-2}$,
  T is the temperature in K, and
  λ is the thermal conductivity in $W\ m^{-1}\ K^{-1}$,

- Mass transfer obeys Darcy's law and Fick's law. The first law corresponds to liquid flow through a porous medium and the second concerns the diffusion of water

vapour. In fact, the transport of moisture through the body during drying can occur by two mechanisms: liquid flow by capillarity and gas diffusion as water vapour. The relative proportion of these mechanisms depends on the physical structure of particles, pore shapes, pore size distribution and especially on the actual liquid content of the system during drying.

At the beginning of drying, the system is assumed to be constituted uniquely of solid particles separated by continuous water in liquid form. In this case the dominant mechanism is liquid flow through the pores which can be described by a gradient in pressure according to Darcy's law as following [11]:

$$J_L = -\frac{D}{\eta_L}\nabla P_L \tag{1.7}$$

where J_L is the flux of the liquid in units of volume per unit area of the porous sample per unit time in $m\ s^{-1}$,
D is the permeability in m^2,
η_L is the viscosity of the liquid in $Pa\ s$, and
P_L is the force per unit area of the liquid in Pa.

Then as drying progresses, and particularly for the case of a green body when the particles stop approaching each other, liquid migrating out of the system is replaced by air. The gas diffusion mechanism now comes into play to transport moisture as vapour through the pores to the sample surface where it can be removed. This diffusion can then be related to the concentration gradient according to Fick's law [10]:

$$J_D = -D_w \nabla C \tag{1.8}$$

where J_D is the diffusion flux in $mol\ m^{-2}\ s^{-1}$,
D_w is the diffusion coefficient in $m^2\ s^{-1}$, and
C is the concentration of water in $mol\ m^{-3}$.

1.2.3 Exchanges with surrounding air

For convective drying, the porous body surface is directly in contact with air. The relationship between the wet surface and the surrounding air must then be taken into account. Generally, in this situation, a thin film called the boundary layer is always formed close to the surface, and it can be described as a zone exibiting concentration gradients of water. The thickness of the boundary layer is defined as the value of the height (H) for which $\frac{C_{s-b.l}-C_{b.l}}{C_{s-b.l}-C_{air}} = 0.99$, where $C_{s-b.l}$ is the water vapour concentration in the boundary layer just above the body surface in $mol\ m^{-3}$, C_{air} is the water vapour concentration

in the air, and $C_{b.l}$ is the water vapour concentration in the boundary layer [12]. This boundary layer controls the transfer of moisture from the body into water vapour in the surrounding atmosphere and also conducts heat from the surrounding atmosphere to the body surface (figure 1.3) [13].

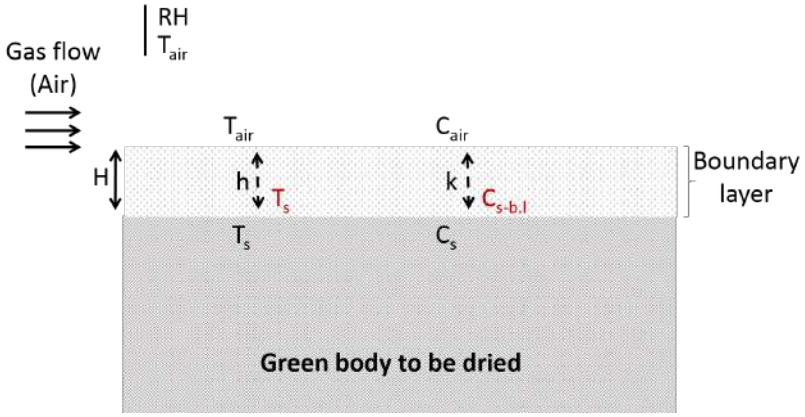

Figure 1.3: A schematic representation of heat and mass fluxes at a moist surface drying by convection.

The mass transfer (ϕ_C) can then be defined as proportional to the concentration difference across the boundary layer:

$$\phi_C = -k(C_{air} - C_{s-b.l}) \tag{1.9}$$

where k is the convection mass transfer coefficient in $m\ s^{-1}$.

Both concentrations can be related to the vapour pressures of water through the ideal-gas law:

$$\begin{cases} C_{air} = RH\ \frac{P_s(T_{air})}{R\ T_{air}} \\ C_{s-b.l} = a_w\ \frac{P_s(T_s)}{R\ T_s} \end{cases} \tag{1.10}$$

where RH is the relative humidity,
a_w is the water activity, which will be defined in the next paragraph,
R is the ideal gas constant in $J\ mol^{-1}\ K^{-1}$, and
P_s is the saturated vapour pressure of water in Pa.

Focusing now on the heat transfer, the heat exchanged by convection with the air through the boundary layer (ϕ_{T_1}) can be described as:

$$\phi_{T_1} = -h\ (T_{air} - T_s) \tag{1.11}$$

where T_{air} is the air temperature in K,
T_s is the body surface temperature in K, and
h is the heat transfer coefficient in $W\ m^{-2}\ K^{-1}$. This heat transfer coefficient depends on the air flow velocity near to the boundary layer. For example with free convection in air $2 < h < 25$ and with forced convection $25 < h < 250$,

Furthermore, since the evaporation occurs at the body surface, a second term of heat transfer (ϕ_{T_2}) which takes into account the heat of vaporization comes into play. This term relates the enthalpy of vaporization to the mass transfer as following:

$$\phi_{T_2} = L_w\ M_w\ \phi_C \tag{1.12}$$

where M_w is the water molar mass in $kg\ mol^{-1}$, and
L_w is the latent heat of vaporization in $J\ kg^{-1}$.

Since the mass and heat transfers both occur within the boundary layer and they are governed by dimensionless equations of the same form, a relation between their coefficients exists by analogy given by:

$$k = \frac{h}{\rho_{air}\ Cp_{air}\ Le_f} \tag{1.13}$$

where ρ_{air} is the air density in $kg\ m^{-3}$,
Cp_{air} is the air heat capacity in $J\ kg^{-1}\ K^{-1}$, and
Le_f is the Lewis number. Its value for air-water vapour mixture is usually assumed to be equal to 1 to simplify the governing equations of heat and mass transfers [14].

1.2.4 Physical properties involved in drying

The physical properties involved in drying such as, the activity of water, heat capacity, thermal conductivity and the diffusion coefficient depend strongly on the moisture content within the body. Several studies have focused on modeling of mass and heat transport, going from very simple models to more complex ones. However, for every model used to describe drying, there is always the need to employ accurate values of the physical properties. Available information in the literature for each property will be discussed in the following paragraphs, since in chapter 4 we will report new results obtained for ceramic green bodies of alumina and kaolin clay.

1.2.4.1 Water activity

Water activity (a_w) in a body is a measurable property that depends on temperature and moisture content. It represents the ratio between water vapour pressure at the body

surface (P_v) and the saturation pressure above a free water surface (P_s) at the same temperature T [13]:

$$a_w = \frac{P_v}{P_s} \tag{1.14}$$

- If the moist surface behaves as a free water surface $P_v = P_s$, then $a_w = 1$.
- If only bound water remains within the body (i.e. is held on the internal surfaces), $P_v < P_s$ and then $a_w < 1$.

1.2.4.2 Diffusion coefficient

Several studies have been dedicated to obtain values for the diffusion coefficient during drying. Certain methods are based on numerical modeling where the diffusion coefficient is fitted to yield the correct distribution of water in the porous solid [15]. For instance, for water evaporation from a porous alumina pellet the diffusion coefficient of water within the pellet was deduced to be 5.10^{-8} m^2 s^{-1} from the concentration profile evaluated by Magnetic Resonance Imaging (MRI) measurements. More direct experimental techniques based on weight measurements to estimate the diffusion coefficients for brick materials, have shown significant dependence on moisture content during drying (figure 1.4) [16]. Van der Zanden and Wit have used for their modeling study an empirical relation for the diffusion coefficient which varies between 10^{-5} m^2 s^{-1} and 10^{-8} m^2 s^{-1} depending on the water content.

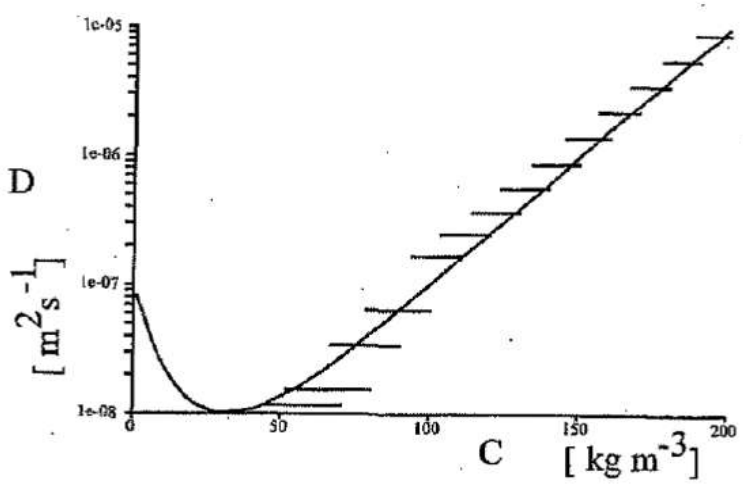

Figure 1.4: Measured diffusion coefficient (short lines indicating error bars) compared with the diffusion coefficient described by an emperical relation (curved line) as a function of the water concentration given in reference [16].

1.2.4.3 Heat capacity

The heat capacity also depends on the moisture content within the product. It is defined as the amount of energy required to raise the temperature of a system by one kelvin. Since the water content can be determined during drying, the heat capacity of a wet porous body can be calculated simply as a function of moisture content using the rule of mixtures:

$$Cp = \frac{X\ Cp_{water} + Cp_{solid}}{X + 1} \tag{1.15}$$

where X is the moisture content on DB.
Cp_{water} is the heat capacity of water in $J\ kg^{-1}\ K^{-1}$, and
Cp_{solid} is the heat capacity of the solid in $J\ kg^{-1}\ K^{-1}$.

The heat capacity of water is equal to 4210 $J\ kg^{-1}\ K^{-1}$ at 20 $°C$, more than 4 times the value for many ceramic oxides. For example alumina has a value of 780 $J\ kg^{-1}\ K^{-1}$. Consequently the incorporation of water into a porous solid has a strong effect on the overall heat capacity.

1.2.4.4 Thermal conductivity

The role of water on the thermal conductivity has been widely investigated, for example for soils, or more recently, for containers of radioactive waste and in materials for buildings [17, 18]. All these studies show that the thermal conductivity increases with increasing water content. In the case of compacted bentonite, the thermal conductivity increases from 0.5 to 1 $W\ m^{-1}\ K^{-1}$ when the volume fraction of water in the pores is increased from 30 to 90% [19]. For zirconia samples, the thermal conductivity increases from 0.2 to 0.8 $W\ m^{-1}\ K^{-1}$ when the volume fraction of water in the pores is raised from 4 to 80%. Changes in the thermal conductivity can be explained using an approach based on a mixture of phases by replacing a volume of air with a thermal conductivity of 0.026 of $W\ m^{-1}\ K^{-1}$ by a volume of water with a higher thermal conductivity: 0.61 $W\ m^{-1}\ K^{-1}$. Several models have been proposed and tested in literature to describe the behaviour of the thermal conductivity with water content [17, 20, 21]. More recently, in the case of granular materials, it has been shown that variations in the thermal conductivity with water content cannot be explained solely by the contribution of water as an additional phase in the material [18]. The authors have reported an increase in the thermal conductivity of packed silica sand from 0.4 $W\ m^{-1}\ K^{-1}$ for the dry state to 1.8 $W\ m^{-1}\ K^{-1}$ with just 2 vol% of water. They explain this increase by reduction of the thermal resistance at contact interfaces between solid grains. In all of these studies the overall volume of the material which consists of solid, water and air did not vary when the water content was changed or this is not mentioned by the authors. In the case of

drying a green body, the volume of the sample may vary when the water is removed. In the present study we will report new results obtained for thermal conductivity variation during drying including dimensional changes.

1.3 Drying mechanisms

1.3.1 Drying stages

Given that the principal aim of drying is the extraction of water from a body, one of the first means used hitherto for the description of the drying process is to examine the weight loss over time as shown in figure 1.5.

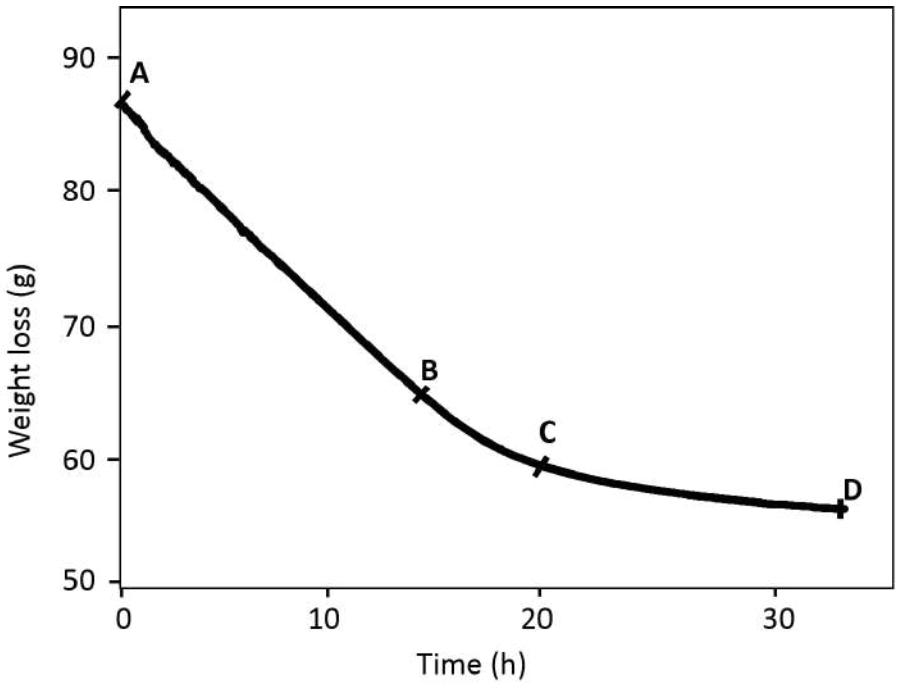

Figure 1.5: A plot of weight loss of a green body against the drying time.

Drying of a ceramic green body under constant conditions (temperature, relative humidity and air velocity) is a process which goes through different stages. These are clearly distinguished in figure 1.6 which represents the drying rate derived from the weight curve as a function of moisture content [8]. First, the moisture content decreases linearly at the beginning of drying. This period is called the constant rate period (CRP), because the slope of the weight curve is essentially constant (A to B in figure 1.5). Then at some definite moisture content, the drying rate decreases, entering a regime called, the falling rate period (FRP). Furthermore, in most cases, depending on the material type and the conditions of drying, the falling rate period can be divided into two periods. The first falling rate period exhibits a proportionality between the rate of drying and the moisture

content (B to C in figure 1.6). Then the second falling rate period corresponds to extraction of the last vestiges of moisture content in the body. In this situation the drying rate is no longer a linear function of moisture content (C to D in figure 1.6).

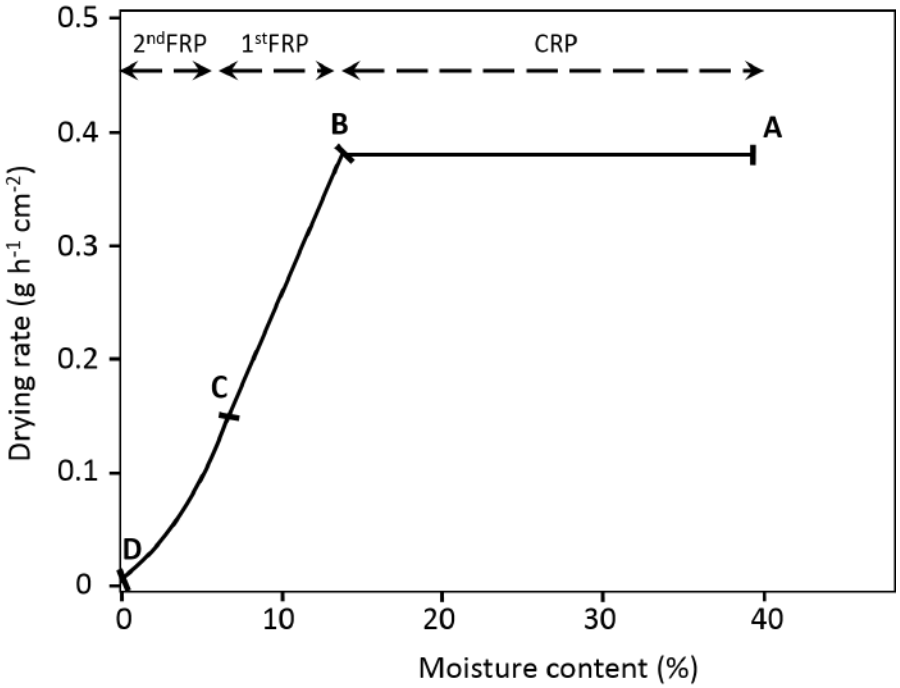

Figure 1.6: Drying rate as a function of moisture content for the different stages of drying.

Schematic representations of the water distribution in a porous body during drying are shown in figure 1.7. These are related to the changes in drying rate discussed in greater details in the next paragraphs.

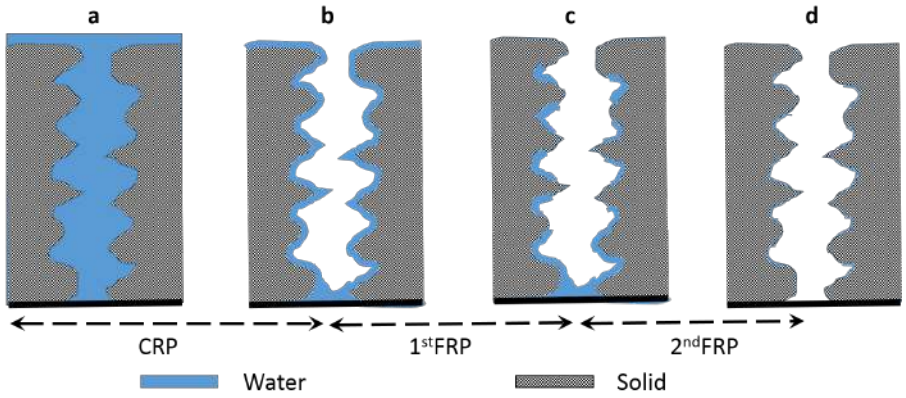

Figure 1.7: Schematic representations of drying stages within a porous body (adapted from [11]).

- **The constant rate period (CRP)**

  During this first period the surface is covered by a continuous film of water and the evaporation of water occurs at the body surface (figure 1.7 a). Consequently, the drying rate is assumed to be independent of both the water content and the type of the material. In the case of drying with only convection to bring heat for removing water from the surface, the surface temperature of the body should strictly be the wet bulb temperature of the surrounding air which is lower than the temperature of the atmosphere. This difference in temperatures is related to the rate of evaporation. Furthermore, when water is evaporated from the surface, capillary forces ensure the flow of water from the interior of the body to the surface. Therefore, the liquid films surrounding particles decrease in thickness and particles approach to each other. In this situation, the volume of water evaporated is directly accompanied by a significant decrease of the apparent volume of the body. Figure 1.8 illustrates a simplified green body-water system during the first stage of drying.

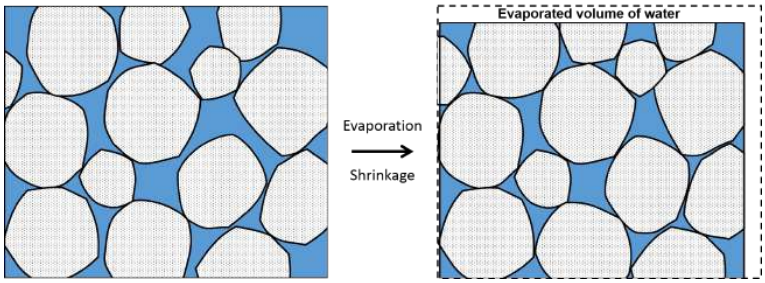

Figure 1.8: Schematic representation of particles-water system during shrinkage.

- **The first falling rate period (1^{st}FP)**

  This period is characterized by a proportionality between the evaporation rate and the drying time (B to C in figure 1.6). Shrinkage has stopped but a part of the evaporation still occurs at the surface even if this is no longer behaving as a free water surface. From now on until the end of drying, the temperature at the body surface rises. Evaporated water is replaced by air, as shown in figure 1.7 b. Consequently, water evaporates, in addition to the surface evaporation, within unsaturated pores and the vapour is transported by gaseous diffusion. Furthermore, in some cases, an evaporation front can develop during this period, i.e. there is a liquid/vapour interface with a strong gradient of moisture content which separates wet zones from the drier zones.

- **The second falling rate period (2^{st}FP)**

During this final stage, the relationship between drying rate and moisture content is no longer linear (figure 1.6). The liquid phase becomes discontinuous (figure 1.7 c). Thus the residual water is evaporated at greater depth in the porous body so that it is transported to the surface only by vapour diffusion.

This summary of drying stages, which has been broadly discussed in the literature [7, 8,11,22–24], gives a a good general picture for understanding the drying process. However because of the importance to mechanical strength and control of body dimensions, the next section examines green body shrinkage in more detail. Particular attention to this aspect is also made in the experimental part of the thesis.

1.3.2 Shrinkage

1.3.2.1 Driving forces for shrinkage

The liquid migration through the pores during the CRP causes a reorganization of particles and changes in dimensions of the pores through which the liquid flows. Scherrer has examined the interaction between migration of water and dilatation of bodies in terms of the driving forces for shrinkage, especially in the case of gels. But the principles also apply to other ceramic green bodies. These forces include capillary pressure, osmotic pressure and disjoining pressure which are briefly described below [11]:

- **Capillary pressure:** given that water evaporates from the surface, the liquid film surrounding particles decreases. Thus, the liquid/vapour interface tends to form curved menisci within the pores. The capillary pressure (P) ensures the migration of water from the interior to the surface. From a theoretical point of view, it can be defined as the difference between the pressures of water and air.

$$P = \frac{2\gamma}{R_c} \tag{1.16}$$

  where γ is the liquid/vapour interfacial energy, and
  R_c is the radius of curvature of the meniscus which can be related to the radius of the pore (r) and the contact angle (θ) by $R_c = \frac{r}{cos(\theta)}$.

- **Osmotic pressure:** consider as an example pure water diffusing through a semipermeable membrane to dilute a salt-rich solution. Osmotic pressure corresponds to migration of a solvent from the zones with lower salt concentration to the zones with higher salt concentration through a semipermeable membrane without any change of phase. In the case of the present thesis, osmosis is not taken into account since all mixtures which have been studied are constituted only of water and solid.

- **Disjoining pressure:** the disjoining pressure characterizes the state of a liquid or gas film trapped between two surfaces of the solid. In other words, owing to a particular organization of water molecules close to the solid surface, the stability and the wettability of liquid film is governed by the disjoining pressure.

- **Moisture stress:** called also the moisture potential, corresponds to the free energy of water in a porous body. It includes all the driving forces mentioned above and can be obtained by measuring the vapour pressure.

1.3.3 Linear shrinkage and Bigot curve

For at least 100 years, in the literature [25–28], drying shrinkage has mostly been expressed as change in length over time. A popular and useful method of investigating the behaviour of a ceramic paste consists of monitoring simultaneously the length and mass during drying with slow kinetics to ensure a uniform shrinkage. Thus, the time dependence can be removed by plotting the water content on a dry basis as a function of the linear shrinkage to obtain the well-known Bigot curve. This is presented in figure 1.9 [29]. Such an approach to representing the drying behaviour of ceramic green bodies with linear shrinkage and the water content in the same graph was also proposed by Kingery [30]. These curves are used to illustrate drying behaviour, which can vary depending on raw materials, mixtures, additives or drying conditions.

The linear shrinkage (Sh) is calculated with the following relation:

$$Sh = \frac{L(t) - L_d}{L_d} \tag{1.17}$$

where L(t) is the length of the sample at time t, and
L_d is the length of the sample at the end of drying.

To summarize the important information which can be extracted from the curve, three distinct zones can be distinguished [31]. These are now listed with mention of any particular limitations to the interpretation:

- (1) At the beginning (zone between points A and B), shrinkage is directly related to the moisture content. The decrease in dimensions simply corresponds to the volume of liquid evaporated. Furthermore, the linear zone is known to be large for clay materials and less extended for non clay materials (e.g. sandy material).

- (2) Between points B and C, shrinkage is no longer linear. During this period particles begin gradually to be in contact with each other which decreases the overall amount of shrinkage [32]. The moisture content M_{BC} (between B and C in figure 1.9) is called the critical moisture content because it separates the period with

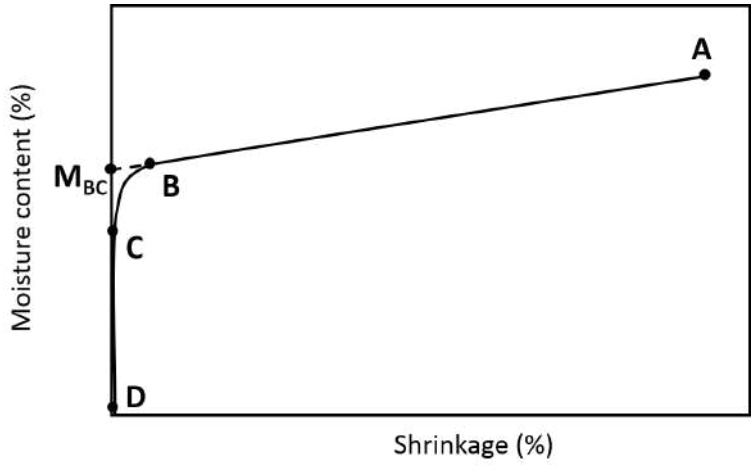

Figure 1.9: Schematic representation of a typical Bigot's curve.

major shrinkage from that with negligible shrinkage. The green bodies are called leatherhard at this point. In practice, before that point is attained drying has to be performed carefully to avoid defects. Then when this point is reached the ceramic green body can be handled without fear of distortion [7].

- (3) In the last stage (zone between points C and D), where shrinkage is negligible, the particles are all in contact with each other and, the water located in the pores is progressively replaced by air.

1.3.4 Air penetration and distribution of water

In the first stage of drying the evaporation of water takes place essentially at the body surface and water migrates from the interior to replace it. Then, when the shrinkage becomes negligible, air penetrates the system. A recent study of the drying process for a suspension with particle size of approximately 1.1 μm was made in order to observe the invasion of air within a porous media [33]. It was shown through micrographs obtained with confocal microscopy that the transition between regimes causes an abrupt invasion of air into the body (figure 1.10).

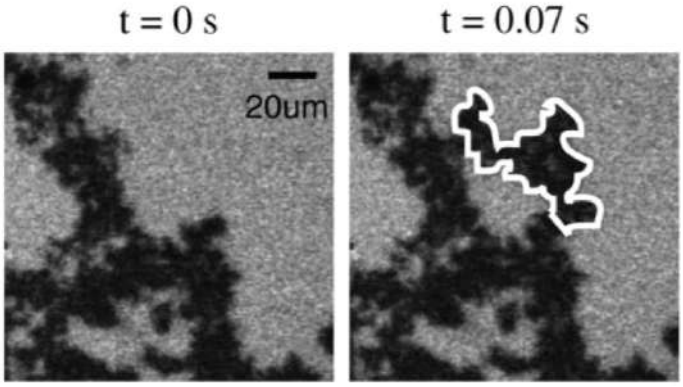

Figure 1.10: Image of one large burst. An area of size corresponding to 800 particles (the highlighted area) is invaded within 0.07 s [33].

Given that the large pores present greater volume for less surface area interacting with and holding the liquid phase, it is likely for porous media that air first penetrates the large pores before the small ones. However, as evaporation takes place firstly at the surface, the water in small pores tends to evaporate but the menisci formed in these small pores yields reduced pressure and draws liquid from menisci in large pores placed at a greater depth within the body. In figure 1.11, we observe this phenomenon in a system with different pore sizes. The small pore at the top of the image (indicated by the upper arrow in the second image) fills with water while the bottom pore is emptied (indicated by the lower arrow in the same image).

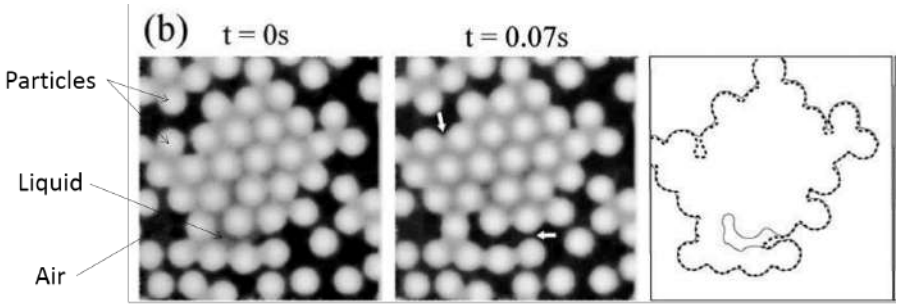

Figure 1.11: liquid redistribution due to penetration by a burst of air. The 1st image is before the burst and the 2^{nd} is after. An invasion occurs at the lower arrow spot, resulting in an obvious meniscus readjustment at the upper arrow spot. The 3^{rd} picture traces the air/liquid interface of the first two images. The dotted curve is before the burst and the solid one is afterwards. It shows menisci readjustments at several positions [33].

The question about where the liquid is located during drying was also investigated in a simpler case (without considering the shrinkage of the material) using Nuclear Magnetic Resonance (NMR) imaging [34]. The water distribution along the diameter of an alumina pellet with a bimodal distribution of pore sizes is presented in figure 1.12. The alumina

pellets contains agglomerate of clusters with mesopores inside and macropores between clusters as shown in figure 1.13. According to figure 1.12 c, the air penetrates first the macropores close to the external surface at first (figure 1.13, 1^{st} schematic). This yields a rounded profile at the sample edges (profiles 1 and 2 in figure 1.12 b). Due to capillary flow of liquid a redistribution of water takes place and the mesopores stay filled until all macropores become empty (figure 1.13, 2^{nd} schematic). This implies a rectangular concentration profile shape (profile 3 in figure 1.12 b). Then mesopores close to the surface of the sample are drained before those at greater depth as shown in the $3^r d$ schematic of figure 1.13. This results again in pronounced round profiles (profiles 6 to 10 in figure 1.12).

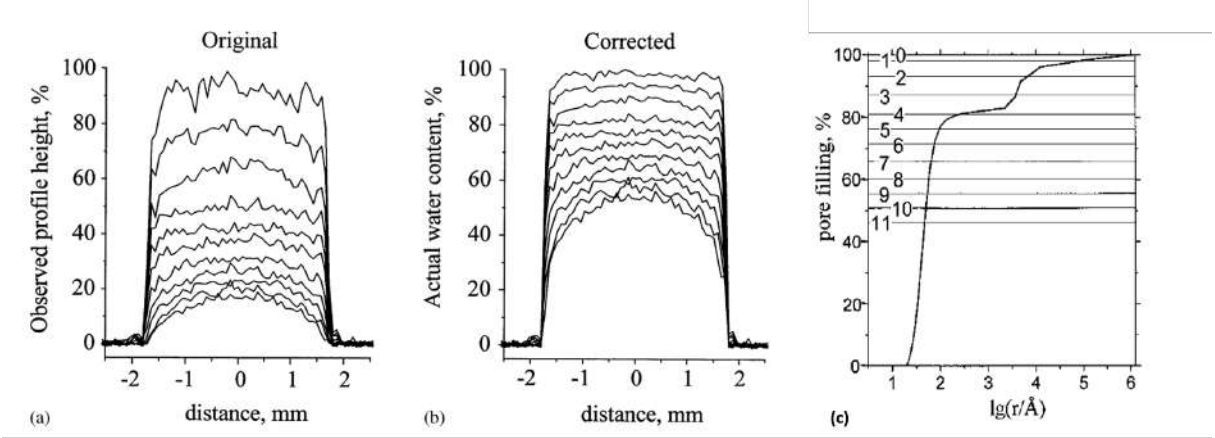

Figure 1.12: The profiles for water distribution along the diameter of an alumina pellet in the course of its drying. (a) Original profiles and (b) those corrected for the relaxation effects. (c) Cumulative pore size distribution of the alumina II sample. Horizontal lines show the average height of the corresponding profiles. [34].

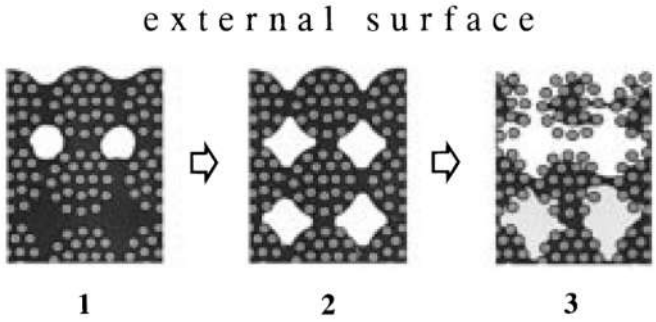

Figure 1.13: Schematic representation of liquid distribution at the various stages of drying in a sample representing an agglomerate of clusters of primary particles [34].

1.4 Management of drying behaviour

Thus far we have only described the mechanisms which occur during drying, in general terms. These mechanisms have a strong dependence on different parameters such as material composition, shape, size and the external conditions. The dependence of each parameter on the drying behaviour will be discussed in the following paragraphs.

1.4.1 Material formulation

For the ceramic industry, successful drying must respect two main criteria: minimized energy consumption and final product appearance (absence of defects or deformation). Indeed, one method used to improve the quality of dried products while optimizing energy consumption consists of choosing the composition of the material in order to influence the drying behaviour in a certain specific way. This can be illustrated by two examples of additives incorporated in ceramic materials. Each type of modification to the composition influences the overall shrinkage and the drying rate.

First, one of the cures in traditional ceramics for reducing drying shrinkage and making the green body more resistance to defects is by adding grog, shale or other nonplastics [7]. For example, in the brick industry, the typical starting formulation is a mixture of clay powder with quartz particles (nonplastic material) [35, 36]. The quartz particles hardly interact with water and exhibit a large grain size ($> 100\ \mu m$). However, clay powders with smaller particles exhibit plasticity and also a significant shrinkage on drying that increases the probability of inducing defects. Based on this difference in behaviour the overall shrinkage of a clay/sand mixture is less and consequently helps to improve the quality of products after drying. Furthermore, the amount of water added to the mixture depends on factors, such as the proportion and the particle size of constituent powders. In practice, up to 30% of quartz is added on a dry basis which typically decreases the amount of water required for shaping [35].

Another possible way to change the drying behaviour is to modify the water activity. Fuks et al. studied alumina foams which crack under certain conditions of drying [37]. They tested several cosolvents with low volatility in order to alter the drying behaviour. Results show that reducing the volatility of the liquid phase yields a decrease in the total amount of evaporated liquid as shown in figure 1.14. Consequently the transport mechanisms are affected since the migration of liquid is dominated by gaseous diffusion and not by capillary pressure.

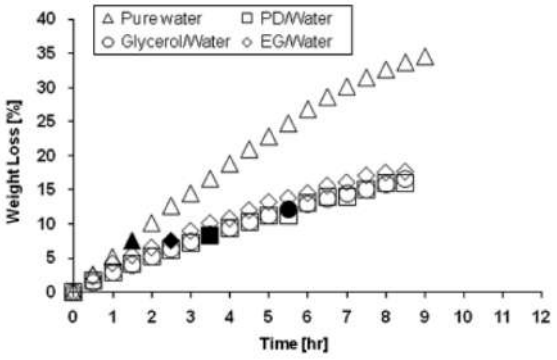

Figure 1.14: Total weight loss versus time. Filled symbols represent the onset of the first crack formation in case of pure water and propanediol(PD)/water and ethylene glycol (EG)/water systems or separation from walls in case of glycerol/water system. The alcohol/water ratios were 1:5 in all cases [37].

1.4.2 Product shape and size

In the ceramic industry, the shape and size of the ceramic bodies vary significantly, depending on the type of products. Generally, the generation of defects increases with sample shape and size. Consequently, the production of large and complex parts is difficult. Starting with the effect of shape, the evaporation rate of water from different positions in a body with complex shape is not necessarily uniform. In other words, as certain zones of the surface are not exposed to free air, the surrounding relative humidity of air next to these surface zones differs. Consequently, the corresponding shrinkage is not uniform. Simply, from a point of view of body dimension, drying is slower for larger parts. During the constant rate period, where evaporation takes place on the surface, the drying rate is independent of the thickness. Since the body is larger, containing more water, drying will take longer. Then during the falling rate periods, gaseous diffusion within the sample becomes a limiting factor and the drying rate becomes linked to the thickness of the product increasing the drying time.

1.4.3 External conditions

The manner in which the drying behaviour undergoes changes due to surrounding external conditions expressed by parameters such as temperature, humidity and the flow of air, is clearly important. The following table summarizes the effect of each parameter on shrinkage and the drying rate.

Parameters	Shrinkage	Drying rate
↗ Temperature	Formation of a crust at zones close to surface which prevents a uniform shrinkage. Accordingly, the overall shrinkage appears to be reduced.	The drying rate increases and the time required for complete drying becomes shorter.
↗ Relative humidity	Uniform shrinkage occurs with high relative humidity	The difference in vapour pressure between the moist surface and air decreases with increase of the relative humidity of the ambient air. As a consequence of this the drying rate decreases.
↗ Flow of air	Shrinkage is more rapid at positions close to the surface than the interior of the sample which may modify the overall shrinkage	When air flows across the surface of the moist sample, it helps to sweep away the evaporated water and replaces it by dry air. The rate of evaporation is then accelerated. For example, according to Ford the rate of evaporation is proportional to $V^{0.8}$ where V is the air velocity. Furthermore, with a flow perpendicular to the drying surface, the degree of turbulence at the surface is greater than with a flow parallel to the drying surface. This gives higher coefficients of mass transfer and heat transfer and consequently increases the drying rate [8].

Table 1.1: Description of the effect of external parameters (temperature, relative humidity and flow of air) on shrinkage and drying rate.

1.5 Conclusion

Drying is the operation of removing water from the porous material by evaporation. This moisture can be present within a porous ceramic body in liquid and/or vapour

states. Then to evaporate it, heat is required which can be supplied by convection, conduction and radiation or by a combination of two or three of them. The present thesis focuses particularly on convective drying.

From a theoretical point of view, drying can be described as a coupling of heat and mass transfers. Such description dealing with heat and mass transfer equations involves different properties: water activity, diffusion coefficient, heat capacity and thermal conductivity. All these properties vary significantly with the moisture content remaining within the porous solid during drying. Thus in the present work, we focus particularly on the role of water for each specific property.

By looking at the particular case of drying ceramic green bodies, the process can be divided into two or three stages, depending on the material nature and conditions of drying. The first stage which is called the constant rate period corresponds to the removal of liquid from the body surface by evaporation. Capillary forces ensure the flow of water from inside to the surface. In most cases, this period is accompanied by shrinkage which has been the topic of many investigations in the literature due to its close relation to drying difficulties such as cracking. The second and third periods called the falling rate periods, start after the end of shrinkage. A second transport mechanism is involved during these periods which is vapour diffusion within the porous body. Finally, it has been shown that these mechanisms are variable and sensitive to different parameters such as the wet body formulation, shape , size and the external conditions.

This first chapter has briefly described the state of the art concerning drying of ceramic green bodies and the different relationships between the ceramic green body to be dried and the surrounding atmosphere. On the basis of this knowledge, practical interpretation of two technologically important materials is discussed in the next chapter in order to identify their macroscopic drying behaviour.

Chapter 2 :

Macroscopic drying behaviour of green bodies

Chapter context

The second chapter discusses variations in the drying behaviour for different ceramic pastes. Three materials were selected for this study: alumina, kaolin and montmorillonite. First a brief description of materials and samples preparation is presented. Then characterization of drying behaviour has been made by the simultaneous measurements of sample dimension, mass and surface temperature of the green body to identify the stages of drying. Thus the effect of external conditions, i.e temperature and relative humidity, on the evaporation rate is examined. By concentrating on shrinkage during drying, the final part of the chapter presents a new approach with an optical camera to simultaneously determine bigot curves in two orthogonal directions, in order to investigate materials exhibiting anisotropic shrinkage. Such information is relevant to identifying difficulties in the ceramic processing.

2.1 Raw materials

2.1.1 Alumina

An α-alumina powder, denoted P172SB and supplied by the company Alcan, was used in this study.

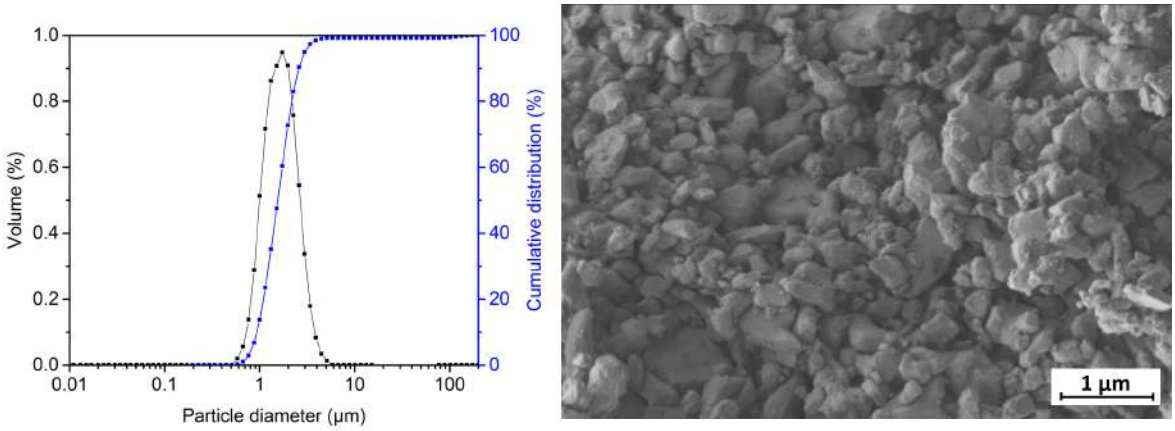

Figure 2.1: Particle size distribution measured by laser light scattering of alumina powder (P172SB) in an aqueous medium and SEM micrograph of the same powder.

This chosen alumina powder is suitable for the shaping process of casting due to its small grain size, represented by a median size of 0.4 μm. However, the median grain size measured using laser light scattering is 1.5 μm which is higher than the indicated value (figure 2.1). This difference can be explained by an agglomeration of grains which was confirmed after observation of alumina powder using the scanning electron microscope (SEM) (figure 2.1). It is clear that the grain size is smaller than the value

obtained using laser light scattering. Furthermore, the SEM micrograph reveals that grains are not perfectly spherical. The surface area of this alumina powder, measured using the Brunauer–Emmett–Teller (BET) method, is 7.5 $m^2\ g^{-1}$. The true density of 3.96 $g\ cm^{-3}$ was measured with a helium pycnometer and is close to the theoretical density of 3.98 $g\ cm^{-3}$ which is deduced from measurements of lattice parameters by X-ray diffraction [38] .

2.1.2 Kaolin

A kaolin clay powder, called BIP kaolin, was supplied by Imerys Ceramic France after extraction from the Beauvoir site.

- **Chemical and mineralogical compositions:** the chemical composition in weight percentage of BIP kaolin, deduced from measurement by the inductively coupled plasma (ICP) method, is given in table 2.1 which reveals that the major oxides constituting this clay powder are silica and alumina with a SiO_2/Al_2O_3 ratio of 1.3. This value suggests the presence of silica in another form for example quartz, since the ratio for kaolinite is 1.18. Indeed, using X-ray diffraction (XRD), three main phases were identified: kaolinite, muscovite and quartz with the mass percentages given in table 2.2.

Chemical composition	SiO_2	Al_2O_3	Fe_2O_3	CaO	MgO	Na_2O	K_2O	TiO_2	Li_2O
Mass %	48.1	36.9	0.26	<0.20	0.17	<0.20	1.90	<0.05	0.27

Table 2.1: Chemical composition in weight percentage of BIP kaolin.

Mineralogical composition	Kaolinite	Muscovite	Quartz
Mass %	78	17	4

Table 2.2: Mineralogical composition in weight percentage of BIP kaolin.

The distribution of particle sizes in BIP kaolin was measured using laser light scattering (figure 2.2) and the median grain size is 5.1 μm. Its specific surface area measured by BET method is 10 $m^2\ g^{-1}$ and the true density is 2.6 $g\ cm^{-3}$.

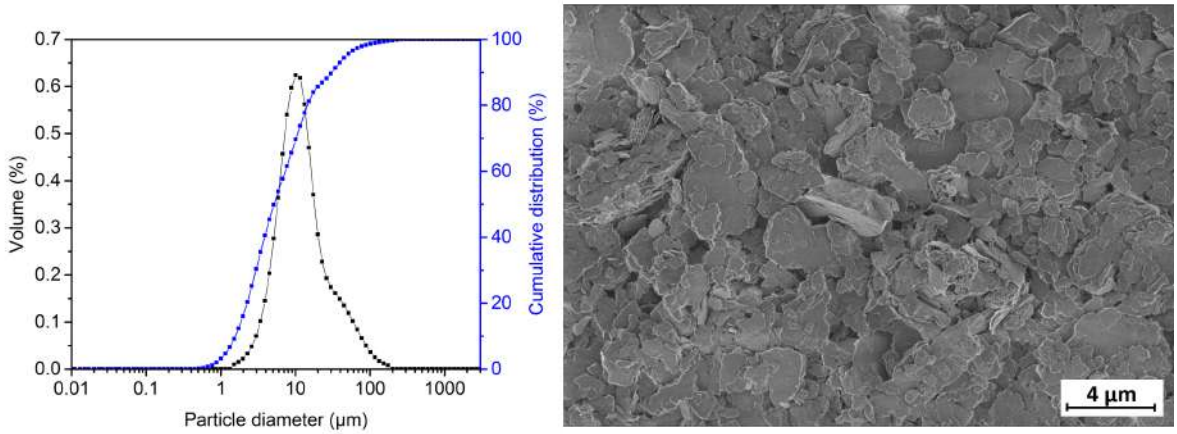

Figure 2.2: Particle size distribution measured by laser light scattering of BIP kaolin powder in an aqueous medium and SEM micrograph of the same powder.

2.1.3 Montmorillonite

The third raw material used in this study is a montmorillonite clay powder, denoted ABM.

- **Chemical and mineralogical compositions:** its chemical composition given by the supplier and the mineralogical composition are summarized in tables 2.3 and 2.4.

Chemical composition	SiO_2	Al_2O_3	TiO_2	Fe_2O_3	CaO	MgO	K_2O	Na_2O	P_2O_5
Mass %	56.6	17.9	0.36	4.2	2.6	5.9	1.2	<0.2	0.08

Table 2.3: Chemical composition in weight percentage of montmorillonite.

Mineralogical composition	Montmorillonite	Quartz	Other phyllitic clay minerals
Mass %	95	< 1	< 5

Table 2.4: Mineralogical composition in weight percentage of montmorillonite.

The median grain size of this powder is 7.4 μm. As can be seen in figure 2.3 a bimodal distribution of particles is revealed. The D10 is 2.2 μm and the D90 is 49.9 μm. However, the specific surface area of this powder measured with BET is 88 $m^2\ g^{-1}$ which is high with respect to the average grain size. This suggests that the grains are constituted of smaller clay particles which have agglomerated. The density of this powder is 2.3 $g\ cm^{-3}$. The physical structure of montmorillonite is in the form of sheets and layers with the particularity that water can insert itself between layers to cause swelling of the particles [39, 40].

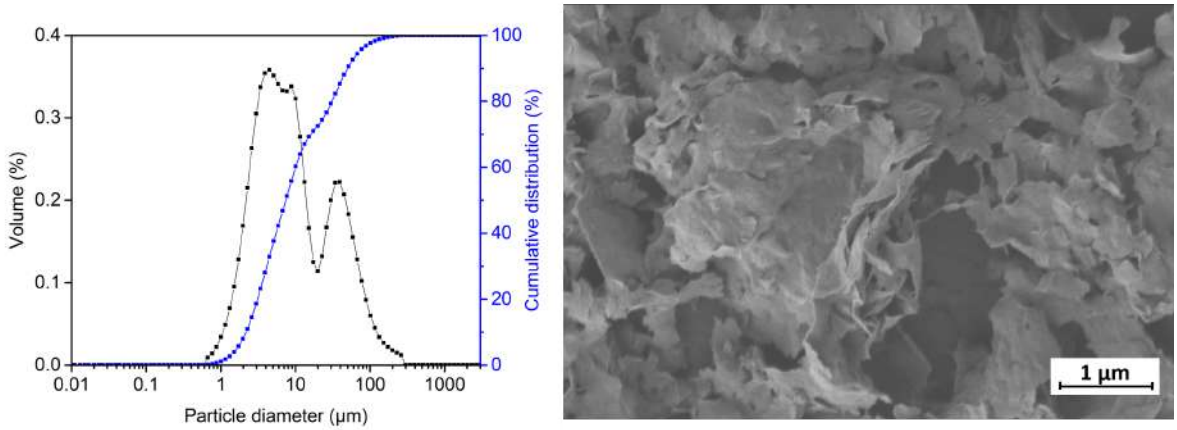

Figure 2.3: Particle size distribution measured by laser light scattering of montmorillonite clay powder in an aqueous medium and SEM micrograph of montmorillonite clay powder.

2.2 Pastes preparation

Initially, each powder was mixed with water according to the mass quantities in Table 2.5. The mixture was stirred in a jar mill (FAURE Equipement) for 75 minutes with a rotation speed of 35 rpm (figure 2.4 step 1), in order to obtain a homogeneous slurry without any clumps. With the aim of manipulating the mixture and obtaining a homogeneous ceramic paste, the mixture was cast manually on a porous plasterboard and maintained there for approximately 20 minutes to absorb a part of the initial water, (figure 2.4 steps 2 and 3). The paste was cut into samples with the desired dimensions (figure 2.4 step 4). This step proved to be difficult for smaller dimensions; in which case a removable mold was then used to shape samples. Finally, to avoid any premature evaporation before the drying study, the samples were covered with a hermetic plastic film and placed in an atmosphere saturated in water vapour (figure 2.4 step 5). As the plaster absorbed a part of the slurry water, the obtained samples have a liquid weight percentage which is less than that of the initial composition. The shaped samples final composition before drying is given in Table 2.5. It can be noted that the montmorillonite retains a larger amount of water compared to kaolin and alumina.

	Water content on DB (mass %w) in the initial suspension	Water content on DB (mass %w) in the wet pastes
Alumina	100	~ 30
Kaolin	186	~ 40
Montmorillonite	186	~ 100

Table 2.5: Water content in weight percentage in the initial suspensions and in ceramic paste samples.

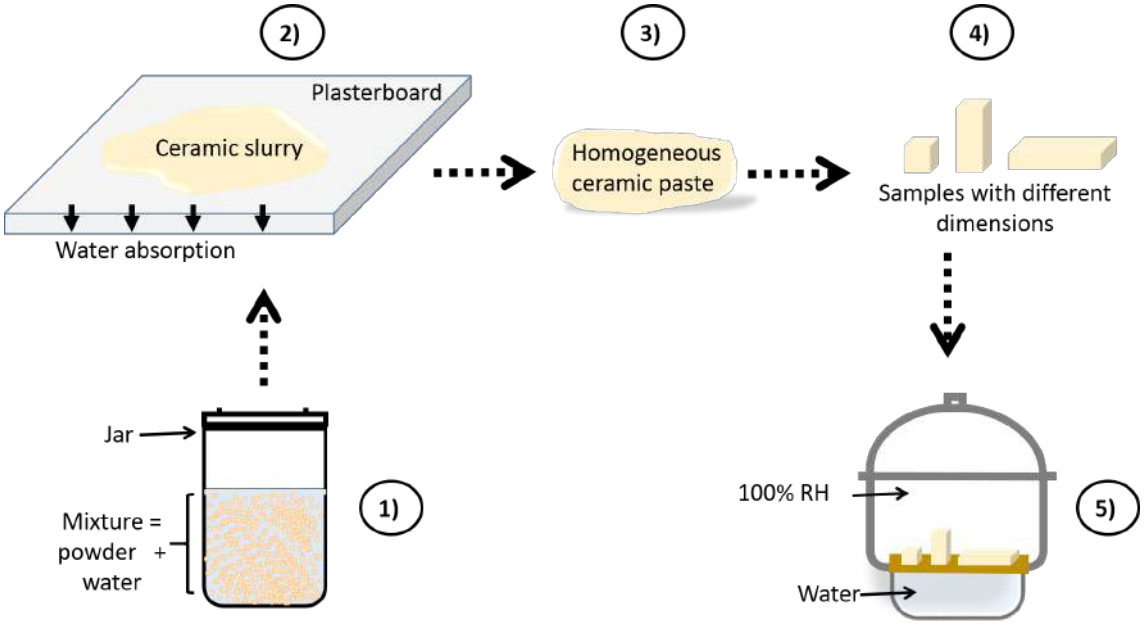

Figure 2.4: Representation of the different steps in sample preparation.

2.3 Characterization of drying behaviour

Measurements of the sample mass and dimensions as a function of time enables the drying rate, total duration and shrinkage to be assessed. Surface temperature measurement also gives useful information on the progression of drying of the ceramic green body. These characteristics are sensitive to the conditions of the surrounding atmosphere. Consequently, experiments have been made in the controlled atmosphere of a climatic chamber.

2.3.1 Experimental methods

2.3.1.1 Climatic chamber

An instrumented climatic chamber (MPC) was used to measure simultaneously the sample's weight and the dimension changes in one direction at a given temperature and relative humidity (figure 2.5). The temperature can be controlled between ambient temperature and 80 $°C$. The air humidity is controlled by using two temperature probes placed in the chamber which measure the dry and wet bulb temperatures. The difference between these temperatures allows the relative humidity to be calculated using the relation 1.5 presented in chapter 1. In order to increase the air humidity, the required water vapour is supplied by a boiler filled with water. When the relative humidity exceeds the set point, it is reduced by using a cooling unit connected to the chamber.

To investigate the length and weight variations of samples during drying, the climatic

chamber was instrumented with a Sartorius balance which has a sensitivity of 1 mg, and a Linear Variable Differential Transformer (LVDT) sensor 12K 006 supplied by Sensorex with an accuracy of $\pm$ 5 μm and a measuring range of 3 mm. Samples were placed on a support connected to the balance. The LVDT sensor was placed on the sample. Given the sensitivity of this measurement, the length sensor and the balance were connected along the same vertical axis (figure 2.5). In addition, an oil bath was used to seal the climatic chamber from the bottom part with the balance in order to maintain constant temperature and humidity. It is also worth noting that the oil bath allows some freedom of movement along the horizontal plane which can accommodate sample shrinkage without affecting the measurements of sample weight and length.

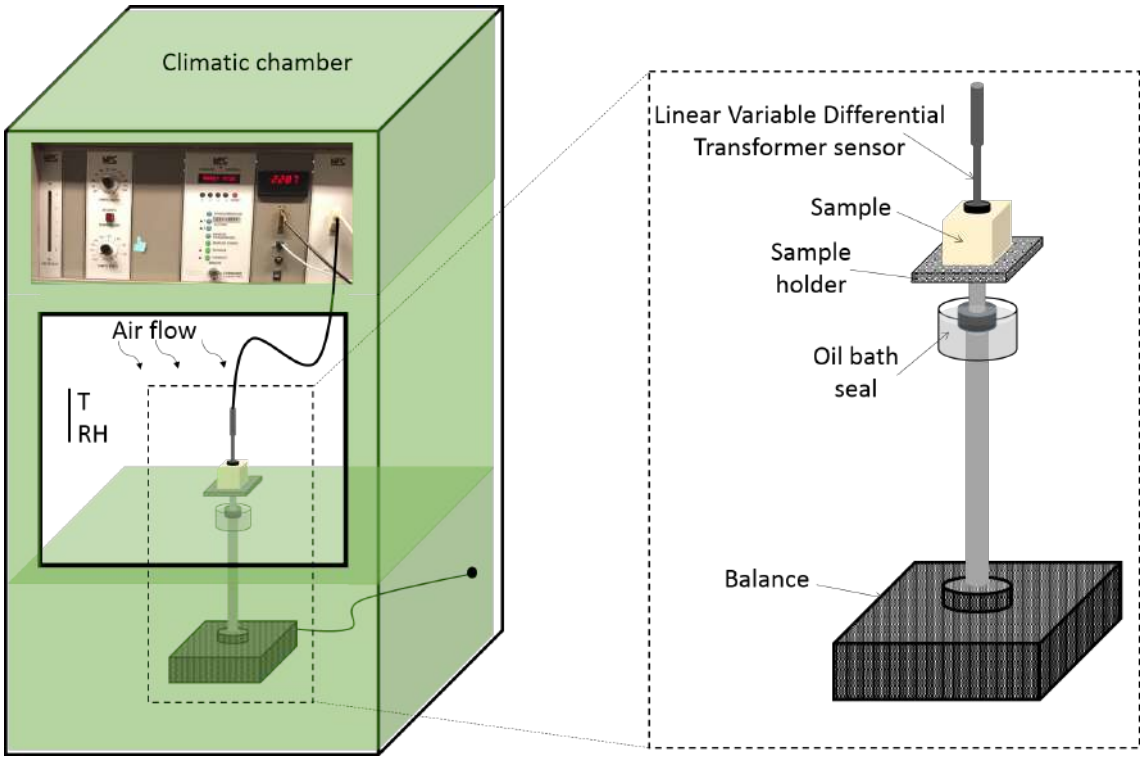

Figure 2.5: A schematic representation of the climatic chamber.

2.3.1.2 Non-contact temperature measurement at the sample surface

Monitoring of surface temperature during drying was performed using a IN-FRATHERM IN5 pyrometer which was placed within the climatic chamber (figure 2.6). Its accuracy in drying experiments was estimated to ca. $\pm$1 °C. Indeed, the pyrometer measures the radiated flux emitted by the sample in a range of wavelengths from 8 to 14 μm. Then by introducing the emissivity value of the material to be measured in the appropriate software, the surface temperature can be recorded. For the current study, the emissivity was determined for alumina and kaolin using the following method: a dry

sample was heated up to a known temperature measured with a thermocouple and the surface temperature was measured with the pyrometer using the emissivity as an adjustable variable until the output temperature was set to the known one. An emissivity value of 95% was estimated for alumina and 90% for kaolin.

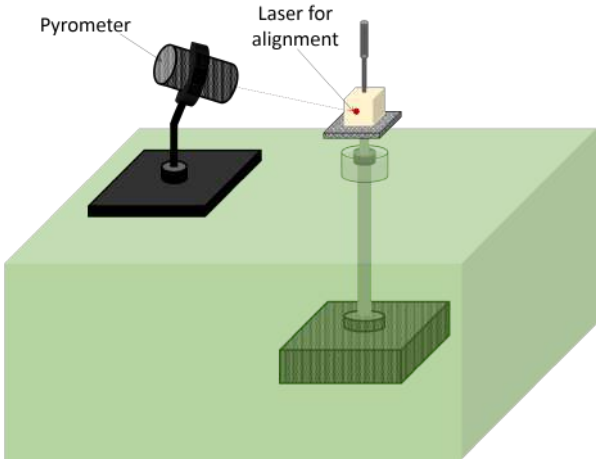

Figure 2.6: A schematic representation of temperature measurement at the sample surface.

2.3.2 Drying behaviour for alumina and kaolin pastes

Using the climatic chamber, similar cubic samples of 20 mm × 20 mm × 20 mm made from alumina and kaolin pastes were dried in the same conditions (30 °C and 63% of relative humidity). For each material, the sample weight, length and surface temperature changes over drying time were simultaneously measured. Then each sample was placed in an oven at 110 °C until a constant value is achieved in order to assess the dry weight. The moisture content and the shrinkage were then calculated using respectively the relations 1.1 and 1.17 presented in chapter 1.

The experimental results, plotted as a function of time, are shown in figure 2.7 and examined in the context of the different stages of drying described in the literature (chapter 1). The first stage called the constant rate period (CRP) is characterized by a constant rate per unit area of exposed surface and is clearly identified in the moisture content curves during the initial 5-6 hours for both alumina and kaolin. The transition to the subsequent stages of drying is pinpointed with more difficulty. However, during this period, where the exposed body surface behaves as a free water surface, the heat flow and the latent heat requirements of the evaporating water tend to establish a state of equilibrium witnessed by a constant temperature of the sample surface (T_s). For convective drying as in our case, this corresponds to the wet bulb temperature (approximately 26 °C). Before this is established, a brief transient regime is noticed which can be explained by the initial

sample preparation temperature (20 $°C$) which is less than either the oven temperature (30 $°C$) or the wet bulb temperature. Then when the drying rate slows down disrupting the evaporating surface equilibrium, a strong increase in T_s is observed. The surface temperature measurements thus give a valuable marker of the end of the CRP. This occurs at a moisture content of approximately 10% in the alumina sample and 12% in the kaolin sample.

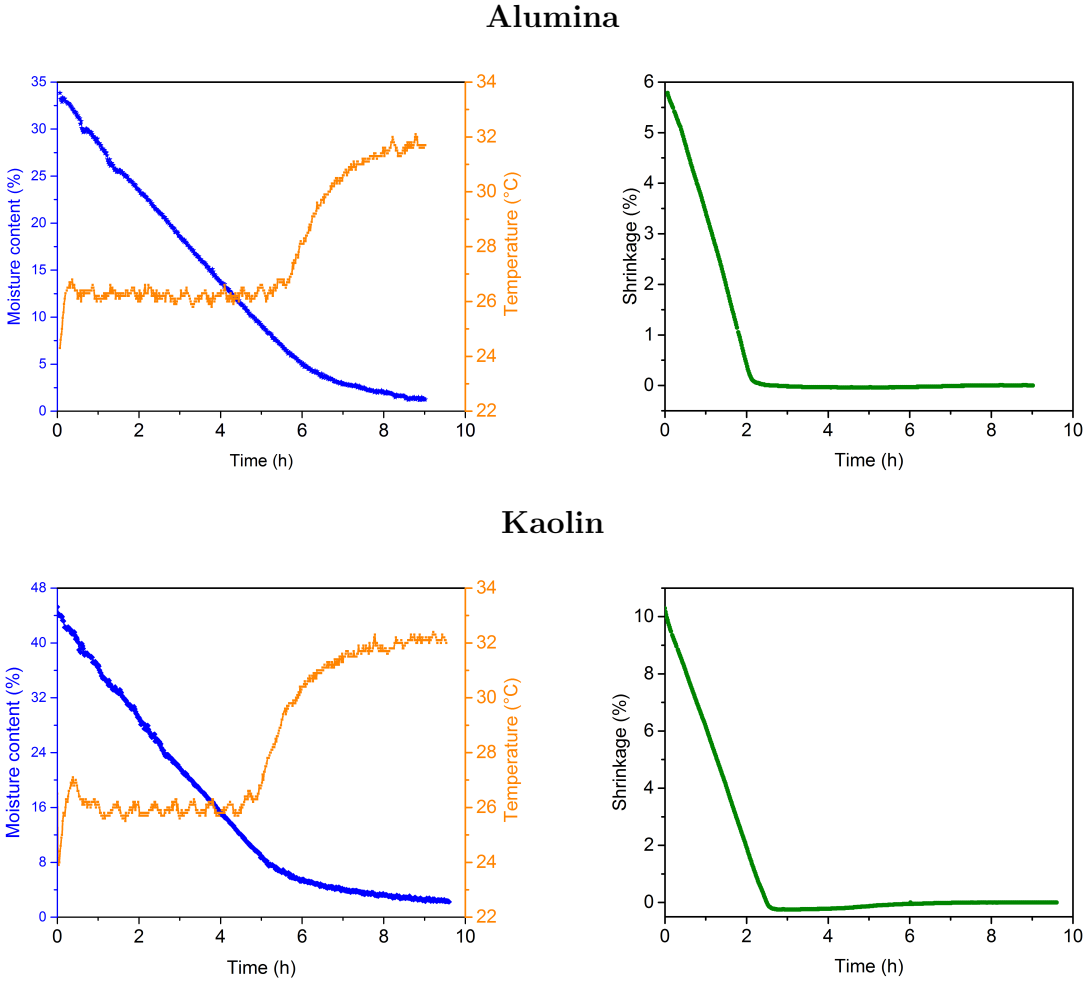

Figure 2.7: Moisture content, surface temperature and linear shrinkage as a function of time for alumina and kaolin samples dried at 30 $°C$ and 63% of the relative humidity.

The drying rate per unit area of exposed surface ($\phi_{C-exp-m}$) can be calculated from the mass loss-time data using the relation:

$$\phi_{C-exp-m} = -\frac{1}{S}\frac{\Delta m}{\Delta t} \tag{2.1}$$

where S is the surface area exposed to drying, Δm is the change in mass incurred in time interval Δt (30 min). Based on the curves in figure 2.7, the values for S have been corrected for shrinkage during the initial 2-2.5 hours. Plotted as a function of

moisture content in figure 2.8, similar drying rates are revealed for both the alumina and kaolin samples, especially during the CRP corresponding to moisture contents down to approximately 10%. This is consistent with drying of a free water surface, independent of the type of material and yields a value of 0.14 $g\ m^{-2}\ s^{-1}$. In the initial period of 2-2.5 hours, shrinkage is involved (down to approximately 25% of moisture content). In fact, a slight decrease in drying rate is detected during the later part of the CRP between 25% and 10% moisture content for kaolin, possibly imputed to slower transport of water to the evaporating surface. This aspect will be investigated further in chapter 4 with the evaluation of effective hydric diffusion. Furthermore, certain authors indicate that the end of shrinkage coincides with the end of the CRP [7, 32]. However, curves in figure 2.7 show clearly that shrinkage stops before the CRP is completed. This is explained by Suzuki and Maeda who proved that the drying rate tends to be constant even after the end of shrinkage when the distance between grains ($\sim$ pore size) is small compared to the thickness of the boundary layer [41].

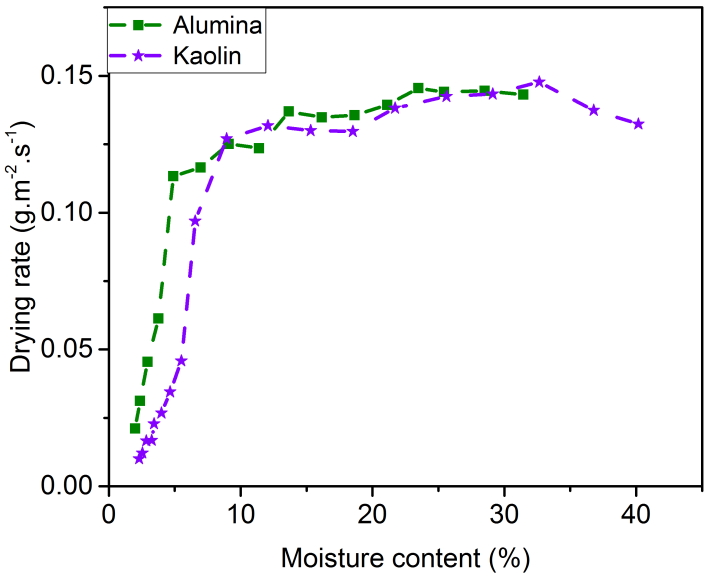

Figure 2.8: Drying rate as a function of moisture content for alumina and kaolin samples dried at 30 °C and 63% of humidity.

During the falling rate periods, the moist surface behaves no longer as a free water surface, and consequently the temperature of the body surface rises back up to the air temperature until the end of drying. The drying rate now decreases sharply towards zero for both alumina and kaolin. If drying of alumina and kaolin is similar during the first stage, this second period seems to present differences in behaviour. To illustrate, based on figure 2.8 the beginning of this period corresponds to different moisture contents within the green body. Thus if we conveniently consider drying to be complete when just 2% of

the residual water remains within the body, this FRP takes 4 hours for kaolin and 2h for alumina. This difference could be ascribed to the material nature. Ford explained that particles of ceramic oxides like alumina are considered as inert and do not interact with water during drying. That means the layers of water molecules around the particles are easier to remove. But with clay materials water molecules form a thick and stable film around the particles which slows down the evaporation of moisture [8]. However, Worrall in his book indicates that kaolin type clays can adsorb between 1 and 2% by mass of water which makes then difficult to associate differences in drying rates between alumina and kaolin only to the particles/water interactions [42]. Other factors which could play a role include: the granulometry, particle morphology and the pore fraction, pore size and shape. It can be noted that the original kaolin powder exhibits a higher specific surface area than the alumina powder, potentially promoting retention of water in the green body. The role of the material nature is explored in the next section with a study on drying of montmorillonite.

2.3.3 Drying behaviour of montmorillonite clay

Montmorillonite is known for its strong interactions with water and was chosen in order to investigate possible variations in drying behaviour. For this purpose, similar experiments as those performed for alumina and kaolin were made on montmorillonite paste. The drying was performed at 30 $°C$ and the relative humidity was controlled at 68%. The sample moisture content, surface temperature and shrinkage as a function of drying time are presented in figure 2.9. Although alumina and kaolin samples respect the description of drying stages in the literature, results for the montmorillonite sample show different behaviour. First it can be noted that the CRP is more difficult to distinguish during the initial part of the moisture content-time plot due to greater fluctuations. However the surface temperature measurements suggest that this period lasts 9 hours. Second the initial moisture content of the montmorillonite paste is much greater ($\sim$90%) than alumina or kaolin. Furthermore, shrinkage is now a continuous process throughout the entire drying duration (25 hours), including the falling rate period. It does not stop before the end of the CRP. These differences can be related to the nature of interactions between montmorillonite and water. The water is not only located between particles but also within particles, causing the perpendicular distance between equivalent planes (called the basal spacing) to increase from 10 to 15 $\AA$. On drying this results in greater shrinkage (33% for montmorillonite compared to 10% for kaolin) [42]. The extraction of water through drying is then more difficult and slower compared to alumina and kaolin. Using the convenient definition of 2% residual water for complete drying, this takes 25 hours in montmorillonite compared to 9.5 hours for kaolin and 8 hours for alumina. It can be concluded that although in most cases, the shrinkage stops during the first stage

of drying (case of alumina and kaolin), particular materials like montmorillonite interact more strongly with water. Then it becomes hard to relate shrinkage in a simple way to the different stages of drying.

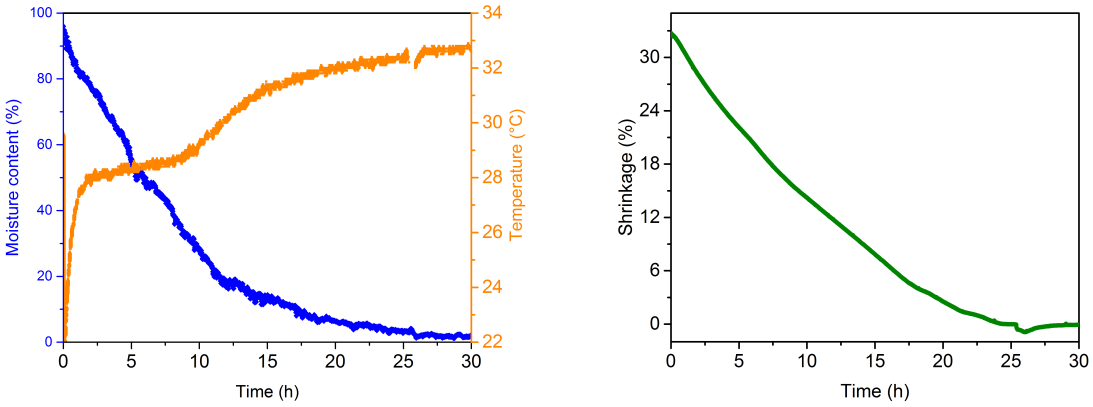

Figure 2.9: Moisture content, surface temperature and linear shrinkage as a function of time for montmorillonite sample dried at 30 $°C$ and 68% of the relative humidity.

2.3.4 Influence of the external conditions on the drying rate

In order to investigate the influence of drying conditions on the evaporation rates of alumina and kaolin materials, drying was examined for samples of the same geometry (cubes of 20 mm × 20 mm × 20 mm). These were dried at three different temperatures (30 $°C$, 40 $°C$ and 50 $°C$) with a constant water vapour pressure of approximately 2100 Pa which corresponds to different relative humidities (respectively 50%, 29% and 17%). Five faces were directly exposed to the drying atmosphere. The sample moisture content and the surface temperature as a function of time are presented in figure 2.10.

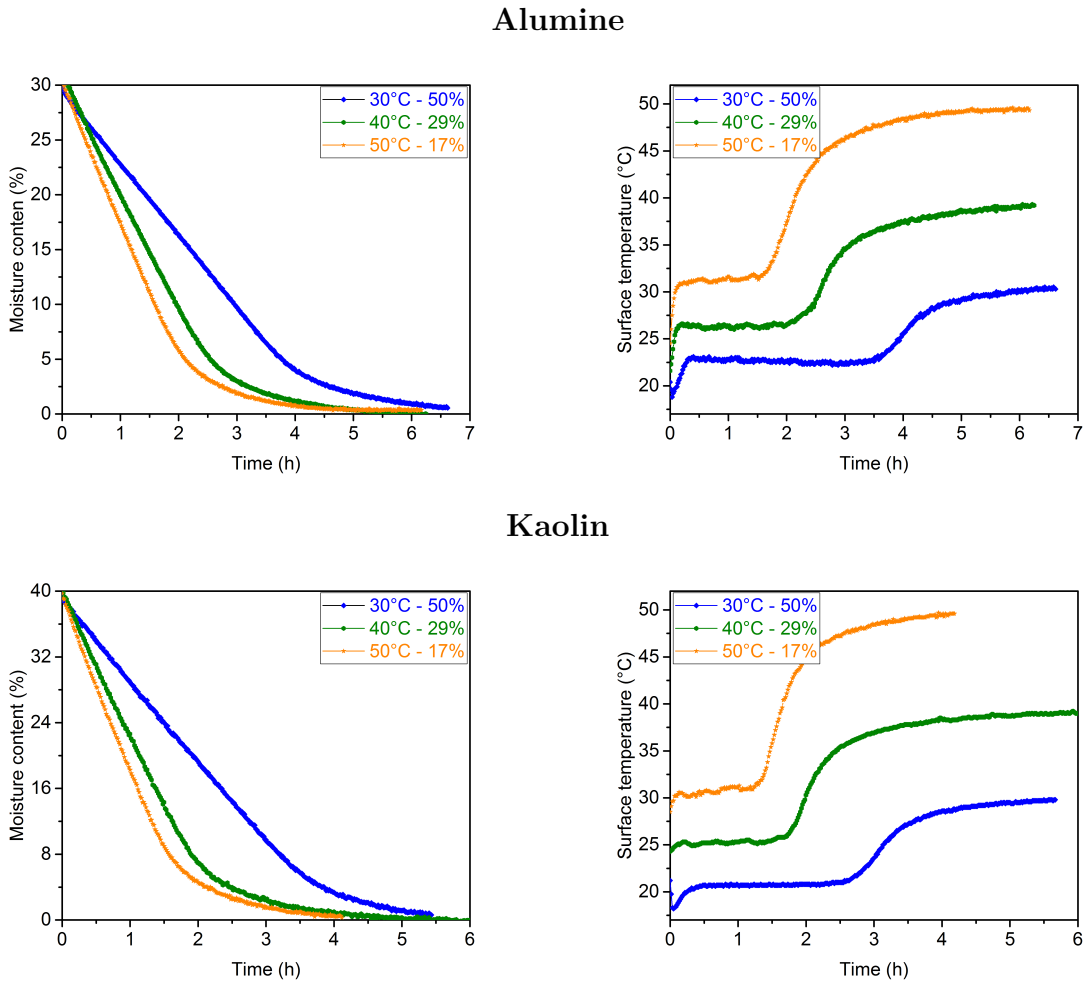

Figure 2.10: Normalized moisture content and surface temperature as a function of time for alumina and kaolin samples. Experiments were performed at different temperatures and relative humidity.

As stated earlier, the end of the CRP coincides with the increase of the surface temperature. Thus by extracting the duration of this period from the surface temperature curves, it can be noted on the moisture content curves that for the different conditions the end of the CRP corresponds to the same moisture content remaining within the samples (approximately 10% for alumina and 12% for kaolin).

Simple calculations of the drying rate during the CRP can be made using two different methods. First an experimental drying rate ($\phi_{C-exp-m}$) can be deduced from mass loss measurements using the relation 2.1. Then, since the surface temperature is measured, the drying rate ($\phi_{C-anal-T}$) during the CRP can be calculated re-expressing equations 1.9 and 1.10:

$$\phi_{C-anal-T} = -k(C_{air} - C_{s-bl}) = -k(RH\frac{P_s(T_{air})}{R\ T_{air}} - a_w\frac{P_s(T_s)}{RT_s}) \tag{2.2}$$

where $a_w = 1$ since during the CRP the surface behaves as a free water surface. As mentioned in chapter 1 the mass transfer coefficient k is related to the heat transfer coefficient h. A value of 40 $W\ m^{-2}\ K^{-1}$ was experimentally estimated for the heat transfer coefficient within the climatic chamber. The mass transfer coefficient can then be calculated using the relation 1.13.

On this basis, the drying rates for alumina and kaolin should be similar during the CRP and increase with surrounding air temperature. This trend is confirmed in the comparison of experimental values with calculated values in figure 2.11. As can be observed the drying rate increases linearly with temperature. The calculations base on equation 2.1 yield increases of drying rate by a factor of 1.8 between 30 $°C$ and 50 $°C$. However, theoretically speaking, the increase of the drying rate during the CRP when ambient conditions are varied can be calculated simply from the difference between air temperature and the wet bulb temperature. With this third calculation, the drying rate should increase by a factor of 2.5 from 30 $°C$ to 50 $°C$. This higher value compared to experimental results could be attributed to inaccuracy in the temperature measurement by the optical pyrometer or in the control of the relative humidity in the climatic chamber. In fact, the climatic chamber is sometimes unable to respect the set point conditions making the relative humidity difficult to control. The value of the water vapour of 2100 Pa was hard to maintain at 40 $°C$ and 50 $°C$. The data monitored by the climatic chamber for 40 $°C$ and 50 $°C$ are 32% and 24% respectively which correspond to water vapour pressure of 2350 Pa and 2940 Pa.

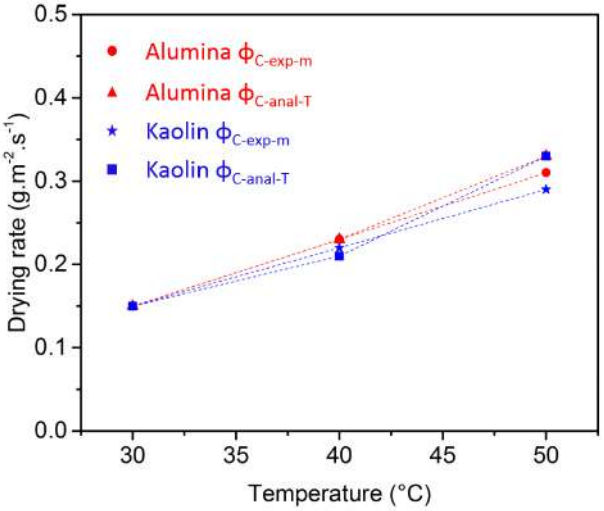

Figure 2.11: Drying rate as a function against temperature of drying for alumina and kaolin samples.

2.4 Evaluation of shrinkage

Maintaining dimensional control of the final ceramic object and avoiding the presence of defects is one of the main aims for industry. Thus, taking into account the shrinkage of green bodies during drying is of a strong importance since in some processing technologies like tape casting, as an example, a deviation from isotropic shrinkage occurs [5,6]. For that purpose, this part presents first the traditional Bigot curve representation for previous results (section 2.3.2) and then focuses on the assessment of anisotropic shrinkage in different orthogonal directions.

2.4.1 Bigot curve

The results of section 2.3.2 on the characterization of alumina and kaolin pastes are presented in the form of Bigot curves. As can be seen in figure 2.12, alumina and kaolin present two typical regimes as described in the literature (chapter 1). First, the initial weight loss is accompanied by major shrinkage. Then the second regime corresponds to the weight loss with minor shrinkage until the end of drying. This type of presentation is useful to identify graphically the change from one regime to another which is considered as a critical moment (leatherhard moisture content). This leatherhard moisture content is achieved when particles are in contact, herein it corresponds to ca. 23% for alumina and 25% for kaolin.

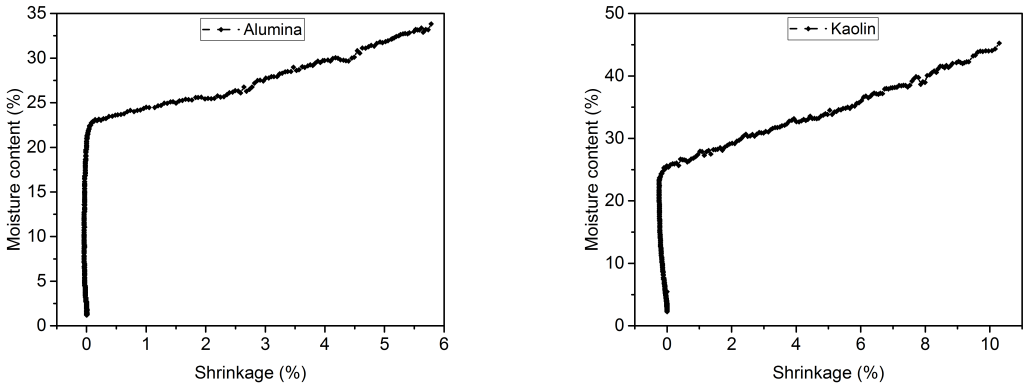

Figure 2.12: Bigot curves for alumina and kaolin samples dried at 30 $°C$ and 63% of the relative humidity .

At the end of the major shrinkage it can be assumed that the pores are completely saturated with water, which means that the volume of water at this moment corresponds to the volume of air at the end of drying. Thus the leatherhard moisture content can be an indicator of the porosity for the dry body. To illustrate briefly this idea, the Bigot curves can be used to investigate the behaviour of a paste when the formulation is varied.

For example, in traditional ceramics, it is usual to add grog particles to reduce the overall shrinkage of the paste. That is why two kaolin formulations were blended with water: BIP kaolin and a mixture of BIP kaolin and quartz (70% of kaolin and 30% mass of quartz) with larger grains (250 μm). The choice of quartz is due to its frequent use in formulations for traditional ceramics like bricks. The moisture content and the shrinkage of similar samples were followed in the same conditions of drying. The comparison in figure 2.13 shows that the overall shrinkage is reduced in the sample containing quartz particles (6% compared to 7% for pure kaolin). It can also be noted that the leatherhard moisture content for the sample with quartz particles is lower, approximately 20% compared to 25% for kaolin , which indicates that the sample containing quartz should have the higher density. In this respect, an estimate of the apparent density of each green body from the dry weight and measurement of the sample dimensions was made. The porosity was then deduced and was indeed lower for the mixture of kaolin and quartz (40%) compared to kaolin with 46%.

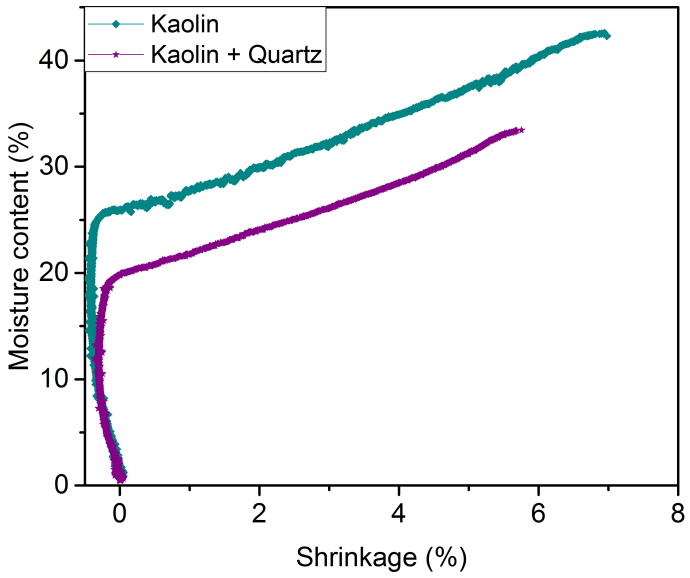

Figure 2.13: Bigot curves for kaolin and kaolin + quartz samples dried at ambient temperature (20 $°C$) without controlling the relative humidity.

2.4.2 Shrinkage in different directions

Considering now the shrinkage in different directions, we develop in addition to standard shrinkage characterization, a new optical method based on tracking of marks to measure shrinkage, simultaneously in two dimensions during drying. In fact, similar methods in the field of mechanics, have been developed to measure displacement

or strain field of a surface from digital images obtained using optical cameras. For example methods based on tracking of marks or on digital image correlation have been reported [43]. Furthermore, optical cameras have already been used to investigate drying of ceramics, for example to study crack formation in clay materials or to determine shrinkage in concrete samples [44, 45].

In this respect texturing of the ceramic green body was achieved by pressing the ceramic pastes (alumina and kaolin) in one preferential direction. Furthermore, for kaolin material extrusion was used as a second forming method. This method is well adapted for shaping plastic mixtures.

2.4.3 Verification of the sample shape influence

Before going further, a simple test of the effect of sample shape on the drying behaviour was made since we plan to deal with shapes other than cubes. Two simple geometries of alumina and kaolin pastes were examined: a cube of 20 mm × 20 mm × 20 mm and rectangular parallelepiped of 40 mm × 20 mm × 5 mm. Drying was performed in the same conditions (30 °C without controlling the relative humidity) and for both geometries the surface area with 5 faces exposed to drying was the same (20 cm^2). According to figure 2.14 which presents Bigot curves (a) and drying rates as a function of moisture content (b) for alumina material, we deduce that even if the volume to be dried is different for both shapes, the samples dry in a similar way in terms of overall shrinkage and evaporation rate. Drying behaviours were also similar for kaolin samples.

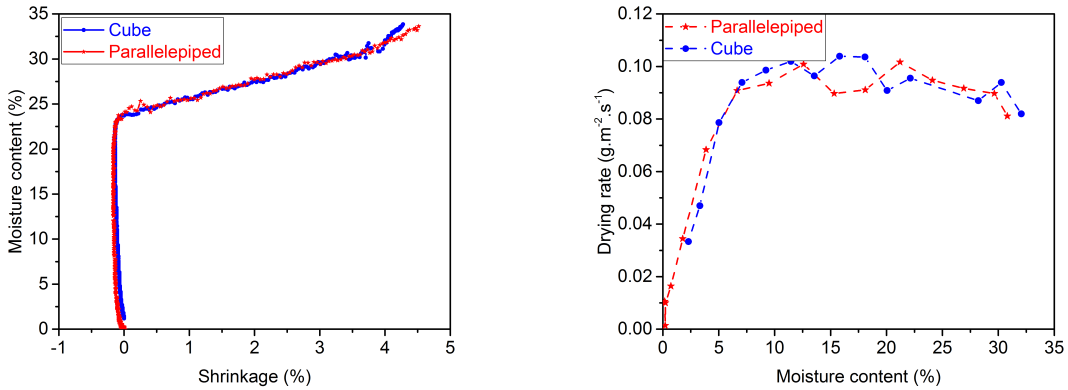

(a) (b)

Figure 2.14: a) Bigot curves for alumina samples with different geometries (cube and rectangular parallelepiped) dried at 30 °C without controlling the relative humidity. b) Corresponding drying rate as a function of moisture content.

2.4.4 Shaping methods to investigate anisotropic behaviour

2.4.4.1 pressing method

Before each measurement, a portion of the paste was extracted from the ceramic paste and pressed in one direction. Then the samples were cut with the dimensions of 20 mm × 20 mm × 7 mm as illustrated in figure 2.15.

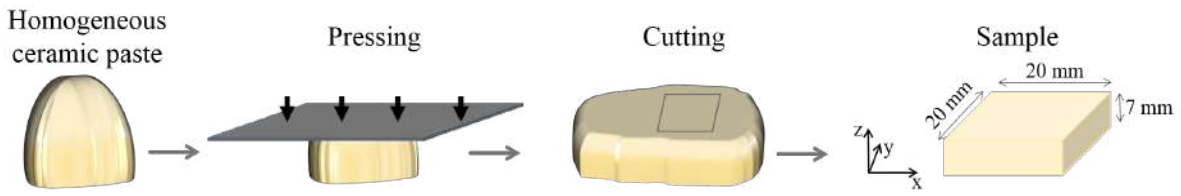

Figure 2.15: Schematic description of the different steps of sample shaping by pressing.

2.4.4.2 Extrusion method

In this method, the kaolin paste was extruded in a cylindrical form (diameter of 20 mm) with a piston extruder as illustrated in figure 2.16. The kaolin paste was placed in a reservoir and then was pushed through a die by a piston. Furthermore, a vacuum pump was connected to the die in order to remove air bubbles. After extrusion, the paste was cut into cylinders with 20 mm of height. These were then cut into half cylinders in order to measure simultaneously the height and diameter.

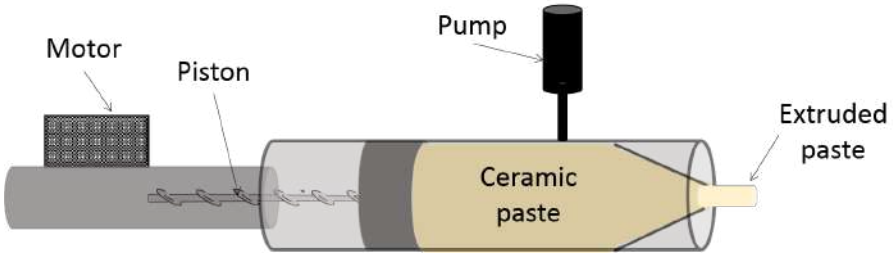

Figure 2.16: Schematic of the sample shaping by extrusion.

2.4.5 Experimental methods

Monitoring the variation of sample dimensions in different directions simultaneously with measurement of the weight loss as a function of time during drying was performed using two different methods.

2.4.5.1 1D measurement

The first method is the standard one using a BC220M Precisa balance which has a sensitivity of 1 mg and Linear Variable Differential Transformer (LVDT) sensor similar to that one used in the climatic chamber. The device used in these experiments has a measuring range of 6 mm with a resolution of 5 μm. The experimental set-up is illustrated in figure 2.17. With this equipment, three experiments were performed with different sample orientations, to obtain shrinkage in three orthogonal directions.

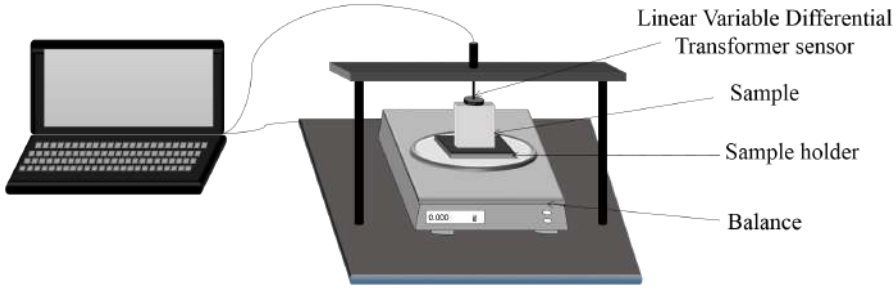

Figure 2.17: Schematic representation of the experimental setup for shrinkage measurement in 1D.

2.4.5.2 2D measurement: optical method

The measurements were performed with the use of a similar $BC220M$ Precisa balance, and a uEye SE camera supplied by IDS with a resolution of 2590 $\times$ 1920 pixels. With this method, the variation of sample dimensions was identified simultaneously in two directions during drying. Schematic representation of this experimental set-up is given in figure 2.18. The sample was placed on a support which was lubricated with oil to avoid mechanical stresses resulting from adhesion with the support during drying. For pressed pastes, each material, alumina and kaolin, was measured with two different sample orientations in order to monitor the variation of dimensions in three directions (figure 2.19 a). For extruded samples only one configuration was used (figure 2.19 b). Several colored full circles were marked on the sample surface before starting the measurement as shown in figure 2.19. Then the images and the sample weight were recorded every 5 minutes.

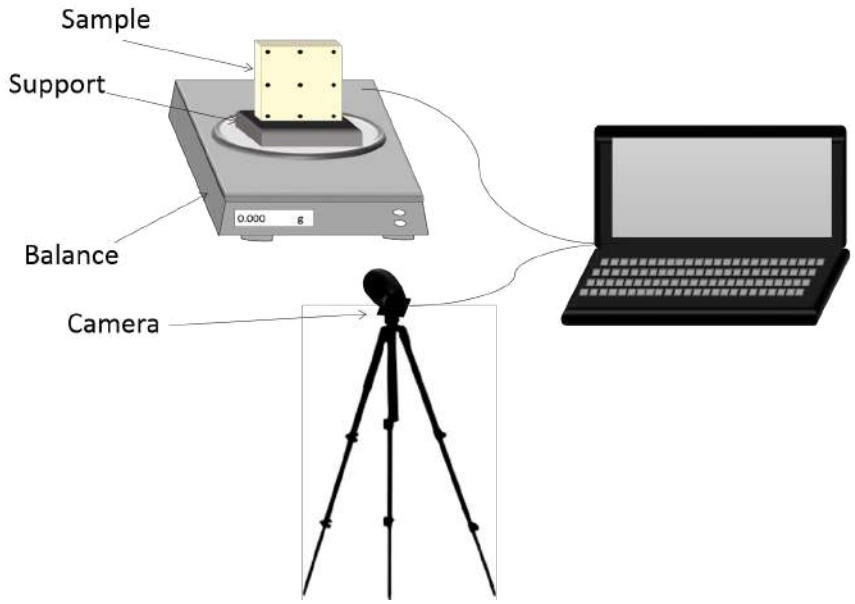

Figure 2.18: a) Experimental setup for shrinkage measurement in 2D.

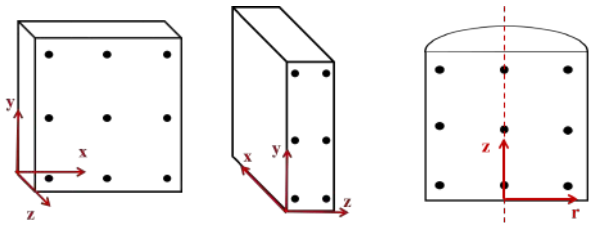

(a) (b)

Figure 2.19: Schematic representation of experiments to measure shrinkage in all directions (with full circles on the observed face). (a) for pressed samples and (b) for extruded samples.

In order to accurately determine the sample dimension changes in two directions, the distances between the full circles of images were evaluated with the use of a program written in python. Image analysis typically involves different steps. The first step corresponds to cropping of images in order to focus the analysis on the sample surface (figure 2.20 a and b). Then as the images were taken at different times during drying and the sample state changes with water removal, the lighting conditions were not the same. For that reason, a specific adaptable threshold was used. Then a blur function was applied to the images in order to detect the full circle contours and their centers (figure 2.20 c and d). Based on the distance values between the pairs of the full circles for each image during drying L(t) and those of the last image which corresponds to the dry sample L_d, the shrinkage (Sh) in two orthogonal directions was calculated using the relation 1.17. For

each direction, the shrinkage was evaluated by taking an average value over all the pairs of full circles. Furthermore, since the sample shrinkage is in three orthogonal directions, the resolution of the pixels per unit length number changes slightly. A correction was made to take this effect into account. According to the obtained sample mass m, the water content X was calculated with the relation 1.1 of chapter 1.

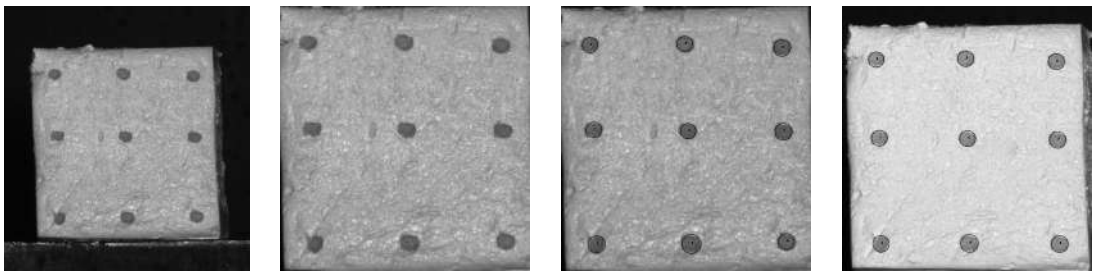

(a) (b) (c) (d)

Figure 2.20: Representation of the different steps of image analysis for square shaped samples of kaolin. a) Raw image. b) Image cropped to the sample surface. c) Contour detection at the beginning of drying. d) Contour detection at the end of drying.

2.4.5.3 Microstructure observations

A Scanning Electron Microscope (SEM), type FEI Quanta 450 FEG, was used to observe the microstructure of the samples. Before the observations, samples were dried in an oven at 110 $°C$ for 24 hours to ensure complete water removal. Then they were fractured in order to observe two cuts: the perpendicular and the parallel cuts to the pressing direction or the extrusion direction.

2.4.6 Results

For all measurements, the drying of samples was evaluated in similar conditions, i.e. at room temperature (20 °C), and ambient relative humidity with the same surface exposed to drying. Then after complete drying in an oven at 110 °C, shrinkage Sh and water content X were calculated using equations 1.17 and 1.1, respectively.

2.4.6.1 Shrinkage of alumina samples

The Bigot curves in x, y and z directions were established for drying of alumina samples. It can be noted that from the beginning of drying, the shrinkage for each direction decreases linearly with water loss down to 24% of water content within the sample and then exhibits a negligible variation until the end of drying. Also based on

figure 2.21, we can distinguish different amounts of shrinkage depending on directions. It is identical in x and y directions (ca. $\sim 4\%$) but increases in the z direction (ca. $\sim 5\%$) for both the LVDT and optical measurements. This difference in the overall shrinkage as a function of water content, corresponding to a factor of 1.2 between the z direction and the other directions can be explained by the nature of the raw material and the sample preparation. In fact, pressing a paste of isometric grains should not yield any preferential orientation. Accordingly, shrinkage in the three orthogonal directions should be similar. This is not quite the case here, since alumina particles are not strictly isometric as shown in figure 2.1. Therefore, to investigate further the preferential orientation, we present in figure 2.22 two SEM images corresponding to cuts perpendicular (figure 2.22 a) and parallel (figure 2.22 b) to the pressing direction. The observations confirm that grains are not perfectly isometric and seem to be oriented as shown in figure 2.22 a with larger surface area of grains compared to figure 2.22 b. This may explain a slight anisotropy in shrinkage for these alumina samples.

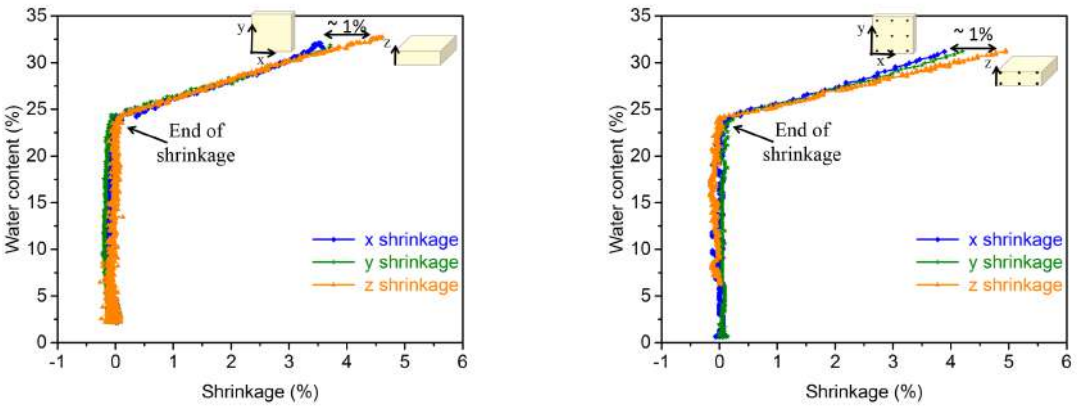

Figure 2.21: Bigot curves for pressed samples of alumina dried at room temperature and in conditions of ambient relative humidity for three orthogonal directions obtained with the LVDT sensor (left) and the optical method (right).

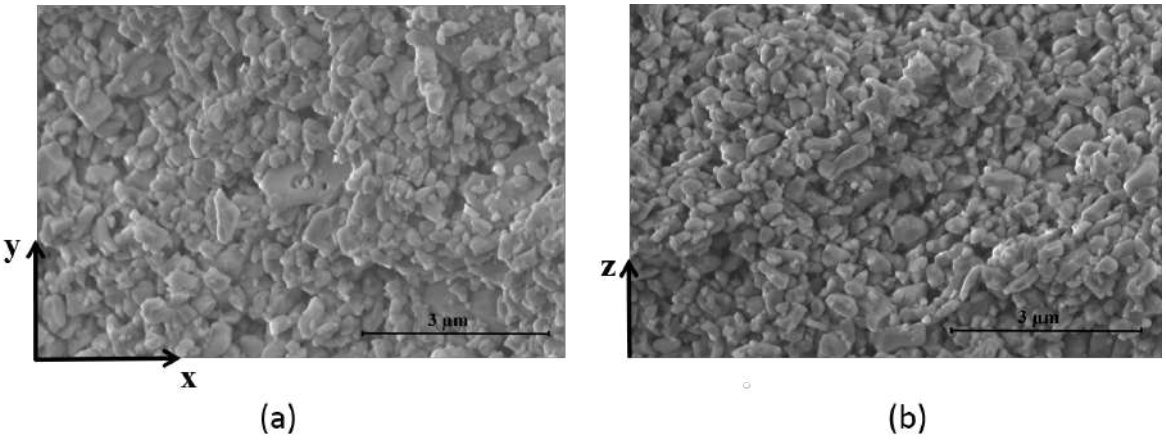

Figure 2.22: SEM micrographs on fractures of the alumina samples completely dried in at 110 $°C$. a) observation of the perpendicular cut to the pressing axis. b) observation of the parallel cut to the pressing axis.

Anisotropic shrinkage behaviour is an interesting feature to elucidate and that can be investigated on materials with more anisometric grains. The next step is then studying kaolin clay with tabular grains.

2.4.6.2 Shrinkage of kaolin samples

Both methods were also used to establish Bigot curves in three orthogonal directions for kaolin samples (figure 2.23). Initially the water content within samples is the same (44%). Results show that the mass loss is linear with shrinkage until the water content reaches approximately 24%. Shrinkage then becomes negligible in the three directions simultaneously. The main difference compared to curves obtained for alumina samples is that variation in the overall shrinkage for the three directions yields a wider interval, between 6% and 11%. This corresponds to a factor of 1.8 between the z direction and the other two directions. Similar to alumina samples, greater shrinkage is still observed in z direction. Indeed, since the kaolin grains have a tabular form, we assume that a preferential orientation of grains due to pressing could correlate with the higher shrinkage value in the z direction.

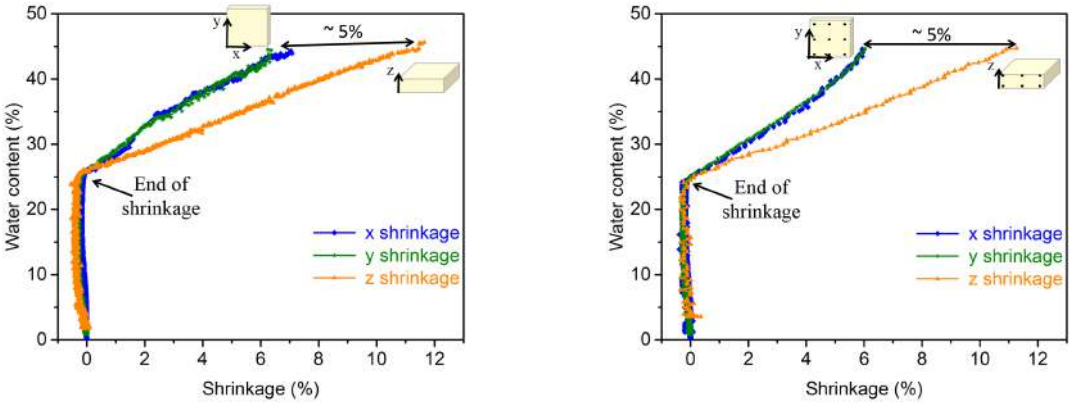

Figure 2.23: Bigot curves for pressed samples of kaolin dried at room temperature and in conditions of ambient relative humidity for three orthogonal directions measured with the LVDT sensor (left) and with the camera (right).

In order to investigate further the preferential orientation of kaolin platelets due to the pressing step, we present two SEM images corresponding to cuts perpendicular (figure 2.24 a) and parallel (figure 2.24 b) to the pressing direction. In figure 2.24 a, tabular shaped grains can be observed without noticeable preferential orientation which is in accordance with similar shrinkage values measured in x and y directions. However, in figure 2.24 b, stacking of the kaolin platelets along the z direction can be observed with basal planes oriented perpendicular to this direction. Based on these observations, the higher shrinkage revealed in z direction can then be explained by this preferential orientation with a higher number of grains/water interfaces per unit length in this particular direction. At the beginning of drying the platelets are surrounded by liquid water as illustrated in figure 2.25 a. The number of water layers per unit length is higher along z than in the other directions and consequently the removal of the water layers leads to greater shrinkage along z (figure 2.25 b). Based on a grain size of 4 μm in x-y plane, a simple estimate of the starting water film thickness, in case of perfect orientation, is 200 nm. This is consistent with earlier work by Ford who discussed the anisotropy in shrinkage behaviour of clay materials, explaining that when the number of water films per unit length is different in the two directions, the shrinkage is also different [8]. In the real situation, the distribution of particle sizes and orientations should be taken into account.

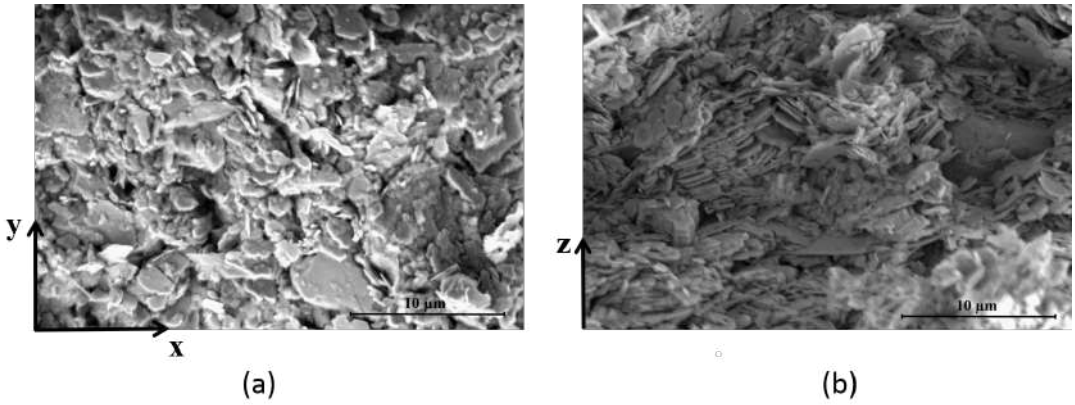

Figure 2.24: SEM micrographs on fractures of the kaolin samples previously dried at 110 $°C$. a) observation of the perpendicular cut to the pressing axis. b) observation of the parallel cut to the pressing axis.

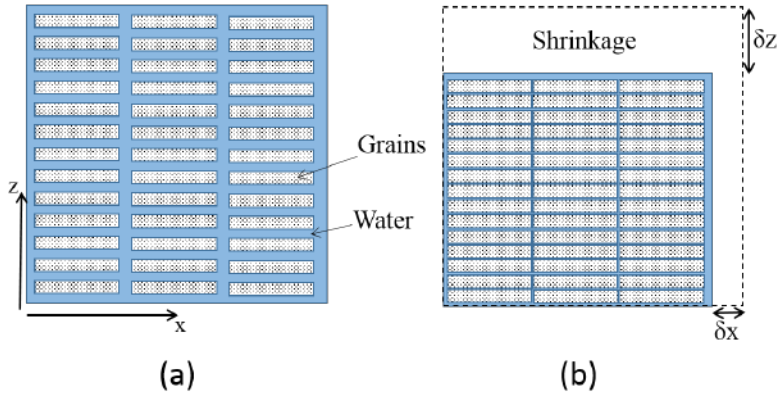

Figure 2.25: Schematic arrangement of grains with the same number of grains. a) At the beginning of drying. b) At the end of major shrinkage.

Given that kaolin clay is frequently used in plastic mixtures and exhibits particles with tabular form, it was of strong interest to follow the evolution of the shrinkage using a second common shaping method in ceramic processing which is extrusion. Since the samples with this shaping method had a cylindrical shape, the shrinkage was determined for the radial direction and along the extrusion axis (figure 2.26). It was noted that due to a preferential orientation of grains which is observed in SEM images (figure 2.27), the amount of shrinkage along a radial direction is similar to the shrinkage in the z direction for the pressing method. Whereas the direction that corresponds to the extrusion axis exhibits fewer grain/water interfaces. A possible arrangement of particles is presented in figure 2.28.

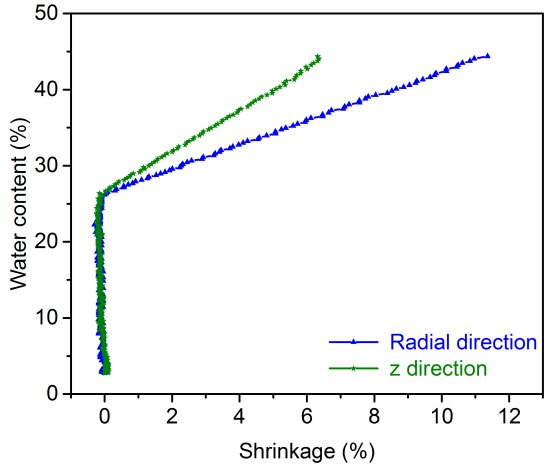

Figure 2.26: Bigot curves for extruded samples of kaolin dried at room temperature and in conditions of ambient relative humidity for the radial and z (height) directions measured with the camera.

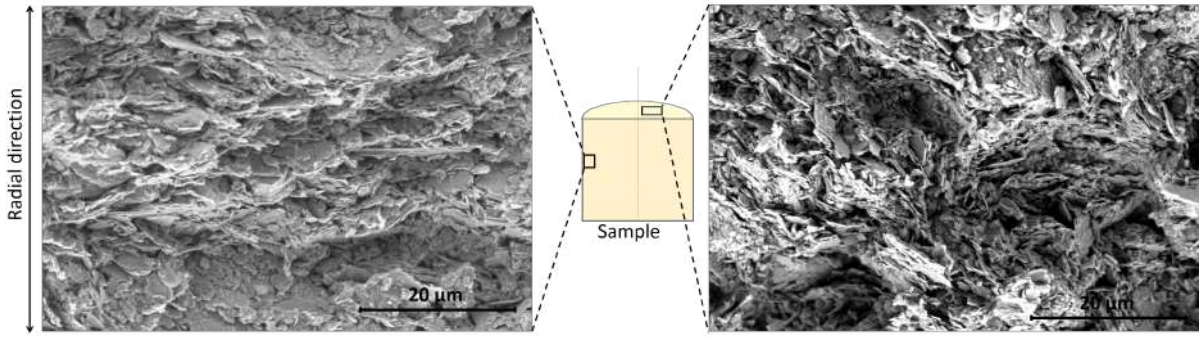

Figure 2.27: SEM micrographs on fractures of the kaolin samples previously dried at 110 $°C$. Observation of the perpendicular and parallel cuts to the extrusion axis.

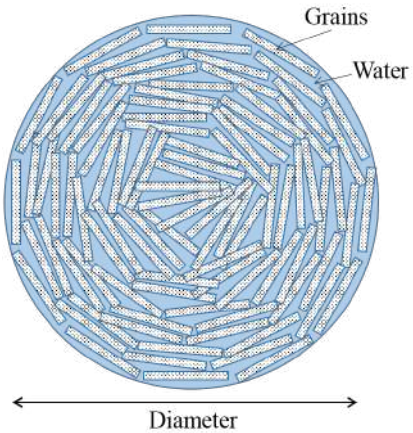

Figure 2.28: Schematic of a possible arrangement of grains for extruded cylinders.

2.5 conclusion

Using an experimental approach, the macroscopic drying behaviours of three different ceramic pastes: alumina, kaolin and montmorillonite were examined in this chapter.

In the first part, surface temperature, moisture content and the length changes have been monitored for samples of similar dimensions in the same air conditions (constant temperature and relative humidity). Referring to the different stages of drying described in the literature, no difference was observed in the drying rate between alumina and kaolin during the CRP. However the second stage of drying, known as the FRP took more time in the case of kaolin clay compared to alumina. This can be related to the interactions between clay particles and water as explained in the literature by Ford [8]. In order to investigate this further, the drying behaviour of a third material 'montmorillonite' was characterized in the same conditions. In the case of montmorillonite, which is a swelling clay, water interacts strongly with the particles. It is located between particles and also within the particle itself. As a consequence, its extraction from the green body during drying is slower and takes longer time. Shrinkage can not be related in a simple way to the different stages of drying. Finally an increase of the surrounding air temperature was shown to increase the evaporation rate, and as expected reduce the overall drying time.

The second part was dedicated to the assessment of shrinkage in different directions during drying of ceramic pastes. An optical method based on tracking of marks was developed to measure linear shrinkage simultaneously in two dimensions. To illustrate the interest of such a method in the field of ceramics, kaolin and alumina pastes were characterized. Results obtained with this method are found to be in good agreement with those obtained with a LVDT sensor which is the more conventional method. We have also shown that pressing or extruding a ceramic paste could lead to strong anisotropic shrinkage. For instance, the overall shrinkage of kaolin in the pressing or extrusion direction is 1.8 times greater than in the other directions, while for alumina it is significantly less. The anisotropic shrinkage is related to the orientation and morphology of grains inducing a larger water/solid ratio along one direction compared to the other two orthogonal directions.

Chapter 3 :

Multi-scale study of the moisture distribution

Chapter context

The mechanisms controlling the drying rate of ceramic green body discussed in the chapter 2 imply that changes in the concentration and distribution of water occur during the process. A fundamental question is then: where is the liquid physically located during drying? To answer, the present chapter characterizes the distribution of water within the ceramic green bodies during drying at different scales. First, experimental measurements using a simple weighing technique gives data at the cm scale. Then modern techniques such as Magnetic Resonance Imaging (MRI) and Environmental Scanning Electron Microscopy (ESEM) were used in order to examine the spatial distribution and the localization of water at the mm and grain scales. Such information is useful for the construction and testing of a robust numerical model to describe the drying behaviour of a ceramic green body. Most of the results presented in this chapter have been published in the paper: "Distribution of water in ceramic green bodies during drying" by S. Oummadi et al. *Journal of the European Ceramic Society 39 (2019) 3164–3172*

3.1 Experimental methods

3.1.1 Macroscopic scale ($\sim$ cm): weight loss measurements

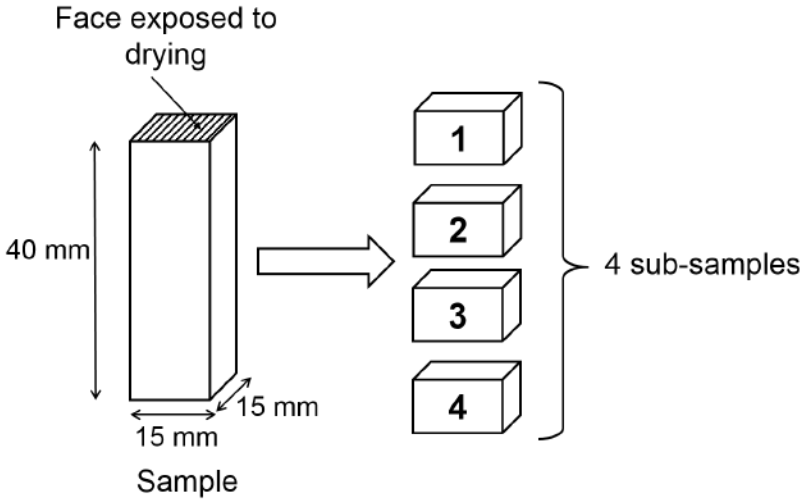

Figure 3.1: Representation of the sample divided into 4 blocks.

The evolution of moisture content in alumina and kaolin green bodies was followed at different positions as a function of time with the following procedure. Drying was performed in an oven at temperatures of 40 °C and 70 °C. The partial pressure of water was measured in the room using the wet bulb temperature and was assumed to be the same in the oven at both temperatures. The relative humidity was then estimated at 15% for 40 °C and 5% for 70 °C. The sample (15 mm $\times$ 15 mm $\times$ 40 mm) was placed in

the oven. Only one face (15 mm $\times$ 15 mm) was exposed to drying and the other faces were covered with polyvinyl film in order to ensure water transfer in one direction. Then the sample was removed at a precise time t and cut into four sub-samples (figure 3.1). Afterwards, the weights of the different sub-samples were measured before the sub-samples were placed in the oven for 24 hours at 110 °C. Their weight was then measured again after complete drying. The moisture content of each sub-sample at time t was calculated with respect to the dry basis using the relation 1.1.

3.1.2 Macroscopic scale ($\sim$ mm): Zero Echo Time (ZTE) Magnetic Resonance Imaging (MRI)

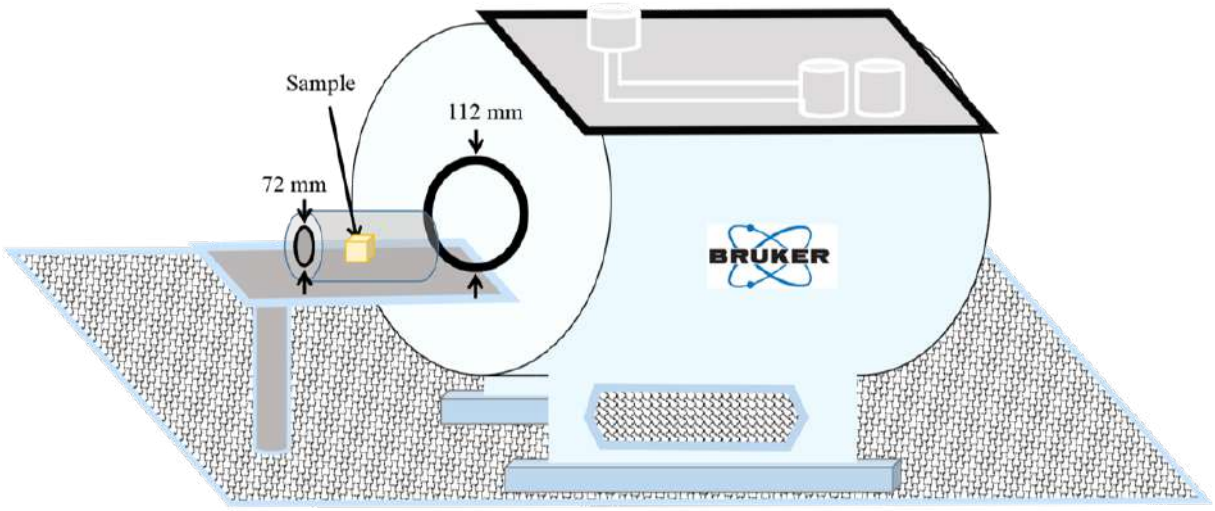

Figure 3.2: A schematic representation of the MRI machine.

As a complement to the weight analysis, Magnetic Resonance Imaging (MRI) measurements offer further information at a smaller scale with better than mm resolution. This approach is able to provide useful information about water distribution at different depths inside the ceramic body. In the present study carried out at the University of Bremen with the supervision of Prof. Wolfgang Dreher and Prof. Kurosch Rezwan, MRI measurements were conducted by an optimized Zero Echo Time (ZTE) MRI pulse sequence [46–48] implemented on a 7-Tesla preclinical MRI system (Biospec 70/20, Bruker Biospin GmbH, Ettlingen, Germany (figure 3.2)). The ZTE method was chosen for the MRI study of water in ceramic samples because of the very short effective transverse relaxation times (T_2*) involved. Background signals originate from NMR hardware components (e.g., supporting material and electronic parts of the RF coil) outside of the Field-of-View (FOV) and thus unwanted wave-pattern image artefacts were removed by applying an Outer Volume Suppression (OVS) module prior to RF excitation

of the sample [49]. In ZTE-MRI, for a series of measurements with short repetition time TR, data are acquired from the whole sample but with different orientations of the applied magnetic field gradient, allowing the reconstruction of a 3D image. In this study, ZTE MRI was performed with a FOV of 48 $\times$ 48 $\times$ 48 mm^3 and a matrix size of 128 $\times$ 128 $\times$ 128, yielding a voxel size of 375 $\times$ 375 $\times$ 375 μm^3. Using a TR of 11.3 ms and 51896 data acquisitions, the total measurement time per 3D image was about 10 minutes.

Image reconstruction was performed on the MRI console using the software Paravision 5.1 provided by the manufacturer. The 3D MR images were reconstructed by a gridding algorithm to determine the data on a Cartesian grid from the radially sampled k-space data, followed by a 3D Fast Fourier Transformation. It is important to note that some intensity distortions may occur in ZTE images, i.e. a non-uniform intensity distribution may be reconstructed for a uniform object. These image artifacts can be caused by experimental problems (missing or distorted signals near the k-space center acquired immediately after switching from transmission to reception mode [48]; influence of OVS [49]) or by data reconstructions (aliasing artifacts or incomplete deapodization to suppress aliasing artifacts) [50, 51]. In MRI applications that focus on the detection or delineation of objects or structures, such intensity distortions are of minor importance. However, for quantitative data evaluation performed in this study, an intensity recalibration was used assuming a uniform signal distribution at the beginning of the drying process.

3.1.3 Microscopic scale: microstructure observations by ESEM

In order to obtain information on the location of water during drying at the grain scale, observations were made on alumina and kaolin samples using an Environmental Scanning Electron Microscope (ESEM), model Quanta 450 FEG, supplied by FEI. The relative humidity was controlled close to the sample surface, and reduced step by step from 100% to observe the effect of drying. The temperature of the sample holder was set to 2 °C, and the water vapour pressure in the chamber to 700 Pa which corresponds to 100% relative humidity. Reducing the pressure below 700 Pa then decreases the relative humidity.

3.2 Results

3.2.1 Alumina P172SB samples

3.2.1.1 Weight loss

- Drying at 40 °C and 15% RH:

Based on the macroscopic scale measurements, the moisture content for each sub-sample of the alumina P172SB samples as a function of time are shown in figure 3.3.

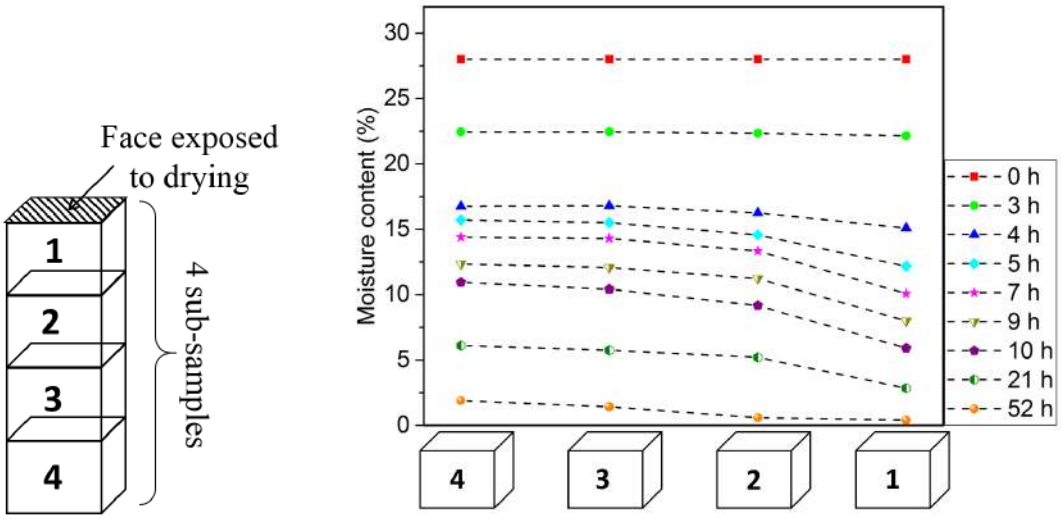

Figure 3.3: Water content of alumina P172SB sub-samples after different drying times, at 40 °C and 15% RH.

The situation and mechanisms described in chapter 1 can explain the distribution of the water within the ceramic green body during drying. At the beginning of drying, the material should be constituted uniquely of the solid and water. It can be seen that the water distribution is uniform throughout the sample as shown in the first profile of figure 3.3 (0 h). Two periods of drying can be distinguished: the first one lasts approximately 3 hours which coincides with the major shrinkage (down to approximately 23%) and the second corresponds to the rest of the drying time. In the situation of slow drying, involving higher relative humidity and temperatures close to ambient, a continuous layer of water covers the surface of the sample throughout the shrinkage period. Then the water evaporated from the surface and physical movement of the liquid/air interface leads to a redistribution of the water/particle system to maintain a uniform water concentration. In our study with one side exposed to drying, it is observed in figure 3.3 that even after 3 hours of drying, the water content in the four sub-samples

remains the same. However for drying duration of 4 hours or more, a gradient in water concentration occurs. We have shown in chapter 2 that the CRP ends for water content of approximately 10%. Concentration gradients then appear during the CRP after the end of major shrinkage. The concentration gradient reaches a maximum after 10 hours. There is a difference of 3.2% in the water content between sub-samples 1 and 2 while sub-samples 3 and 4 reveal only a small difference (0.5%). As the outer part of the ceramic green body becomes completely dry, the steepest part of the gradient (drying front) moves towards the interior as shown by the curve obtained after 52 hours.

The next series of experiments tested this general picture of water distribution for faster drying at higher temperature on a similar set of alumina samples.

- Drying at 70 °C and 5% RH:

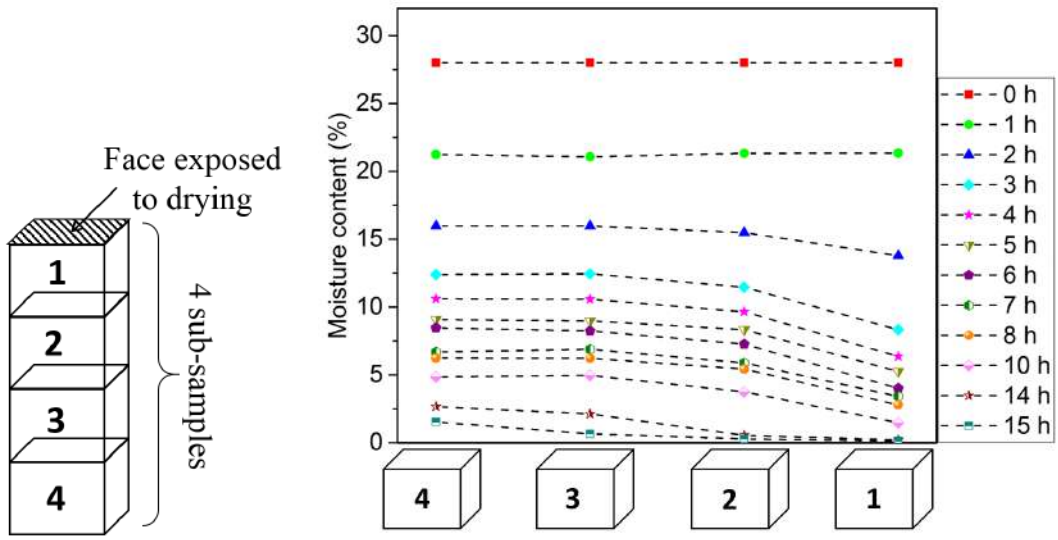

Figure 3.4: Water content of alumina P172SB sub-samples after different drying times, at 70 °C and 5% RH.

Figure 3.4 reveals similar but faster drying behaviour at 70 °C as at 40 °C. Only 15 hours of drying were required to reduce the moisture content to $< 2\%$ versus 52 hours at 40 °C. It can be noted that the maximum difference in water contents between sub-samples 1 and 2 is the same at 70 °C as at 40 °C (approximately 3.2% after 6 hours of drying). However, it is stated in the literature that a "faster" evaporation of water at the body surface yields larger concentration gradient, since the surface is supplied slowly by water migrating from deep below the surface. In fact, a study on drying of large plastic bodies (18 cm) shows that differences in water concentration become more and more pronounced within the sample when the rate of evaporation from the surface

is increased by a factor of 3 [8].

The next series of trials examine the distribution of water during drying with the higher spatial resolution of MRI.

3.2.1.2 ZTE Magnetic Resonance Imaging

In the present section MRI images of the materials at various stages in drying are presented in figure 3.5. Three slices were chosen in order to illustrate how water is distributed within materials at different positions (from the top to the bottom). In this sample, only one face is exposed to the drying atmosphere while the others are covered with a plastic film. So in this situation the water migration should principally be in one direction. The first observation shows that the pixel intensity in the images for the top, middle and bottom positions, is greatest at the beginning of the drying process (1st column in figure 3.5). Then as drying progresses, the gray levels decrease, meaning that the amount of water decreases. Moreover, the images clearly reveal the phenomenon of shrinkage by the reduction of area of the squares during drying. For example, the square size at the beginning is about 4 cm^2 reducing to 3.69 cm^2 after drying is achieved. It corresponds to approximately 4% of linear shrinkage,which is close to the value obtained in the second chapter using the LVDT sensor and the optical method.

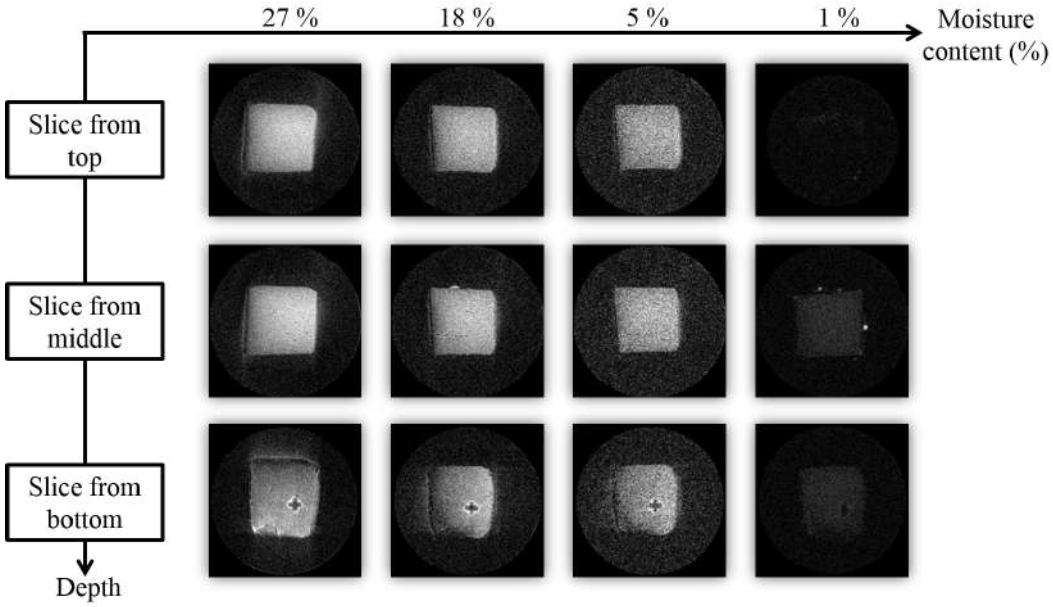

Figure 3.5: Magnetic Resonance Images of an alumina P172SB sample, at different positions for total water contents of 27%, 18%, 5% and 1%.

For further insight, results obtained by MRI were subsequently analyzed using an open-source software ParaView.5.4.1, to calculate averaged pixel concentration profiles,

which should depict the water distribution. A vertical profile is chosen along the central axis of samples for the entire length, with averages made for cross sectional dimensions of 4 mm $\times$ 4 mm (figure 3.6). These profiles of average pixel intensities are shown in figure 3.7 at different times in the drying process. In this set of trials, the drying was accelerated by placing the sample on a hot plate at 50 °C and exposing the remaining 5 faces to the atmosphere.

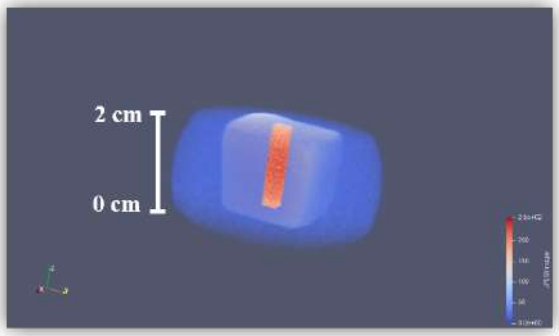

Figure 3.6: Representation of the parallelepiped cut using Paraview software.

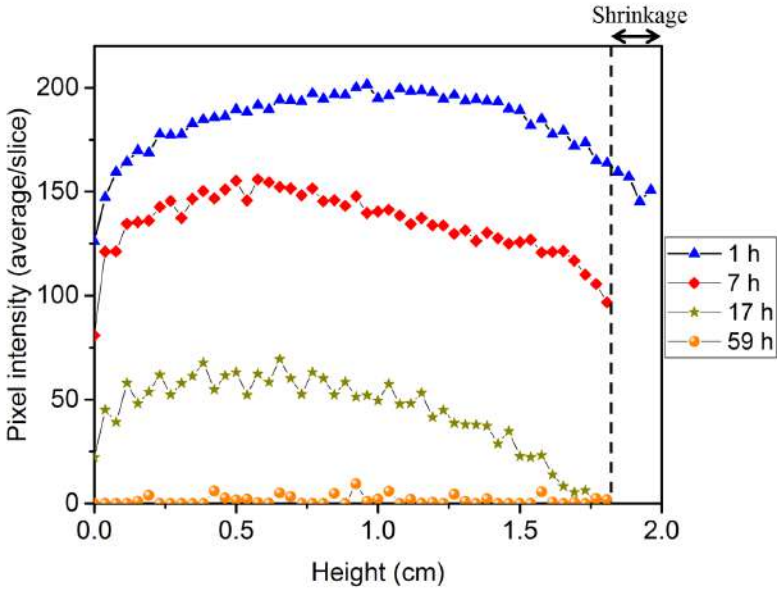

Figure 3.7: Profile curves of the parallelepiped cut as a function of sample height for different drying times. Sample placed on a hot plate at 50 °C and with 5 faces exposed to air.

The first observation is that the overall concentration in water decreases with time as expected. However, the first profile recorded after one hour of drying shows a reduced pixel intensity towards the top and bottom faces of the sample. Even if the drying con-

ditions are different, this result is surprising since the distribution of water should be initially uniform as witnessed by the weight measurements of sub-samples (figure 3.3). Two possible explanations are considered. The forming process by casting could yield a crust towards the exterior of the sample but this does not seem consistent with the weight measurement of sub-samples discussed previously. Secondly, probing of water concentration by NMR measurements is less sensitive towards the outside of the sample chamber. It is indeed known that ZTE-MRI images of objects with constant spin density will often exhibit non-constant signal intensities across the object, with a trend of decreasing signal intensity with increasing distance from the image center. This problem arises from the specific way of data acquisition and reconstruction as described in 2.3. However, since the distribution of water in the sample is assumed to be uniform for the profile obtained after one hour of drying, the subsequent profiles can be recalibrated in relation to it, as shown in figure 3.8. The visualization of the behaviour then seems clear in the profile taken after 7 hours of drying with the appearance of a gradient in water concentration for the top half of the sample (drying front) while the concentration remains uniform in the bottom half. It can be noted in the third profile that the local fluctuations of water content have increased, consistent with complete emptying of some but not all of the pores in a given volume element. Finally a uniform baseline signal of almost zero intensity is obtained for the dry sample (59 hours of drying).

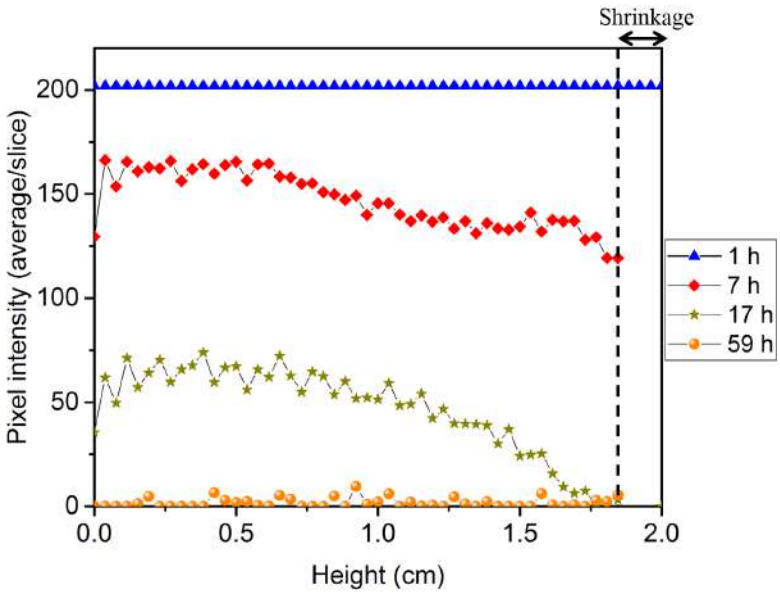

Figure 3.8: Recalibrated profile curves of the parallelepiped cut as a function of sample height for different drying times.

3.2.1.3 ESEM observations

The environmental scanning electron microscope was used to observe the surface of the samples at the micron scale of the grains and pores during drying. Though the experimental conditions inside the microscope chamber in terms of temperature and vapour pressures are some what different to the other two methods as explained in 1.1.3, the basic situation of progressively extracting water out of the ceramic green body is retained. Compared to the starting conditions of 2 °C and 700 Pa, this was achieved by progressively reducing the pressure to 500 Pa. Likewise, a sample dried beforehand in an oven at 110 °C for 24 hours was also observed in the same ESEM.

Observations of the drying process for alumina-P172SB surface are presented in figure 3.9 and figure 3.10. Micrographs of figure 3.9 show the evacuation of water in the same zone of the sample. The different phenomena visible on the surface can be related to the different stages of drying. As one can see, in the first micrograph, water is the dark phase and it forms a continuous film around the grains. This is in agreement with the idea that in the early stages of drying, water evaporates from the surface (liquid-air interface) leading to shrinkage of the ceramic green body. Within the body, initially only solid-liquid interfaces exist. The micrograph b) corresponds to an advancement in the drying process, compared to the first micrograph, where the area occupied by the dark phase is reduced, meaning that the water level has decreased. It can also be noticed that grains are closer to each other which is directly related to shrinkage. In practice, the end of shrinkage is observed during the ESEM experiment when grains stop moving across the field of vision. This occurs between micrographs b) and c) of figure 3.9. After the shrinkage step, water starts first to evaporate from the larger pores and then the smaller pores are emptied later on during the drying process figure 3.9 (c and d). These observations are consistent with literature in the description of relations between the driving forces during drying and the tension in the liquid [11], which is strongly related to pore size. Capillary action ensures that the small pores near to the surface stay filled until all larger pores of the sample are drained. Then in figure 3.10 a) when all of these pores are essentially empty, some remaining moisture can be found located next to grain-grain interfaces.

Comparing the dried sample at 110 °C, presented in micrograph b) of figure 3.10 to the sample dried in the ESEM atmosphere (micrograph a) of figure 3.10), it can be clearly seen that water located at interfaces between grains has been completely removed.

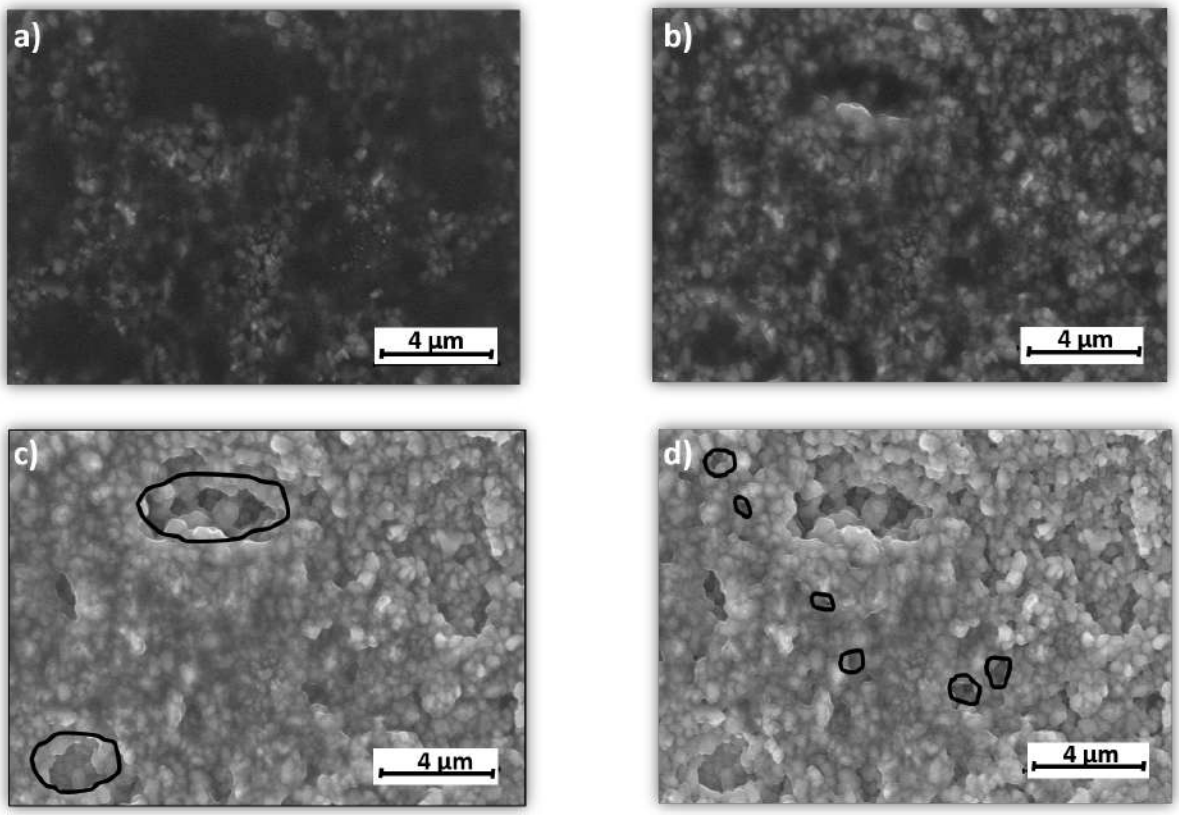

Figure 3.9: ESEM micrographs of a chosen zone on the surface of an alumina-P172SB sample at various stages of drying. Micrographs a) and b) correspond to the CRP of drying with a continuous film of water surrounding grains. c) Corresponds to the falling rate period with water evaporating from the large pores (marked by black lines). d) Represents also the falling rate period, later in drying, with water emptying from the small pores (marked by black lines).

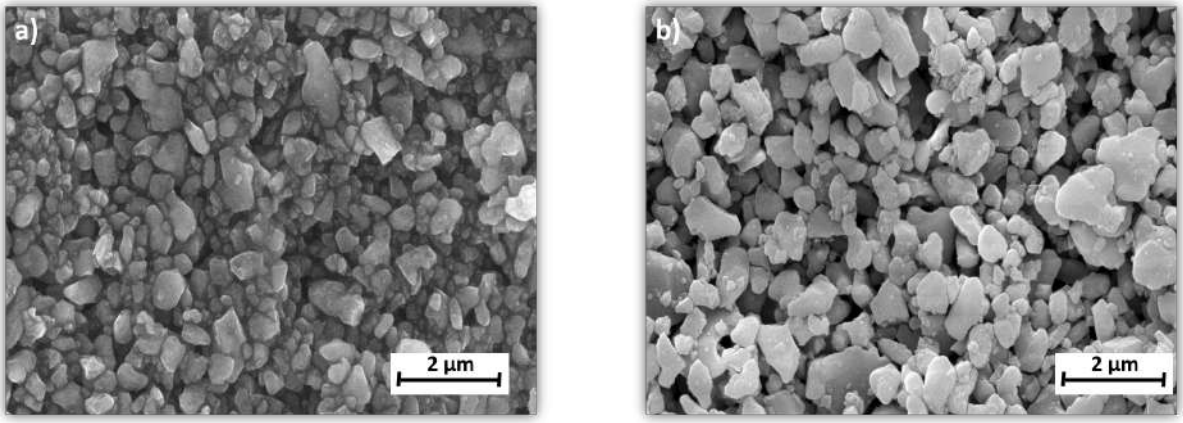

Figure 3.10: ESEM micrographs of alumina-P172SB. a) Sample at the end of drying in ESEM chamber. b) Sample completely dried in an oven at 110 °C for 24 hours.

3.2.2 Kaolin samples

In the previous section, using three different techniques, the investigation of water distribution has been well established for alumina. But the way the water is transported out of the green body may be affected by the material nature and grains morphology because of stronger interactions of water with particles. These factors could influence the distribution of water and its localization within the body as drying proceeds. Therefore, a similar study on kaolin clay with platelet grains was made.

- Weight loss: Drying at 40 °C and 15% RH:

At first, the profiles of water concentration obtained by weight measurements of sub-blocks at 40 °C and 15% are presented in figure 3.11.

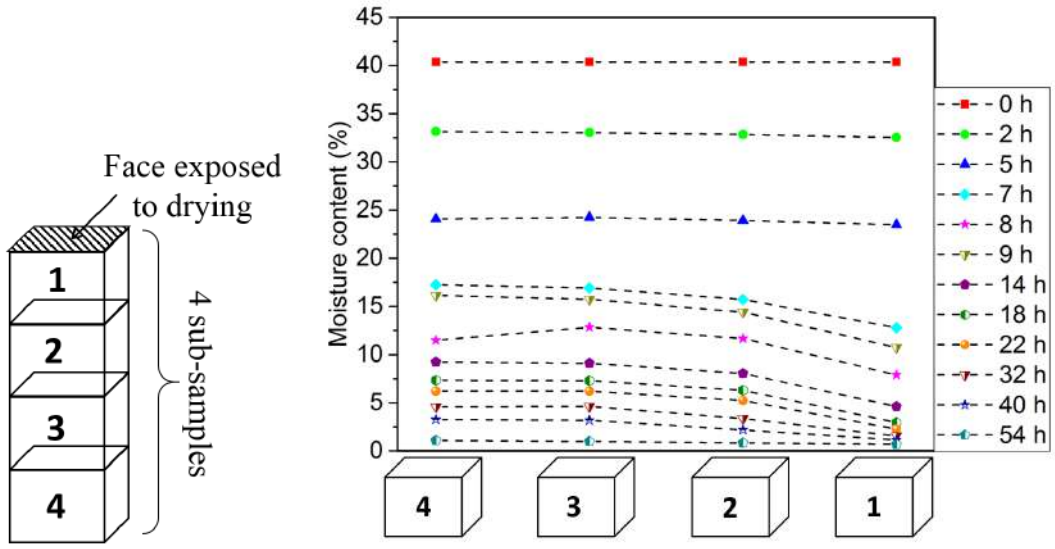

Figure 3.11: Water content of kaolin sub-samples after different drying times, at 40 °C and 15% RH.

Despite the difference of morphology between the two materials, i.e. spherical form of grains for alumina and platelets for kaolin, many aspects of the general behaviour during drying of kaolin samples are similar to alumina. During the initial period of drying accompanied by shrinkage (for water content above 25%), which takes place in the first 5 hours of drying, no gradient in water content within samples is detected as shown in figure 3.11. Later on in the drying process, a gradient in water concentration develops, reaching a maximum value after 8 hours with a difference of 3.7% in the water content between sub-samples 1 and 2. After this duration of drying, since the overall amount of moisture content remaining within the sample does not exceed 10%, the gradient in water concentration decreases which can be explained by an evaporation of water at greater depth and then a transportation of the vapour to the surface by gas diffusion.

- Weight loss and linear shrinkage: Drying at 70 °C and 5% RH:

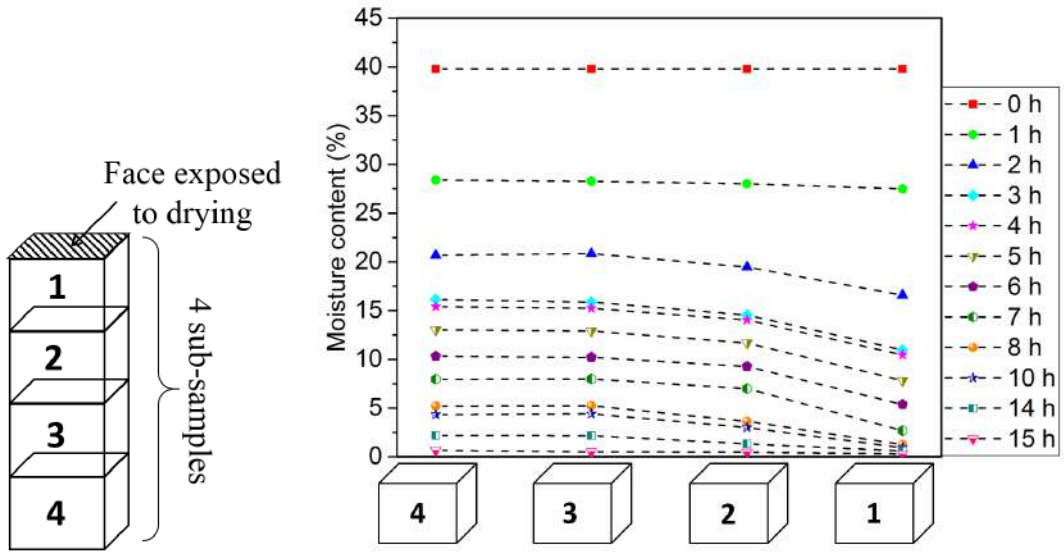

Figure 3.12: Water content of kaolin sub-samples after different drying times, at 70 °C and 5% RH.

For drying experiments carried at 70 °C, again the drying behaviour of kaolin sub-samples presents similarities with the behaviour obtained for alumina as can be observed in figure 3.12. It can be noted that the main effect produced by increasing the drying temperature is the decrease of the drying duration.

- ZTE Magnetic Resonance Imaging:

The MRI observations also reveal the progression of a drying front once the shrinkage stage is completed. A notable difference for the kaolin samples with the MRI technique is that even at the end of drying quite a strong signal remains as shown in figure 3.13. This ^{1}H signal is expected because of the presence of OH groups in kaolinite which give rise to a residual signal [52]. Furthermore, the presence of this strong baseline (> 50) is clearly seen in the graphs of the averaged pixel concentration and recalibrated profiles in figures 3.14 and 3.15, respectively.

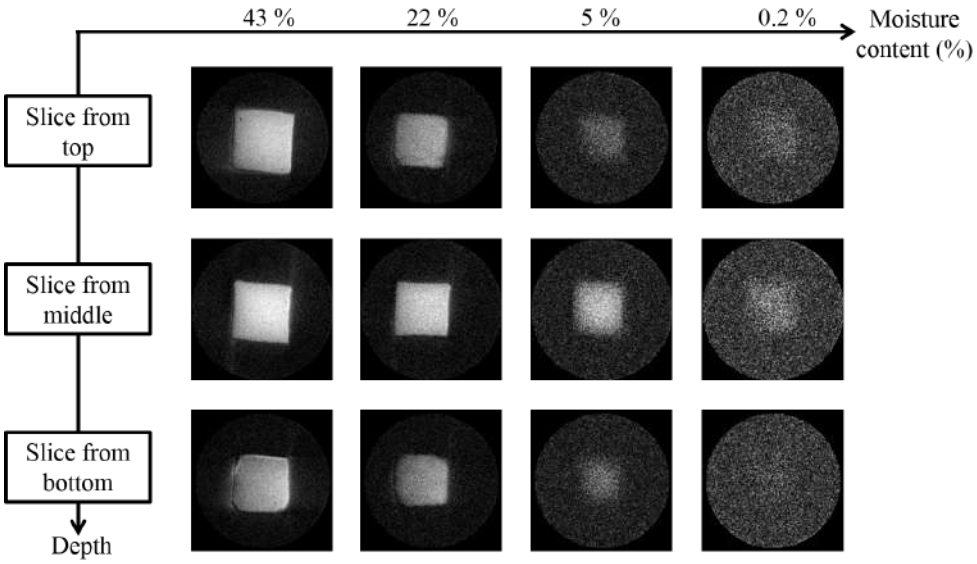

Figure 3.13: Magnetic Resonance Images of an alumina P172SB sample, at different positions for total water contents of 43%, 22%, 5% and 0.2%.

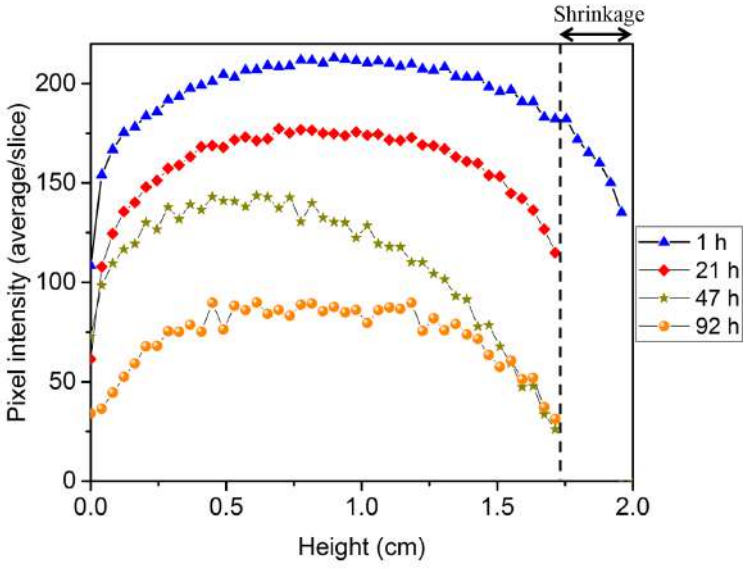

Figure 3.14: Profile curves of the parallelepiped cut as a function of sample height for different drying times. Sample placed on a hot plate at 50 °C and with 5 faces exposed to air.

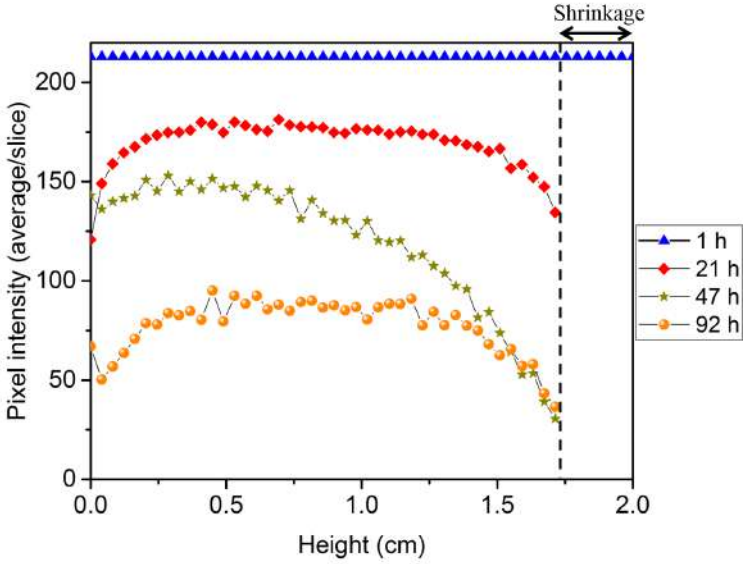

Figure 3.15: Recalibrated profile curves of the parallelepiped cut as a function of sample height for different drying times.

- ESEM observations:

Observations of a kaolin sample during drying using the ESEM are presented in figure 3.16. As for alumina samples, during the first stage of drying (first and second micrographs), the grains are surrounded by water. Only liquid/solid and liquid/gas interfaces exist. Then during the falling rate period, water starts to evaporate from the larger pores before the smaller ones, similar to the observations for alumina.

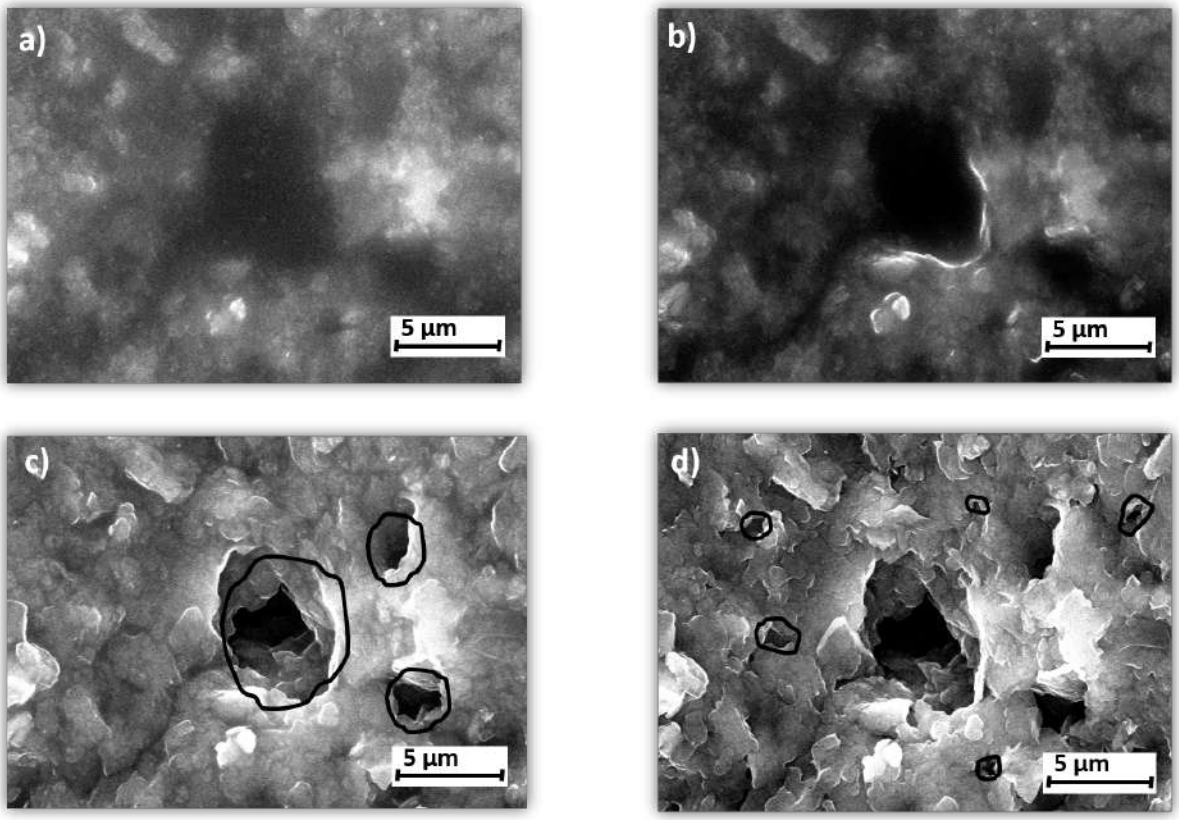

Figure 3.16: ESEM micrographs of a chosen zone on the surface of a kaolin sample at various stages of drying. Micrographs a) and b) correspond to the CRP of drying with a continuous film of water surrounding grains. c) Corresponds to the falling rate period with water evaporating from the large pores. d) Further drying reveals emptying of water from the small pores.

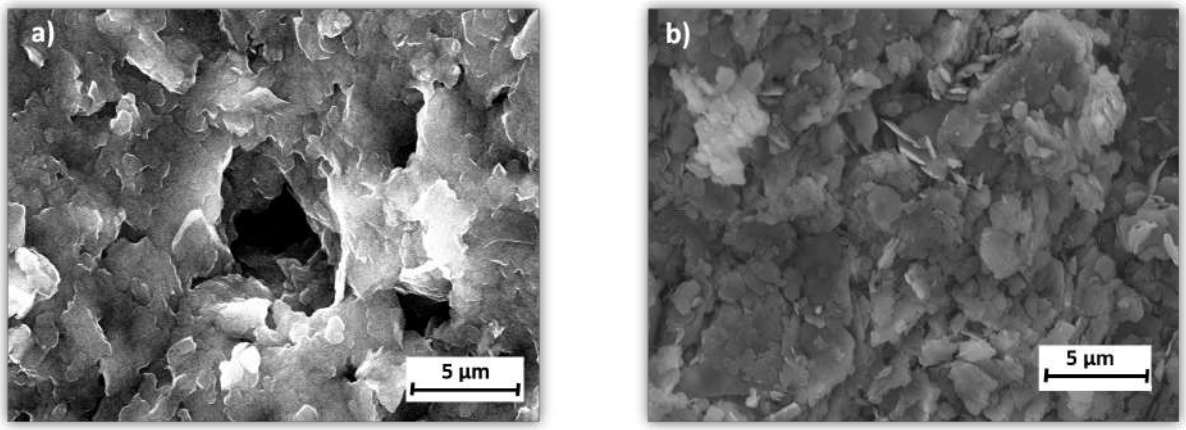

Figure 3.17: ESEM micrographs of alumina-P172SB. a) Sample at the end of drying in ESEM chamber. b) Sample completely dried in an oven at 110 °C for 24 hours.

3.3 Conclusion

In this chapter, the spatial distributions of water within alumina and kaolin green bodies have been investigated at different scales during drying. Three distinct techniques were used. At the macroscopic scale, the evolution of water content was estimated by a simple weighing of blocks with 1 cm of height which had been cut from samples with a total height of 4 cm. As a complement, on a smaller scale, Magnetic Resonance Imaging (MRI) measurements were conducted with a spatial resolution of 0.4 mm. Thirdly, observations have been made of a surface exposed to drying in an Environmental Scanning Electron Microscope (ESEM).

This work brings new information but basically confirms the general picture of drying established in the literature. For "slow" drying corresponding to removal of water by natural convection, during the first stage involving shrinkage, the distribution of water in the ceramic body is uniform. Then during the second stage of drying, when the body volume is fixed and water evaporates from the pores in the interior of the body, the distribution of water within the sample varies with position. A gradient in water concentration is revealed between emptied zones next to the drying face(s) and the body interior where water is removed more slowly. At the grain scale, it was noticed that the water starts to evaporate from the larger pores first, then the smaller pores later during the drying process. Then in the final stage of drying, the residual water is localized in the zones next to the solid–solid contacts between particles. This information will be useful in the next part of this study in order to help to explain how physical properties vary with moisture content, particularly the effective thermal conductivity and water diffusion coefficient.

Chapter 4 :

Physical properties involved in heat and mass transfers

Chapter context

Since the final objective of this work is the construction of a robust numerical model which describes the drying behaviour of a ceramic green body, there is the need to have reliable values of the physical properties. That is why this chapter is devoted to the experimental evaluation of physical properties involved during drying. First, the evolution of water activity for alumina and kaolin materials during drying is presented. Then, values for the effective diffusion coefficient are calculated using the experimental results for water distribution obtained by weighing which have been presented in the previous chapter. Finally, variations in the heat capacity and thermal conductivity of the green body are assessed for both materials during drying. Some of the results presented in this chapter on the assessment of the thermal conductivity have been published in the paper: " Thermal conductivity of ceramic green bodies during drying" by B, Nait-Ali et al. *Journal of the European Ceramic Society 37 (2017) 1839–1846.*

4.1 Mass transport

4.1.1 Water activity

4.1.1.1 Experimental set-up

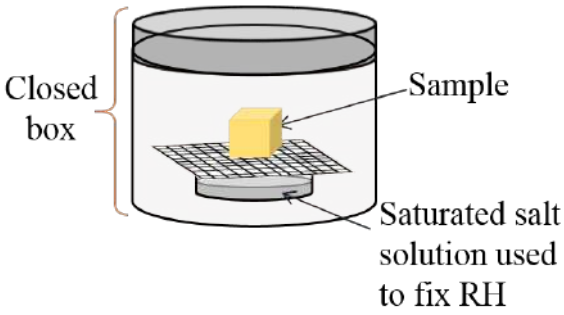

Figure 4.1: A schematic representation of the water activity measurement.

In a controlled environment with constant temperature and relative humidity, a wet green body loses water until an equilibrium state is achieved with a constant mass. At this stage, the water vapour at the sample surface is the same as that of the exterior atmosphere and the temperature at the body surface is equal to the air temperature. There are no heat and mass transfers. Considering equations 1.9 and 1.11, $C_{air} = C_{s-b.l}$ and $T_{air} = T_s$. As a consequence, the water activity a_w is equal to the relative humidity fixed in the chamber. The relationship between the equilibrium moisture content (X) and water activity (a_w) of a body is known as the water sorption isotherm [53, 54]. Moisture sorption isotherms can be obtained for adsorption or for desorption processes. In our case, since we deal with drying, only desorption was examined for alumina and kaolin

pastes. Saturated salt solutions were used to fix the relative humidity according to [55]. Different salts were chosen as shown in table 4.1. The samples were placed in closed boxes containing the saturated solutions, as illustrated in figure 4.1, until the mass has reached a constant value (ca. one month). Afterwards, the sample was completely dried in an oven for 24 hours at 110 °C. The moisture content (X) of each sample was calculated on a dry basis using the relation 1.1 of chapter 1.

	Lithium chloride (LiCl)	**Potassium carbonate (K_2CO_3)**	**Sodium chloride (NaCl)**	**Potassium chloride (KCl)**	**Potassium sulfate (K_2SO_4)**
RH at (20 °C)	12 %	43.2 %	75.5 %	85.1 %	97.6 %
RH at (40 °C)	11.2 %	43.2 %	74.7 %	82.3 %	96.4 %

Table 4.1: Saturated salt solutions used with the corresponding relative humidities at 20 °C and 40 °C [55].

4.1.1.2 Results

Using the experimental set-up, moisture desorption of kaolin and alumina materials was evaluated at ambient temperature (ca. 20 °C) and 40 °C. The results obtained for the different relative humidities are plotted in figures 4.2 and 4.3.

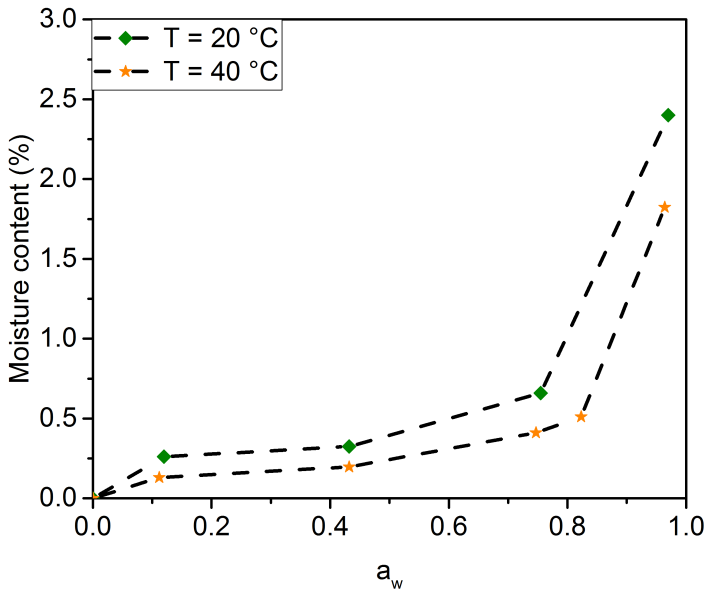

Figure 4.2: Desorption isotherms equivalent to moisture content as a function of water activity for alumina samples measured at 20 °C and 40 °C.

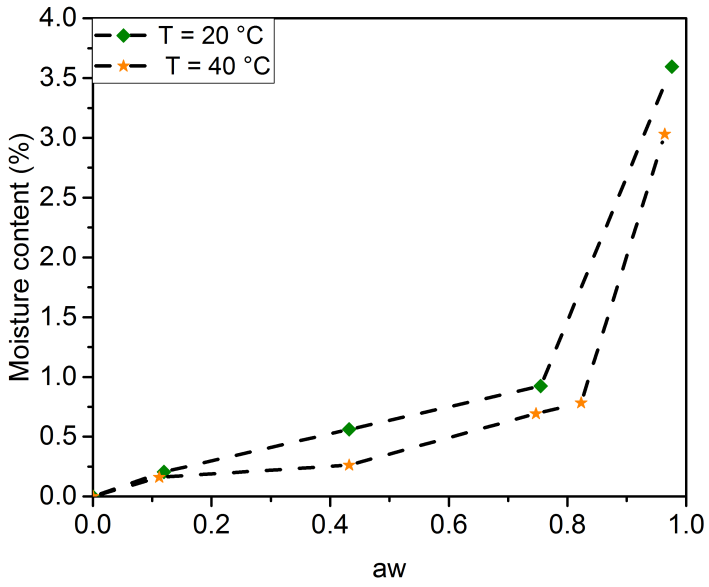

Figure 4.3: Desorption isotherms equivalent to moisture content as a function of water activity for kaolin samples measured at 20 °C and 40 °C.

As can be observed, we deduce that during drying the water activity is close to 1 until the moisture amount at the sample surface falls to less than 3% for alumina and 4% for kaolin. Then the activity strongly decreases down to 0.11 for 0.13% of moisture content within alumina and 0.16% in kaolin samples. Furthermore, in terms of temperature, it should be noted that a small difference between values at 20 °C and 40 °C is observed. This difference is explained in the literature by the higher energy provided at 40 °C to desorb water molecules [53, 56].

4.1.2 Estimation of the diffusion coefficient

As discussed in the first chapter in section 1.2.4.2, some of the studies on the dependence of the diffusion coefficient with moisture content have been based on weight measurments [15, 16]. Similarly in this section, order of magnitude estimates of the diffusivity values for water transport in the drying body are made using the results obtained by weighing (Chapter 3 section 3.1.4.1).

As a useful simplification, the situation of one dimensional transport after the shrinkage stage is considered. From a mass balance made at the sample face exposed to air at $x = 0$, the outgoing water flux $J_{x=0}[mol\ m^{-2}\ s^{-1}]$ can be written as [12, 57]:

$$J_{x=0} = -D_w \frac{\partial C}{\partial x} \tag{4.1}$$

where D_w is the diffusion coefficient in $m^2\ s^{-1}$, C is the water concentration in $mol\ m^{-3}$ in the volume element next to the interface and x is the position coordinate in m. This is similar to an expression for Fick's law within the body. An approximate value for the upper limit of the diffusion coefficient D_w can then be given by the relation.

$$D_w = \frac{J_{x=0}}{\frac{\Delta C}{\Delta x}} \tag{4.2}$$

where $\frac{\Delta C}{\Delta x}$ refers to the difference in water concentration of the first two sub-samples per unit length next to the drying face in figure 3.1 and the sign has been dropped. In reality the local concentration gradient may be steeper next to the interface. The diffusion flux corresponds to the amount of evaporated water per unit area of exposed drying surface during a given time period described by the relation :

$$J_{x=0} = \frac{1}{S}\frac{\Delta C}{\Delta t} \tag{4.3}$$

where ΔC refers to the change in average concentration of the complete sample over time Δt and S is the area of the exposed face.

In the case of the alumina-P172SB samples, shrinkage is essentially finished after 3 hours of drying. Using equations 4.2 and 4.3, diffusion coefficient values were calculated from 3 hours to 21 hours of drying, since a concentration gradient in the first two sub-samples is revealed during this stage, as can be observed in table 4.2. The evaporation rate from the drying surface was evaluated over a time difference of 2 hours by interpolation of the average mass values for the complete sample.

Time (hours)	$J_{x=0}(mol\ m^{-2}\ s^{-1})$	$\frac{\Delta C}{\Delta x}(mol\ m^{-4})$	$D_w(m^2\ s^{-1})$
3	4.9×10^{-2}	2.1×10^{4}	2.3×10^{-6}
4	4.8×10^{-2}	1.3×10^{5}	3.8×10^{-7}
5	$^{*}3.6 \times 10^{-2}$	2.7×10^{5}	5.7×10^{-8}
7	$^{*}2.5 \times 10^{-2}$	3.6×10^{5}	3.5×10^{-8}
10	1.1×10^{-2}	3.6×10^{5}	3.1×10^{-8}
14	4.9×10^{-3}	3.1×10^{5}	1.6×10^{-8}
21	3.7×10^{-3}	2.6×10^{5}	1.4×10^{-8}

Table 4.2: Estimation of the diffusion coefficient values of water through an alumina P172SB sample at different times during drying. (* indicates interpolated values).

First, it can be noted that the values of the diffusion coefficient of water lie between a value of $2.3 \times 10^{-6}\ m^2\ s^{-1}$ just after the end of shrinkage and a value of $1.4 \times\ 10^{-8}\ m^2\ s^{-1}$

after 21 hours of drying when 5% of water still remains within the sample. These estimations are in rough agreement with values found in literature. As an example, for water evaporation from a porous alumina pellet the diffusion coefficient of water within the pellet was deduced to be $5 \times 10^{-8}\ m^2\ s^{-1}$ from the concentration profile evaluated by MRI measurements [34]. Second, the initial large value of the diffusion coefficient should come as no surprise given that, at high water amounts within the material, capillary forces are the main mechanism transporting water. The progressive decrease in diffusion coefficient value, with drying time and water amount, is then consistent with a change in the dominant transport mechanism towards diffusion of water vapour through the pores to the outside surface.

A simple attempt was made to test this explanation by altering the microstructure of the drying ceramic and hence modify the two transport mechanisms. Two alumina powders were compared: P172SB with small grains(0.4 μm) and P152SB with larger grains (1.3 μm). Presumably the presence of smaller pores and particles is promoted in P172SB compared to P152SB. First of all the total mass losses of the alumina samples were followed in the same conditions of drying, i.e. at the same humidity and at similar temperatures. The drying rates were then calculated from water loss over time per unit of area exposed to drying and are plotted as a function of moisture content in figure 4.4.

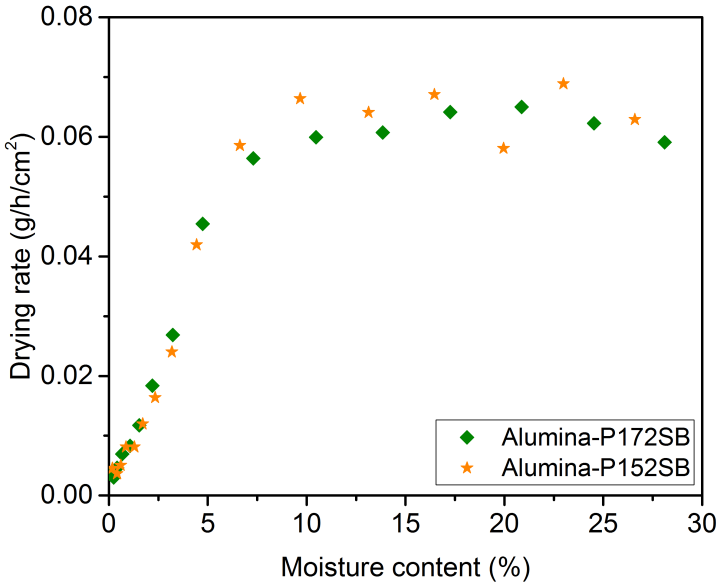

Figure 4.4: Rate of drying as a function of the moisture content for two alumina powders at 40 °C and 30% of relative humidity.

Despite the increase in particle size between the alumina powders (P152SB three times larger than P172SB), no significant difference in drying behaviour is revealed,

especially after the constant rate period is completed (moisture content less than 8%).

Furthermore, the estimation of diffusion coefficients for P152SB, via the weighing of sub-samples yields again a strong dependence on moisture content as shown in figure 4.5. The two data sets can not be distinguished within uncertainty, suggesting reproducibility and that the two pore size distributions are not sufficiently different. More refined evaluation might yield differences at the lowest moisture contents, corresponding to the emptying of the smallest pores.

Even if no particular effect due to grain size difference in the alumina powders was detected, these simple estimations of diffusion coefficient represent an interesting start in the comprehension of the role of this parameter in drying of ceramic bodies. It should be possible to obtain more refined values of the diffusion coefficient by constructing a numerical model for the drying of a green ceramic body, which predicts internal concentration profiles to compare to experimental data.

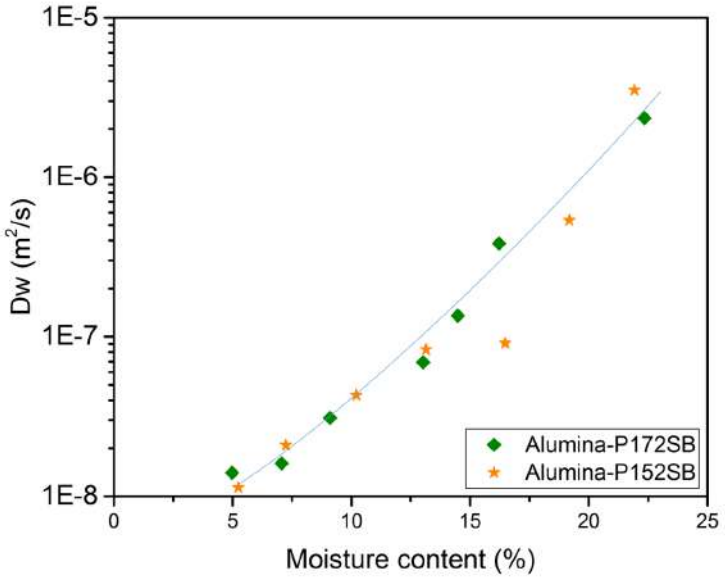

Figure 4.5: Estimated diffusion coefficient as a function of the moisture content for two alumina powders P172SB and P152SB.

As already mentioned, drying is a coupling of two transfers: mass and heat transfers. Therefore, after determining the mass transport properties involved during drying, the next step is to investigate the thermal ones as well.

4.2 Thermal properties

4.2.1 Heat capacity

Unlike transport properties (diffusion coefficient of water and the thermal conductivity), heat capacity is independent of the microstructure involving particles and pore distribution/sizes. Variation in this property is controlled by the mass fraction of the solid and water as drying proceeds. Therefore, in the case of alumina and kaolin samples, the overall heat capacity can be calculated using the relation 1.15 in association with heat capacity values available for each phase in the literature. The value for alumina is $Cp_{alumina} = 780\ J\ kg^{-1}K^{-1}$, for kaolin containing hydroxyl groups, as in our case, the value is $Cp_{kaolin} = 949\ J\ kg^{-1}K^{-1}$ [58, 59]. The value for water at 20 °C is $Cp_{water} = 4210\ J\ kg^{-1}K^{-1}$ which is more than 4-5 times the values for alumina and kaolin [58]. Figure 4.6 shows increases for the wet samples compared to the dry green bodies which can be explained by the high heat capacity value of water. Moisture contents up to 30% for alumina and 40% for kaolin yield a strong increase in heat capacity by a factor of 2 (1600 $J\ kg^{-1}K^{-1}$ and 1930 $J\ kg^{-1}K^{-1}$, respectiviely).

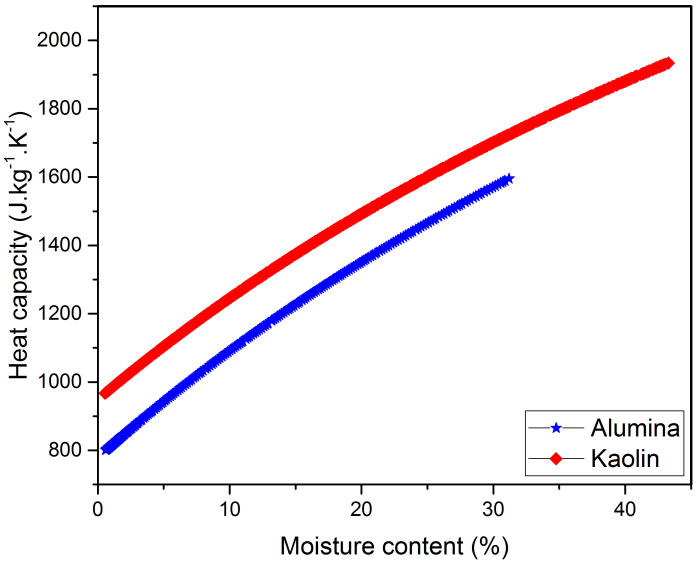

Figure 4.6: Calculated values for heat capacity as a function of moisture content for alumina and kaolin materials. $Cp_{alumina} = 780\ J\ kg^{-1}K^{-1}$, $Cp_{kaolin} = 949\ J\ kg^{-1}K^{-1}$ and $Cp_{water} = 4210\ J\ kg^{-1}K^{-1}$.

note: this value will be reduced on firing to approximately 780 $J\ kg^{-1}K^{-1}$ with the removal of hydroxyl groups.

4.2.2 Thermal conductivity

4.2.2.1 Thermal conductivity measurement

Transient plane source method: The thermal conductivity of the samples was measured using the transient plane source (TPS) method, operating at room temperature. This technique, developed by Gustafsson, uses a thin probe constituted of a nickel spiral wire in a disk shaped sandwiched between two films of an insulating material (figure 4.7.a) [60]. The probe is placed between two blocks made of the material to be measured as shown in figure 4.7.b. The nickel wire is used, first, as a heat source using Joule's effect and, second, as a sensor to monitor the temperature increase by measuring the electrical resistance of the wire. The two sample blocks enclosing the probe are considered to be an infinite medium during the experiment as well as homogeneous and isotropic. At $t < 0$, the material should be in thermal equilibrium with the environment at the temperature T_0 (uniform in the solid). The measurement consists of recording the increase in temperature after applying a constant heat flux from time $t = 0$. The thermal conductivity is determined from the time dependent temperature response. The probing depth of heat penetration is typically of the same order of magnitude as the probe diameter, which was 6.3 mm in our case. Typical measuring time was 80 s.

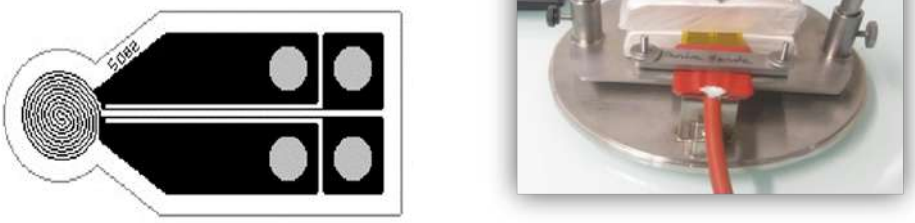

(a) (b)

Figure 4.7: (a) Schematic representation of a hot disk probe (b) Thermal conductivity measurement.

Measurements as a function of water content: as already stated above, before each thermal conductivity measurement the temperature should be in thermal equilibrium and the samples have to be homogeneous and isotropic. However, during drying the temperature in the sample varies strongly, depending on the water evaporation rate. Furthermore due to coupled heat and mass transfers, the temperature and water distribution are not spatially uniform in the material. Thus to ensure a constant and uniform temperature and water distribution in the sample before each measurement,

samples were first dried at ambient temperature and relative humidity (ca. 20 °C and 40%) for a given time, then weighed and covered by a polyvinyl film to stop the drying process, for a duration of 4h.

The choice of this duration was decided after two additional tests which enabled us to check the uniformity and stability of the temperature as well as water distribution before measurements. Samples for both tests were carried out in the same way as samples prepared for the thermal conductivity measurement.

- Temperature test

At first, we placed three thermocouples in different positions within the covered sample as can be seen in figure 4.8.a. Temperatures were recorded every 15 minutes after stopping drying. Figure 4.8.b shows similar increases in temperature for the three thermocouples to reach room temperature after 3 hours. Therefore, a delay of 4 hours is sufficient to reach a constant and uniform temperature in the sample.

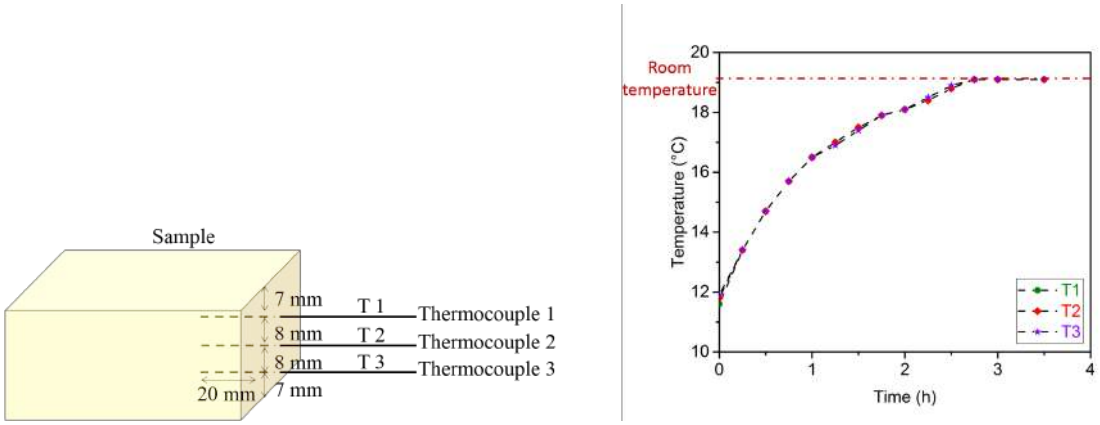

(a) (b)

Figure 4.8: (a) Temperature monitoring at three sample positions (b) Temperature as a function of time for the three sample positions after stopping drying.

- Water distribution test

The second test consists of cutting, from the appropriate sample, smaller specimens in order to check at different moments in the progression of drying (before and after the shrinkage stage) that water content is uniform after the delay of 4 hours (figure 4.9). For that, drying was stopped for 4h. Then the weights of the different specimens were measured before and after they were completely dried in the oven at 110 °C. The calculated moisture contents for each block were close to each other with a difference of ± 0.5%. It confirms that 4 hours is a sufficient duration to attain a uniform water distribution.

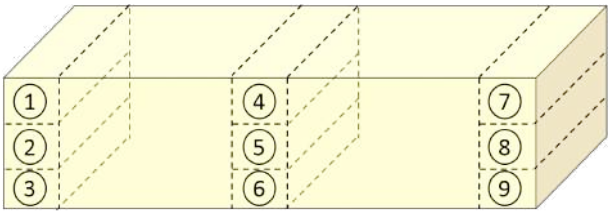

Figure 4.9: Representation of the sample divided into small blocks.

Finally, to measure the completely dry green body, some samples were dried at 40 °C until the mass had reached a constant value. The thermal conductivity was then measured after cooling down to room temperature. Samples were dried at 40 °C instead of 110 °C to avoid cracks.

4.2.2.2 Evolution of thermal conductivity during drying of alumina green bodies

In order to follow and analyze the thermal conductivity of an alumina green body during the different stages of drying, thermal conductivity and linear shrinkage are plotted as a function of moisture content in figure 4.10. Thermal conductivity variations reveal 3 distinct regimes. At the beginning of drying, the value increases from 2.5 $W\ m^{-1}\ K^{-1}$ to reach a maximum value of 3.1 $W\ m^{-1}\ K^{-1}$. Then the thermal conductivity decreases, weakly at first down to 1.5 $W\ m^{-1}\ K^{-1}$ and strongly at the end of drying to yield a value of 0.25 $W\ m^{-1}\ K^{-1}$. These changes in the effective thermal conductivity as a function of the drying progression, corresponding to a factor of 12 between the maximum value and the endpoint, were examined in comparison to the linear shrinkage data. The thermal conductivity increases when the shrinkage occurs and the maximum conductivity value matches the end of strong linear shrinkage which then remains almost constant with further weight loss.

Note: it is worth mentioning here that the end of shrinkage for the alumina sample in this study corresponds to 19% of moisture content which is lower compared to the previous studies. This may be explained by the use of a different P172SB alumina batch for these experiments. Shrinkage experiments were repeated for this batch with different sample sizes and all give an end of shrinkage for approximately 20%.

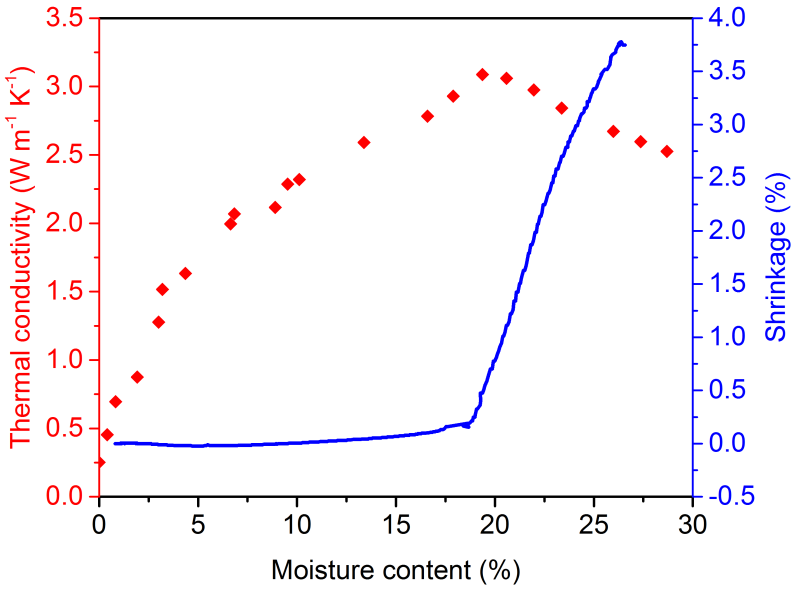

Figure 4.10: Thermal conductivity and linear shrinkage as a function of moisture content for alumina samples.

Focusing on the first thermal conductivity variation (the increase), and relating it to the first stage of drying with strong shrinkage, down to ca. 19% of moisture content, the material is assumed to be constituted of uniquely the solid and water, meaning that the decrease in the apparent volume corresponds to the volume of water which has been evaporated [8]. As a consequence, the volume fraction of solid, which has a higher conductivity than water, increases. Furthermore solid particles, which at the beginning of drying are separated by stable films of water, evolve towards a closer packing increasing the overall grain-grain contact area. These two aspects, schematically illustrated in figure 4.11, are responsible for the thermal conductivity increase when the shrinkage occurs. More insight into the role of each of these contributions is given by a simple model where the effective thermal conductivity can be calculated using the Maxwell-Eucken relation for a mixture of solid and water [61]. For this, the material is assumed to be constituted of isolated solid inclusions surrounded by water described by the following equation:

$$\lambda_{eff} = \lambda_{water} \frac{\lambda_{solid} + 2\lambda_{water} + 2v_{solid}(\lambda_{solid} - \lambda_{water})}{\lambda_{solid} + 2\lambda_{water} - v_{solid}(\lambda_{solid} - \lambda_{water})} \tag{4.4}$$

where λ_{water} is the thermal conductivity of water, λ_{solid} is thermal conductivity of the solid, v_{solid} is the volume fraction of solid. Equation 4.4 is also equivalent to the Hashin-Shtrikman lower bound for an isotropic mixture of alumina particles and water [62]. Values calculated, with a solid phase thermal conductivity of 35 $W\ m^{-1}\ K^{-1}$ and a value of 0.61 $W\ m^{-1}\ K^{-1}$ for water [63, 64], are 2.08 $W\ m^{-1}\ K^{-1}$ at the beginning of drying

and 2.39 $W\ m^{-1}\ K^{-1}$ at the end of the shrinkage stage (figure 4.12). The analytical model assumes that there is no contact for the heat flow between particles, which is probably not strictly the case in the real material and can explain the slightly greater experimental values compared to the predictions. Based on the water and solid volume fraction changes, the calculated difference of 0.3 $W\ m^{-1}\ K^{-1}$ is less than the measured difference of 0.6 $W\ m^{-1}\ K^{-1}$ between the initial wet state and the end of shrinkage. This suggests that an additional factor, change in the particle-particle contact area, influences the thermal conductivity values during the first stage of drying.

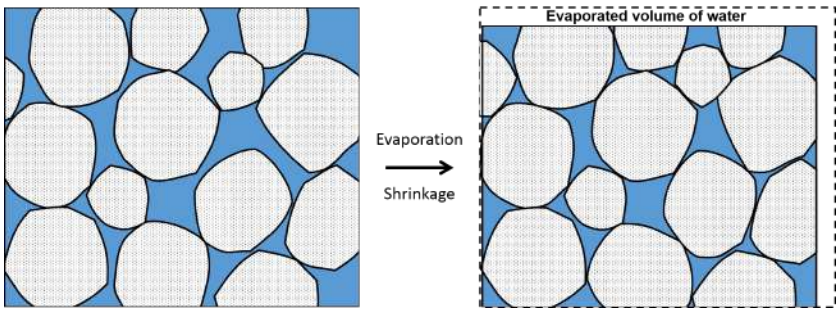

Figure 4.11: Schematic arrangement of solid grains and water at: (a) the start of drying and (b) the end of the shrinkage. The volume fraction of solid has increased as well as the overall contact area between grains.

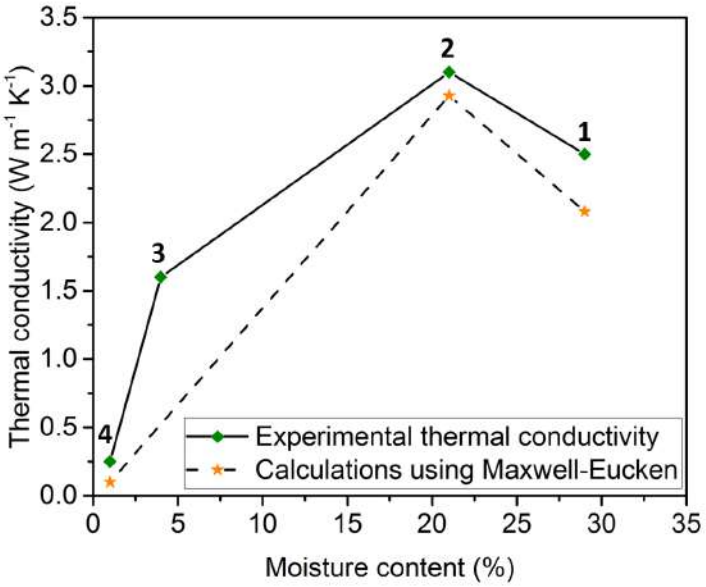

Figure 4.12: Schematic of thermal conductivity as a function of weight loss indicating 4 characteristic points (1, 2, 3, 4) in the drying behaviour. Calculated values using the Maxwell-Eucken relation with water (1, 2) or air (4) as the continuous phase.

Now by looking into the second period once the major shrinkage is achieved, at ca. 19% of moisture content,further drying gives a decrease in thermal conductivity. The effect has already been described in literature and is explained by the volume of water which is replaced by air with a lower thermal conductivity: 0.026 $W\ m^{-1}\ K^{-1}$ or even less for small pores ($< 0.5\ \mu m$) if the Knudsen effect is operating [65, 66]. However, the final stronger decrease in the thermal conductivity seems to indicate that other mechanisms can be involved at the end of the drying process. After a complete drying at 40 $°C$, the material is constituted of only the solid and air. Using the Maxwell-Eucken model, i.e. assuming that the material is constituted of isolated solid inclusions surrounded by air, the predicted value from equation 4.4 on replacing water with air, is 0.1 $W\ m^{-1}\ K^{-1}$, which is below the measured thermal conductivity (figure 4.12). Again the difference between experimental and calculated values can be attributed to the contacts between particles which are not taken into account in the model.

To investigate further the roles of particle-particle contacts and water distribution, we have made a series of calculations at points 2, 3, and 4 of figure 4.12 illustrating the importance of information on the distribution of water in the solid-pore system during drying and in particular in relation to the grain-grain contacts. Below 19% of moisture content, the material exhibits an almost constant volume with a stable continuous phase of joined particles, termed here as the solid matrix. This solid matrix is associated with a second continuous phase occupying the intervening space (or "open porosity") which can be water, air or a mixture of both of them. The effective thermal conductivity (λ_{eff}) of this type of system can be estimated using effective medium percolation theory in the form of Landauer's relation since the 2 phases are continuous with volumes close to 50% [67, 68]. To calculate values corresponding to an equivalent solid matrix, Landauer's relation can be solved to give:

$$\lambda_{solid\ matrix} = \frac{2{\lambda_{eff}}^2 - \lambda_{eff}\lambda_{second\ phase}(2 - 3v_{solid})}{\lambda_{second\ phase} + \lambda_{eff}(3v_{solid} - 1)} \tag{4.5}$$

where $\lambda_{second\ phase}$ is the second phase thermal conductivity value, and v_{solid} is the volume fraction of the solid. We have assumed that:

1. at point 2, the material is only constituted by solid and water,
2. at point 4, after a complete drying at 40$°C$, the material is only constituted of the solid and air,
3. at point 3 when the slope in the thermal conductivity decrease changes, the material is constituted of the solid, water and air. A value for $\lambda_{second\ phase}$ was calculated by assuming that layers of water line the pore contours on the solid

surface. Due to this specific distribution of the water inside the pores, with paths to vehicle heat across the pore, the Maxwell-Eucken model was chosen to estimate the thermal conductivity of the second phase.

$$\lambda_{second\ phase} = \lambda_{water} \frac{\lambda_{air} + 2\lambda_{water} + 2v'_{air}(\lambda_{air} - \lambda_{water})}{\lambda_{air} + 2\lambda_{water} - v'_{air}(\lambda_{air} - \lambda_{water})} \tag{4.6}$$

where λ_{water} and λ_{air} are the thermal conductivities of water and air, v'_{air} is the volume fraction of air or also known by the degree of saturation in the second phase, i.e. in the pores. This corresponds to a situation described successively in previous studies on porous zirconia ceramics in humid atmospheres [20, 69].

The calculated values of $\lambda_{solid\ matrix}$ are given in table 4.3 and are significantly less than 35 $W\ m^{-1}\ K^{-1}$, which is the characteristic value of the intrinsic thermal conductivity of alumina.

A first aspect of explanation can be attributed to the presence of interfaces in the equivalent solid matrix since the alumina phase is polycrystalline and originates from a compacted powder. From a pragmatic engineering point of view with respect to heat flow,we can treat the "solid matrix" as resistors in series, representing the particles (intrinsic thermal conductivity) and the thermal resistance at the interface regions. This can be written as:

$$\frac{1}{\lambda_{solid\ matrix}} = \frac{1}{\lambda_{grain}} + nR_{contact} \tag{4.7}$$

where $\lambda_{solid\ matrix}$ represents the thermal conductivity of the equivalent solid matrix (matrix = grains + interfaces), λ_{grain} is the thermal conductivity of a grain and $R_{contact}$ is identified as a thermal resistance representing an interface plane with macroscopic dimensions (i.e. sample dimensions in the case of 100% dense material).

In the case of a "green body", the effective thermal conductivity is not only modulated by the pore volume fraction in the range 40–50%, but also by reduced contact area between grains. In the present work, even if somewhat arbitrary, the effect of reduced contact area has been incorporated into the conductivity of the solid matrix. Compared to the dense sintered body with a grain boundary network extending across the entire sample, the value of $R_{contact}$ for the green body is significantly amplified by the small solid-solid contact area between particles. The interface plane, described by $R_{contact}$ considered at the macroscopic scale of the sample cross section, represents both zones of solid-solid contact and narrow gaps of empty space. In fact the attribution of a negligibly small volume of pore fraction

in the term $R_{contact}$ has very strong effect. A representation of these different situations is given in figure 4.13. It should be noted that the schematic in figure 4.13.b remains very idealized since the grain-grain contacts in a real ceramic green body will actually be at multiple levels. A value for n is obtained from the inverse median grain size of the powder (0.4 μm).

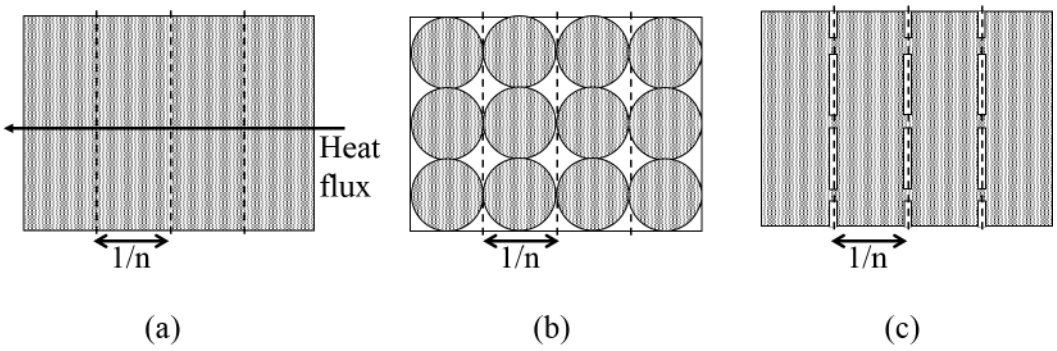

Figure 4.13: (a) Dense sintered body approximated by flat slabs separated by interface planes. (b) Green body represented as an idealised cubic arrangement of pores and particles with small solid-solid contact area. (c) Equivalent solid matrix for the green body where interface planes exhibit both solid-solid contacts and narrow gaps of empty space.

Hence from equations 4.5 and 4.7 the thermal contact resistance ($R_{contact}$) has been estimated at 3 characteristic points in the drying behaviour shown in figure 4.12. These values are also given in table 4.3 which can now be reviewed.

	Point 1	**Point 2**	**Point 3**	**Point 4**
Volume fraction of solid	0.47	0.52	0.52	0.52
Volume fraction of water	0.53	0.48	0.07	0
Volume fraction of air	0	0	0.41	0.48
Experimental effective conductivity ($W\ m^{-1}\ K^{-1}$)	2.5	3.1	1.6	0.25
Calculated solid matrix thermal conductivity ($W\ m^{-1}\ K^{-1}$)		7.8	5.1	0.7
Thermal contact resistance ($m^2\ K\ W^{-1}$)		4×10^{-8}	6.6×10^{-8}	5.3×10^{-7}

Table 4.3: Data for analytical calculations, calculated values for equivalent solid matrix thermal conductivity and thermal resistance of planes representing the grain-grain contacts.

The calculated values of solid matrix thermal conductivity on applying volume fraction changes of air and water to equations 4.5 and 4.6, decrease between points 2 and 4 from 7.8 $W\ m^{-1}\ K^{-1}$ to 0.7 $W\ m^{-1}\ K^{-1}$. This suggests that the description of the behaviour with fixed values of intrinsic thermal conductivity and thermal contact resistance is not

sufficient. It is necessary to vary the value of $R_{contact}$ with water content to find agreement between prediction and experiment. In particular, between point 3 and point 4, the strong decrease in the value of solid matrix thermal conductivity could be explained by the location of water in the system. Just before the end of the drying process, residual water is located in the neck regions between grains as revealed in the ESEM observations (figure 3.10). The action of water like a "thermal grease" in a mechanical contact is illustrated in figure 4.14.a. The removal of water (with a higher thermal conductivity than air) in the neck region leads to the situation shown in figure 4.14.b, explaining the strong increase in $R_{contact}$, by a factor of 10 from point 3 to point 4. Although this analysis may not take into account all the physical details of the green body, it points out the important roles of particle-particle contacts and the localization of water. In particular, the transition to a steeper dependence of thermal conductivity on moisture content can be ascribed to the interruption of the continuous liquid phase within the ceramic green body which takes place after the end of the first falling rate.

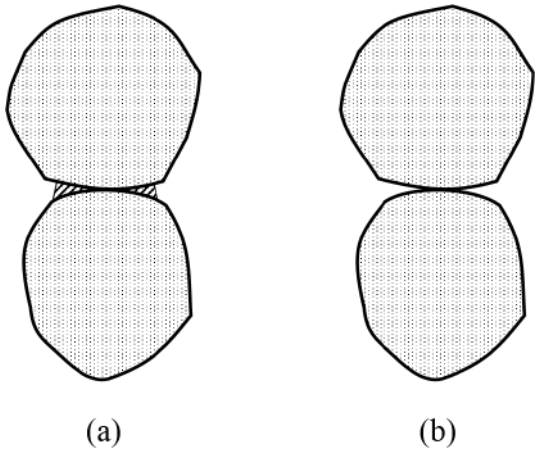

Figure 4.14: Interface between grains with (a) water located in the neck region and (b) after a complete drying. Water with a higher thermal conductivity than air decreases the thermal resistance of the interface region (contact) between grains.

4.2.2.3 Results analysis: Kaolin samples

Despite the much lower thermal conductivity of the solid phases, many aspects of the general behaviour during drying of kaolin samples are similar to alumina. Thermal conductivity and linear shrinkage as a function of weight loss are plotted in figure 4.15 for 3 sets of kaolin samples. As for alumina samples, 3 distinct regimes are observed. The situations for the two materials are compared. At the beginning of drying, the volume fractions of water in the samples are very close (53% for alumina and 51% for kaolin). Then the higher initial value of thermal conductivity for alumina samples can be easily understood by the higher value of the intrinsic conductivity of alumina (35 $W\ m^{-1}\ K^{-1}$)

compared to kaolin clay ($< 2\ W\ m^{-1}\ K^{-1}$). After a complete drying at 40 °C, we can assume that the volume fraction of water is negligible and the material is only constituted by solid and air, with pore volume fractions of 48% for alumina and 44% for kaolin. At this stage, the conductivity value for alumina sample is lower than for kaolin ($0.25\ W\ m^{-1}\ K^{-1}$ and $0.5\ W\ m^{-1}\ K^{-1}$ respectively). As stated earlier, the thermal resistance for contacts between alumina grains can be responsible for a strong decrease in the equivalent solid matrix conductivity and consequently for the low effective value. Indeed, after a complete drying, alumina grains are very weakly bound, which results in a very brittle material in comparison with clay samples which can be easily handled without damage. The greater value of conductivity in kaolin samples can then be explained by more efficient contact between clay particles compared with alumina grains.

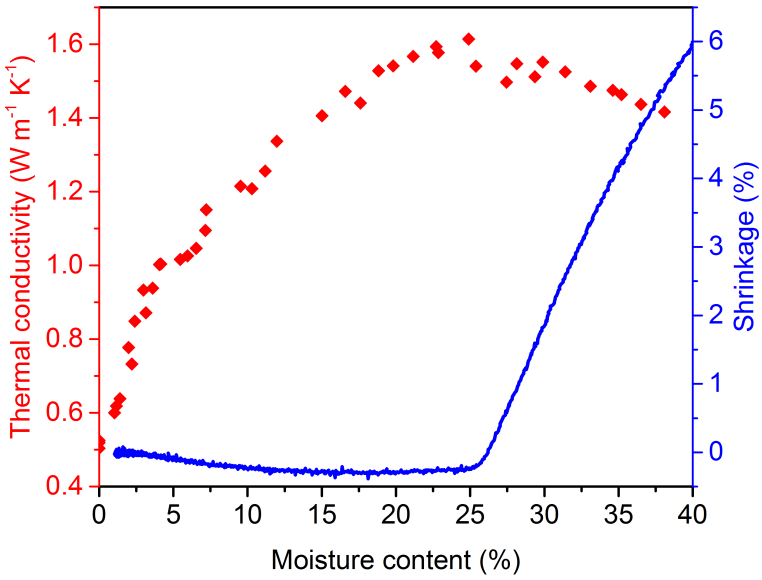

Figure 4.15: Thermal conductivity and linear shrinkage as a function of moisture content for kaolin samples.

4.3 Conclusion

This chapter has evaluated the properties involved in the heat and mass transfers for drying. These are the water activity, diffusion coefficient, heat capacity and thermal conductivity.

First, the water activity has been assessed at two drying temperatures using different atmospheres with constant relative humidity. Results have allowed us to quantify at the

end of drying the residual amount of water that remains in the samples. We have found that kaolin material is able to retain more water than alumina when they are dried under the same conditions. The water distribution profiles within green bodies during drying, obtained in chapter 3, have been used to estimate the evolution of the effective diffusion coefficient of water in the ceramic green body during drying. A strong dependence of this coefficient on moisture content has been observed. It decreases from $2.3 \times 10^{-6}\ m^2\ s^{-1}$ for ca. 22% of moisture content down to $1.4 \times 10^{-8}\ m^2\ s^{-1}$ for ca. 5%. These values are in rough agreement with values found in literature.

For the thermal properties, the heat capacity has been calculated as a function of the moisture content using the rule of mixtures. This property decreases as drying proceeds because of the high value of the water heat capacity compared to that of alumina and kaolin (more than four times higher). Finally, the thermal conductivity of alumina and kaolin has been described in detail. Results show that this property evolves strongly with the moisture content and exhibits 3 distinct regimes. First, the thermal conductivity increases at the beginning of drying and reaches a maximum value at the end of the shrinkage. Second, a decrease is observed, when water which evaporates is replaced by air. Finally, at the end of drying, the thermal conductivity strongly decreases as a function of weight loss. To a first approximation, the behaviour can be described by a simple model based on the Maxwell-Eucken relation but this does not take into account the role of grain-grain contacts. The thermal resistance for an equivalent plane of grain-grain contacts at different stages of drying was estimated using analytical relations. A strong increase in the calculated values is observed at the end of drying that we can attribute to the removal of water located next to the solid grain-grain contacts.

Chapter 5 :

Numerical model of drying and practical application

Chapter context

This final chapter presents the construction of a numerical model that is based on coupling of heat and mass transfers involved in the drying of a ceramic green body. The aim is to predict the changes of moisture content and temperature of the body enabling optimization of the drying process. In this respect, the drying problem is first described in the form of partial differential equations. Then, since heat and mass transfers involve physical properties (thermal conductivity, heat capacity, water activity and effective diffusion coefficient), their changes with water content in the green body, discussed experimentally in chapter 4, are taken into account in construction of the model. To solve the equations, the finite-element method (FEM) is used. The predictions are then tested for accuracy in comparison to experimental results.

5.1 Introduction to numerical modeling of drying

Contributions in numerical modeling to predict drying behaviour become more and more important in many industrial sectors because of the cost and time invested in experimental studies. Providing relatively precise dimensions for the green body are calculated, this approach should be a good alternative to the optimization of the drying process via trial and error [13, 70–75].

As previously stated, convective drying is the most used type of drying in the ceramic industry. It involves coupling of two types of transfer: heat transfer from the surroundings towards the moist sample and mass transfer from the sample towards its surface and then to the surrounding air. Furthermore, in most cases, drying is accompanied by shrinkage. Taking into account all the mechanisms without any simplifications in such a complex system makes finding a satisfactory solution more complicated. Therefore, most modeling works have used simplifying hypotheses such as considering the transfers in one or two dimensions and ignoring variations of physical and thermal properties during drying [70–72]. These models do not take into account the dimension changes. For example, in the case of an exposed surface to a stream of flowing air, Kaya et al. created a 2D numerical model of heat and mass transfer with variable surface transfer coefficients (heat and mass) for a rectangular moist object [70]. They predicted the more favorable aspect ratio, inlet and outlet locations of a rectangular cavity for optimum heat transfer and drying rate. Lallemant et al. used a numerical model in three dimensions to predict the drying behaviour in terms of the evaporation rate of laboratory-scaled transparent ceramic oxide samples [13]. The model was then applied to larger industrial-scaled samples in order to optimize the drying process. With similar concerns Chandra et al. chose to predict the transient temperature and moisture distribution in a rectangular moist body for convective drying [73]. In both models, shrinkage and variations of certain physical and thermal

properties are not taken into account. In another approach, Khalili et al. developed a numerical model to calculate stresses induced during shrinkage, based on the measured values of dimensions of a green clay body. Then, using this model, they predicted the occurrence of defects (deformation and cracks) [74]. Other numerical studies were made to predict values of certain physical properties during drying, for example the effective diffusion coefficient [76]. No studies to our knowledge have tackled the numerical modeling of drying with consideration of the dependence of physical properties on moisture content. Indeed, constructing a numerical model with such input can be used for a predictive control of drying which could serve in practical applications.

5.2 Mathematical description of the model and simulation

One of the most common methods to describe a physical situation such as drying of a body is the Finite Element Method (FEM) which is a numerical technique based on solution of the Partial Differential Equations (PDE). This method consists of dividing the domain where the continuous physical equations are defined into an assembly of discrete subdomains of finite elements, then approximating solutions of each partition to couple them in an overall solution. For that, an open-source computing platform named FEniCS was used to solve the PDEs using Python programming [77]. Indeed, to tackle the physical situation of drying a body with FEniCS, different steps should be followed:

1) Specify the PDEs and their boundary conditions.

2) Reformulate them into variational forms.

3) Define the input data such as the initial parameters, formulas in the variational form and the mesh for the studied domain,

4) Code the whole in Python programming language.

5) Solve the equations and output the results in the form of relevant physical parameters.

5.2.1 Definition of the problem

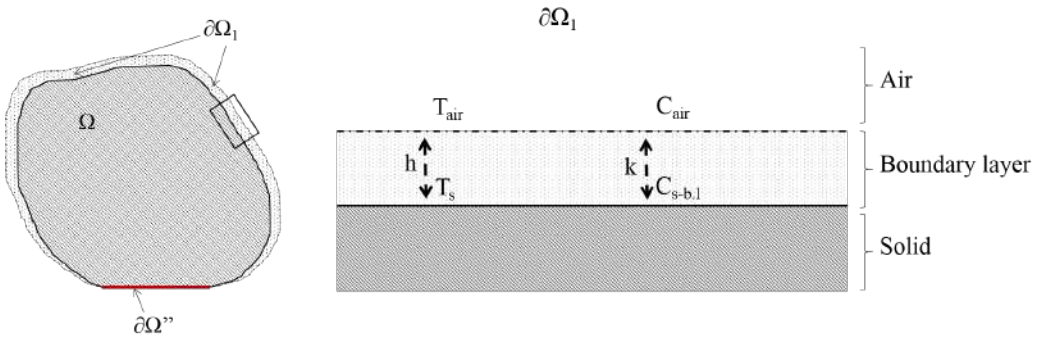

Figure 5.1: A schematic representation of heat and mass fluxes at a moist surface exposed to drying by convection.

Since taking into account all aspects involved in drying of a ceramic green body is complicated, some assumptions are made for simplification: (1) the solid is homogeneous and isotropic (2) the gravitational effect is neglected; (3) the evaporation of water takes place only at the body surface; (4) the shrinkage is neglected but its effect on the mass loss will be quantified.

Based on these assumptions, heat and mass transfers by diffusion within the porous body can then be described using the Fourier and Fick equations:

$$\begin{cases} \frac{\partial T}{\partial t} = \frac{\lambda(C)}{\rho(C)C_p(C)}\nabla^2 T & in \quad \Omega \\ \frac{\partial C}{\partial t} = D_w(C)\nabla^2 C & in \quad \Omega \end{cases} \tag{5.1}$$

where the domain Ω corresponds to the wet body, T is the body temperature in K, and C is the water concentration in $mol\ m^{-3}$. $\rho(C)$ is the density of the wet body which can be expressed as following:

$$\rho(C) = \rho_{dry-bulk} + C\ M_w \tag{5.2}$$

where $\rho_{dry-bulk}$ is the dry bulk density in $kg\ m^{-3}$, and M_w is the water molar mass in $kg\ mol^{-1}$.

The thermal conductivity $\lambda(C)$, heat capacity $C_p(C)$ and diffusion coefficient $D_w(C)$ are functions which depend on the water concentration C, following chapter 4 where we identified the dependence of these properties on the moisture content. It is worth noting that the moisture content X is related to the water concentration by the following expression:

$$X = \frac{C \times M_w}{\rho_{dry-bulk}} \tag{5.3}$$

At the body surface, the solution requires the boundary conditions corresponding to exchanges with the surrounding air. The general situation has been discussed earlier in the first chapter (1.2.3), but nevertheless the useful equations are given below.

The relations are:

$$\begin{cases} \phi_C = -k(C_{air} - C_{s-b.l}) = -k(RH\frac{P_s(T_{air})}{R\ T_{air}} - a_w(C)\frac{P_s(T_s)}{R\ T_s}) & in \quad \partial\Omega_1 \\ \phi_T = -h(T_{air} - T_s) + L_w M_w \phi_C & in \quad \partial\Omega_1 \end{cases} \tag{5.4}$$

The boundaries illustrated in figure 5.1: $\partial\Omega_1$ corresponds to the surface in contact with air and $\partial\Omega''$ concerns the isolated part (no exchanges with air) where the fluxes are assumed to be equal to zero.

5.2.2 Variational formulation

The system of equations above represents a strong formulation of the problem (coupling of the heat and mass transfers), which is assumed to be simultaneously a nonlinear and time-dependent problem. Turning this PDE problem into a weak formulation goes then through different steps developed below:

First, the equations are multiplied by the test functions T_{test} and C_{test}, which correspond to the mathematical finite element literature [77, 78]. These equations are integrated over the domain Ω, using integration by parts with the second derivatives:

$$\int_\Omega \frac{\Delta C}{dt}\ C_{test}\ dx = \int_{\partial\Omega_1} \phi_C(C)\ C_{test}\ dS - D_w(C)\int_\Omega \nabla C.\nabla C_{test}\ dx \tag{5.5}$$

$$\rho(C)\ C_p(C)\ \int_\Omega \frac{\Delta T}{dt}\ T_{test}\ dx = \int_{\partial\Omega_1} \phi_T(T)\ T_{test}\ dS - \lambda(C)\int_\Omega \nabla T.\nabla T_{test}\ dx \tag{5.6}$$

Then the time derivative of the heat and mass equations are discretized using the backward Euler method. This method has been chosen owing to its suitability with large time discretization dt which is necessary in our case because of the long duration of drying. The time derivative for concentration (C) and temperature (T) can then be approximated to the forms:

$$\frac{\Delta C_{n+1}}{dt} \approx \frac{C_{n+1} - C_n}{dt} = D_w(C_{n+1})\nabla^2 C_{n+1} \tag{5.7}$$

$$\frac{\Delta T_{n+1}}{dt} \approx \frac{T_{n+1} - T_n}{dt} = \frac{\lambda(C_{n+1})}{\rho(C_{n+1}) C_p(C_{n+1})} \nabla^2 T_{n+1} \tag{5.8}$$

where n is an integer counting time intervals, which means for example that C_n corresponds to the variable values at time interval n. Then by inserting 5.7 and 5.8 in the integrated equations 5.5 and 5.6 we obtain:

$$\int_\Omega (C_{n+1} - C_n)\, C_{test}\, dx = dt\, (\int_{\partial\Omega_1} \phi_C(C_{n+1})\, C_{test}\, dS - D_w(C_{n+1}) \int_\Omega \nabla C_{n+1}.\nabla C_{test}\, dx) \tag{5.9}$$

$$\rho(C_{n+1})\, C_p(C_{n+1}) \int_\Omega (T_{n+1} - T_n)\, T_{test}\, dx = dt\, (\int_{\partial\Omega_1} \phi_T(T_{n+1})\, T_{test}\, dS - \lambda(C_{n+1}) \int_\Omega \nabla T_{n+1}.\nabla T_{test}\, dx) \tag{5.10}$$

Finally, coupling the equations 5.9 and 5.10 yields:

$$\begin{aligned} \rho(C_{n+1})\, C_p(C_{n+1}) \int_\Omega (T_{n+1} - T_n)\, T_{test}\, dx + \int_\Omega (C_{n+1} - C_n)\, C_{test}\, dx = \\ dt\, (\int_{\partial\Omega_1} \phi_T(T_{n+1})\, T_{test}\, dS - \lambda(C_{n+1}) \int_\Omega \nabla T_{n+1}.\nabla T_{test}\, dx) \\ + dt\, (\int_{\partial\Omega_1} \phi_C(C_{n+1})\, C_{test}\, dS - D_w(C_{n+1}) \int_\Omega \nabla C_{n+1}.\nabla C_{test}\, dx) \end{aligned} \tag{5.11}$$

5.2.3 Input data used in the model

- **Values of parameters/properties used for calculations:**

Parameter	**Symbol**	**Value**	**Unit**
Water density	ρ_w	1000	$kg\ m^{-3}$
Air density	ρ_{air}	1.2	$kg\ m^{-3}$
Alumina density	ρ_{solid}	3986	$kg\ m^{-3}$
Kaolin density	ρ_{solid}	2600	$kg\ m^{-3}$
Pore volume fraction	v_p	0.5	
Dry bulk density for a given porosity	$\rho_{dry-bulk}$	$\rho_{solid}(1 - v_p)$	$kg\ m^{-3}$
Ideal gas constant	R	8.314	$J\ mol^{-1}\ K{-}1$
Water molar mass	M_w	0.018	$kg\ mol^{-1}$
Alumina heat capacity	Cp_{solid}	780	$J\ kg^{-1}\ K^{-1}$
Kaolin heat capacity	Cp_{solid}	949	$J\ kg^{-1}\ K^{-1}$
Water heat capacity	Cp_w	4180	$J\ kg^{-1}\ K^{-1}$
Air heat capacity	Cp_{air}	1000	$J\ kg^{-1}\ K^{-1}$
Lewis coefficient	L_{ef}	1	
Water vaporization latent heat [79]	$L_w(T)$	$1000(2501 - 2.43(T - 273.15))$	$J\ kg^{-1}$
Saturation vapour water pressure [79]	$P_s(T)$	$133.322\ exp(46.784 - \frac{6435}{T} - 3.868\ ln(T))$	Pa

Table 5.1: Input parameters for calculations.

Given that the model deals with various physical properties which depend on the moisture content and the distribution of water within the body during drying, these will determine final accuracy of the predictions. That is why the results obtained experimentally in chapter 4 were fitted and included as a parameter in the model. In this respect the following relations expressed in terms of the water content (X) were used.

- **Water activity:**

Experimental points of water activity were fitted using the Oswin equation which is expressed as follows [80]:

$$a_w = \frac{1}{1 + (\frac{a}{X})^b} \tag{5.12}$$

where a and b are constants determined for each material and both temperatures (figure 5.2).

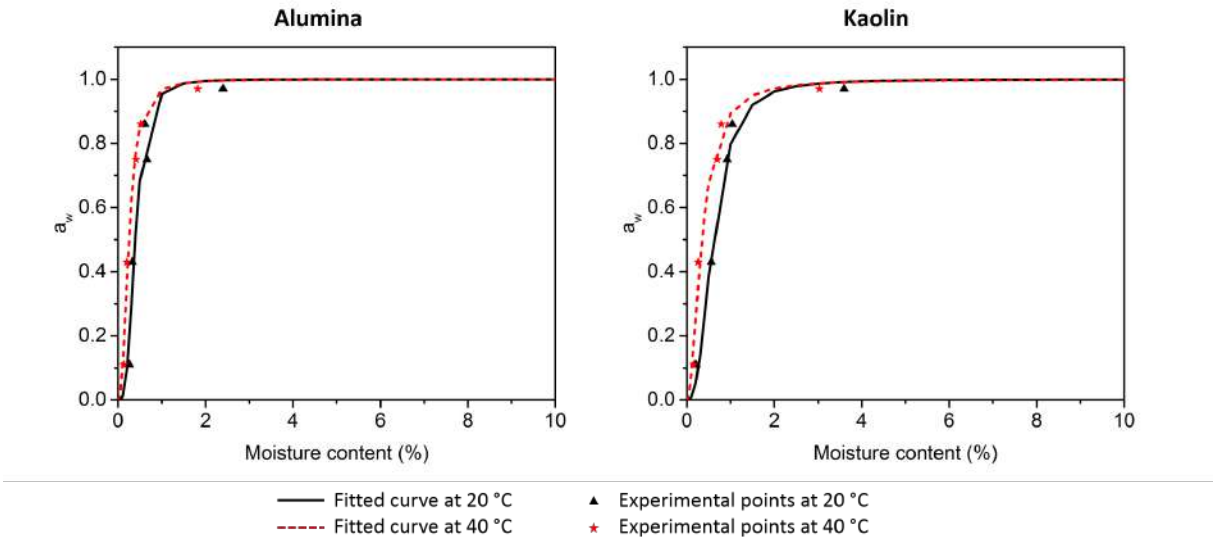

Figure 5.2: Experimental points and fitted curves of water activity as a function of moisture content for both alumina and kaolin at 20 $°C$ and 40 $°C$.

- **Effective diffusion coefficient:**

The effective moisture diffusion coefficient is a parameter that describes migration of water through the body to be evaporated at the surface. In our study, different stages can be identified related to the kinetics for transport of water yielding variation in the value of moisture diffusion coefficient. During a first period, involving shrinkage, the system is assumed to be constituted of liquid and solid. In other words there is no vapour diffusion within the body since a uniform water distribution was observed during this period in chapter 3. Thus, we can attribute a high value of the diffusion coefficient. Based on this, using the same sample dimensions and drying conditions, we reduced the diffusion coefficient value until a gradient in water concentration appeared. The last value which gives a uniform water concentration was used in the model ($6 \times 10^{-5}\ m^2\ s^{-1}$). However, when the body volume is fixed and water evaporates from the pores in the interior of the body, the distribution of water within the sample varies with position. Consequently, the process of vapour diffusion becomes limiting and the variation of D_w must be taken into account in the model. As for water activity, the experimental values of diffusivity were fitted to an analytical relation. The relationship between D_w and moisture content is of the form:

$$D_2(X) = 2 \times 10^{-9} exp(0.3X) \tag{5.13}$$

The transition between the two periods of drying is modeled by a cumulative distribution function which is related to the error function as given in equations 5.14 and

5.15. The evolution of the diffusion coefficient is shown in figure 5.3.

$$D_w(X) = D_2 + \frac{1}{2}(1 + erf(\frac{X - X_{f.p}}{dX\sqrt{2}}))(D_2 - D_1) \tag{5.14}$$

where$X_{f.p}$ is the moisture content for which the first drying period is completed, dX is the deviation, and erf is the error function which can be expressed as follows:

$$erf(x) = \frac{2}{\sqrt{\pi}} \times \int_0^x \exp(-t^2)\ dt \tag{5.15}$$

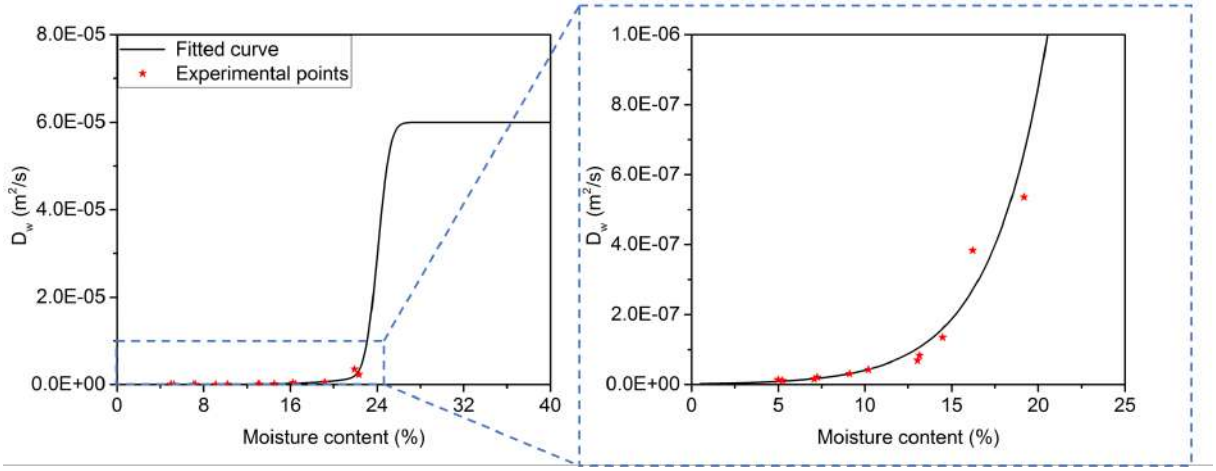

Figure 5.3: Experimental points and the fitted curve of effective diffusion coefficient as a function of moisture content for alumina. The zoom, shows the curve fitted to the experimental points using equation 5.13.

- **Thermal conductivity:**

Since experimental measurements of thermal conductivity show three distinct regimes as a function of moisture content (X), they were each fitted by using a linear equation of the form (figure 5.4):

$$\lambda = a\ X + b \tag{5.16}$$

where a and b are constants. Three sets of coefficients (a, b) were used.

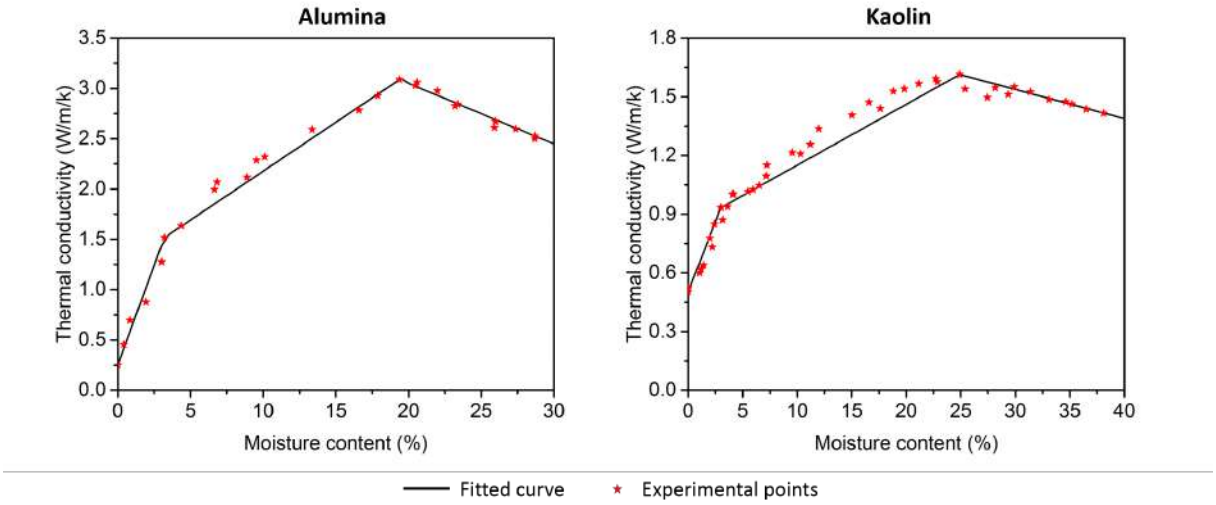

Figure 5.4: Experimental points and fitted curves of thermal conductivity as a function of moisture content for both alumina and kaolin.

Now, as the problem is established in variational form and all useful parameters have been defined, the next step in the construction of the model is to create the sample geometry. This was created and meshed using Salome software (version 7.8.0). Then equation 5.11 was solved with the Newton-Ralphson method, to take into account the non linearity. To summarize the computer simulation steps and the corresponding iterative process a schematic overview using a flowchart diagram is given in figure 5.5.

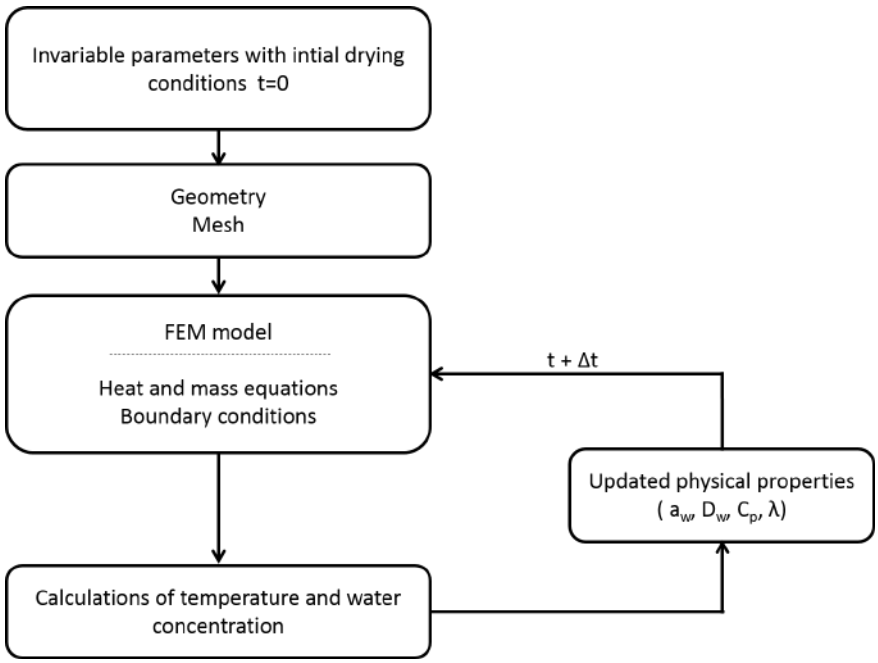

Figure 5.5: Schematic representation of the computer simulation steps of heat and mass equations.

5.3 Results

5.3.1 Model validation

Before presenting comparisons between numerical and experimental results, it is necessary to evaluate how correct is our mathematical modeling. To do that a simple situation can be assessed to predict the drying rate and surface temperature during the first stage of drying. Then, these predictions are compared with analytical results obtained by simple calculations.

For that purpose, a situation of pure convective drying where the surface temperature of the body should be the same as the wet bulb temperature of the surrounding air is considered. A geometry of 20 mm $\times$ 20 mm $\times$ 20 mm was created and a tetrahedral mesh was attributed (figure 5.6). The boundary conditions presented in equation 5.4 were applied on the 5 surfaces of the cube exposed to drying. The heat and mass fluxes were considered to be equal to zero for the bottom surface since there is no exchanges with air. Simulations were performed using a time step of $dt = 300$ s with constant values of the temperature and relative humidity as initial conditions for the calculations. The wet bulb temperature was deduced from the analytical relation 1.5 presented in chapter 1, since the relative humidity and air temperature were fixed. Then based on this temperature, the evaporation rate was calculated using equations 1.9 and 1.10. Table 5.2 summarizes the analytical results and the numerical predictions for several chosen temperatures and relative humidities. Only a small difference in calculated values between the two methods is noticed. This simple verification validates the data by numerical predictions.

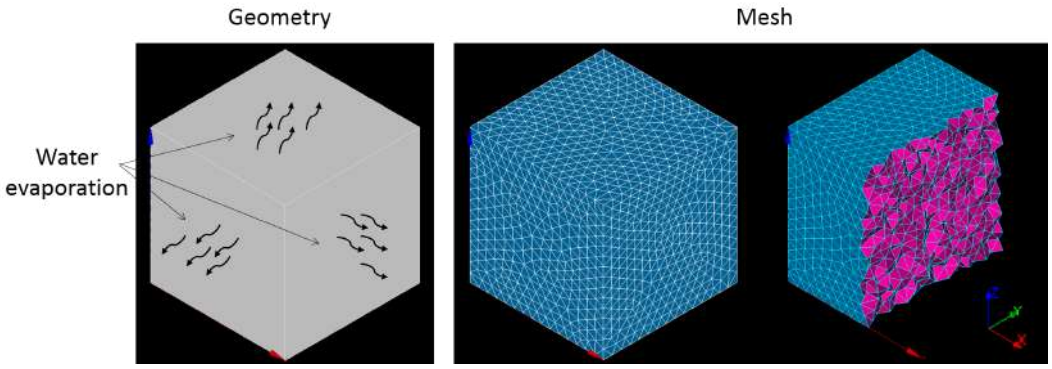

Figure 5.6: The geometry and the three dimensional mesh created with Salome-Meca software of a sample of 20 mm $\times$ 20 mm $\times$ 20 mm.

Temperature of drying ($°C$)	Relative humidity (%)	Wet bulb temperature ($°C$)	Numerical model surface temperature ($°C$)	Analytical evaporation rate ($g\ m^{-2}\ s^{-1}$)	Numerical model drying rate ($g\ m^{-2}\ s^{-1}$)
30	50	22.0	21.9	0.13	0.13
30	45	21.1	21.0	0.15	0.15
30	40	20.1	20.0	0.16	0.16
40	29	24.9	24.8	0.25	0.25
50	17	27.3	27.2	0.38	0.38

Table 5.2: Comparisons of evaporation rates and surface temperatures between analytical and numerical calculations for different temperatures and relative humidities.

5.3.2 Effect of dimensional changes on the model predictions

The numerical model as described above considers a body with invariable geometry for calculations. However, the experimental study has shown that our materials (alumina and kaolin) undergo shrinkage during drying. Thus we were interested to quantify the effect of dimensional changes on the model predictions. To this end, a verification was made by simulating in the same situation as the previous paragraph (convective drying in an environment T = 30 $°C$ and 50% relative humidity) a cubic sample that undergoes 11% of shrinkage. The choice of this value was based on the maximum shrinkage revealed in the experimental study. Two simulations were then performed. The first one corresponds to simulating a fixed geometry and in the second one the initial dimensions of the cube are reduced in several steps to 11% of shrinkage. In other words, we have divided the period for shrinkage into five intervals and during each interval the calculations are made for a new set of cube dimensions. As a result, curves observed in figure 5.7 show the moisture content as a function of time for both simulations. It can be deduced that reducing the dimensions of our geometry during drying has only a small effect on moisture content. The maximum difference reached after 8 hours of drying is approximately 1.2%. To conclude, all geometries will be invariable in the next calculations since we consider this difference as sufficiently negligible.

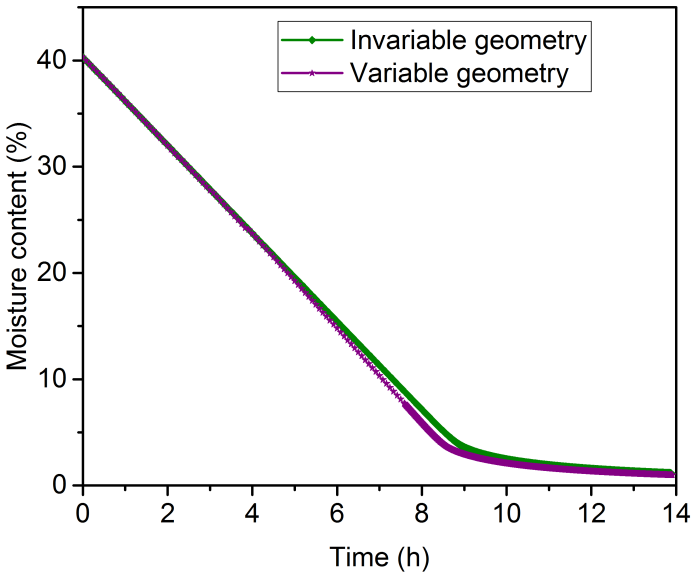

Figure 5.7: Comparison of moisture content predictions as a function of drying time for variable and invariable geometries dried in the same conditions (T = 30 $°C$ and 50%).

5.3.3 Comparisons with experimental macroscopic behaviour for alumina and kaolin

Comparisons of experimental results for the drying rate and surface temperature to numerical predictions have been made. A first simple comparison of the CRP characteristics was made with results reported in section 2.3.4. For that, a body with the same dimensions as for experiments was created virtually for calculations and the same drying conditions were applied. As an example, figure 5.8 illustrates a comparison between moisture content and surface temperature for drying kaolin at 30 $°C$ and 40%. The model presents good agreement with experimental data either in terms of moisture content or surface temperature, except for the temperatures at the beginning of drying and the changeover from the first to the second stage of drying. The first discrepancy at the beginning of drying can be related to the experimental preparation of the sample at ambient temperature (20 $°C$) before drying it at 30 $°C$ which slows down the establishment of an equilibrium. The second discrepancy can be ascribed to water transport that should be transferred in vapour form within the body in addition to liquid form at this stage. However, the evaporation in the numerical model takes place only at the surface.

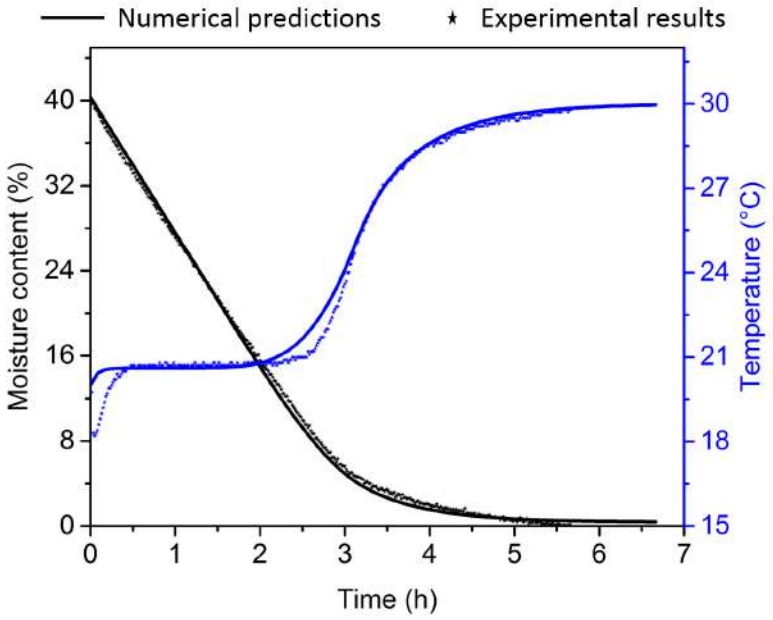

Figure 5.8: Numerical and experimental comparisons of moisture content and surface temperature as a function of drying time for kaolin sample of 20 mm × 20 mm × 20 mm. Experiments and calculations were carried out at 30 $°C$ and 40% humidity.

Further support to the graph is given by calculations of the drying rates and surface temperatures for the three drying conditions which are summarized in table 5.3. It can be concluded that the the values obtained by numerical simulations are close to experimental results.

Temperature of drying ($°C$)	Relative humidity (%)	Experimental surface temperature ($°C$)	Numerical surface temperature ($°C$)	Experimental drying rate ($g\ m^{-2}\ s^{-1}$)	Numerical drying rate ($g\ m^{-2}\ s^{-1}$)
30	40	20.7	20.0	0.15	0.16
40	29	25.1	24.8	0.23	0.24
50	17	28.9	27.2	0.34	0.37

Table 5.3: Calculations of evaporation rates and surface temperatures based on numerical predictions and experimental results for three drying conditions.

In the situation of convective drying, there is no significant difference in behaviour for alumina and kaolin green bodies. However, these two materials exhibit a difference in thermal conductivity which could play a role in drying where heat is also supplied by conduction. In such a situation, the surface temperature should lie above the wet bulb temperature during the CRP related to heat conduction through the material

controlled by its thermal conductivity. Then as the saturation vapour pressure of water increases with temperature, the concentration of water vapour in the boundary layer should increase. Consequently, the drying rate will increase too. To investigate this type of situation an experimental study was first performed with drying of alumina and kaolin samples with identical dimensions ($15\ mm\ \times\ 15\ mm\ \times\ 40\ mm$). Only one face ($15\ mm\ \times\ 15\ mm$) was exposed to drying with air at 20 $°C$. The opposite face was put on a heating plate at 50 $°C$, and the other faces were surrounded with polyvinyl film to prevent vapour loss along the bar. Therefore mass transfer takes place approximately in one dimension.

To simulate this situation, we consider in addition to boundary conditions corresponding to exchanges with air ($\partial\Omega_1$ of figure 5.9), the Dirichlet boundary condition at the surface in contact with the heating plate ($\partial\Omega_3$). This boundary is attributed with a constant to maintain surface temperature of 50 $°C$. Furthermore, to take into account the convective heat flux along the lateral surface ($\partial\Omega_2$), the boundary condition can be written in the variational form as follows and added to equation 5.11:

$$\phi = \int_{\partial\Omega_2} h(T_{n+1} - T_{air})\ T_{test}\ dS \tag{5.17}$$

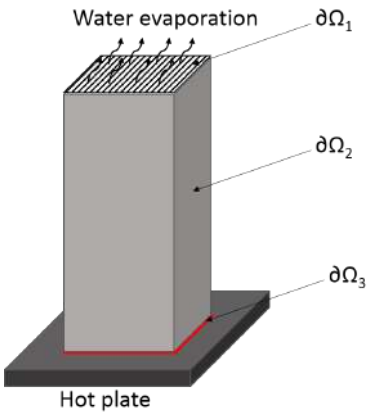

Figure 5.9: Representation of a drying experiment in air at 20 $°C$ with the sample placed on a heating plate at 50 $°C$, yielding the boundary conditions used for calculations. Only the upper surface is exposed to the drying atmosphere and the other faces are surrounded by a plastic film.

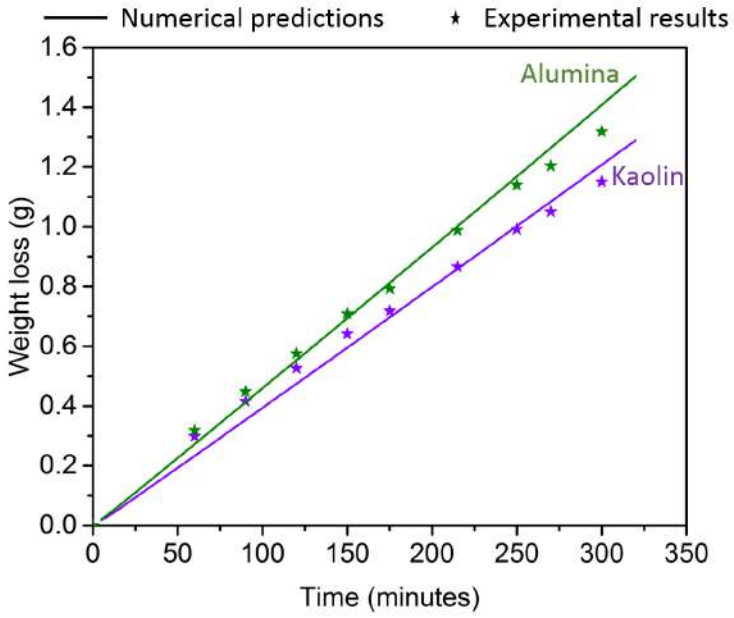

Figure 5.10: Numerical and experimental comparisons of weight loss for alumina and kaolin samples, with similar dimensions, as a function of time. In addition to drying by convection with air at 20 $°C$, samples were put on a heating plate to supply heat by conduction.

Figure 5.10 shows numerical and experimental weight loss as function of time during the CRP. Based on these results evaporation rates were calculated and are reported in table 5.4. As can be seen results are coherent for both materials. It can be noted that the evaporation rate of the alumina sample is approximately 15% higher than for kaolin. This can be explained by the contribution of heat supplied by conduction along the bar, which should be greater in alumina than kaolin related to the higher value of the thermal conductivity during the CRP. The values vary between 2.5 and 3.1 $W\ m^{-1}\ K^{-1}$ for alumina compared to 1.4 and 1.6 $W\ m^{-1}\ K^{-1}$ for kaolin. Based on the numerical predictions, the temperature at the surface exposed to drying for alumina is 4 $°C$ higher than for kaolin (21 $°C$ for alumina and 17 $°C$ for kaolin). We concluded that depending on the drying conditions, the thermal conductivity can affect the drying rate during the CRP.

	Experimental drying rate ($g\ m^{-2}\ s^{-1}$)	Numerical drying rate ($g\ m^{-2}\ s^{-1}$)
Alumina	0.31	0.34
Kaolin	0.26	0.29

Table 5.4: Calculations of drying rates for alumina and kaolin using experimental results and numerical predictions.

5.3.4 Distribution of the moisture content and temperature

In this section simulations were made with respect to experimental results of moisture distribution obtained in chapter 3. The same drying situation as section 3.1.1.1 was considered for the calculations, i.e. only one face was exposed to drying and the other faces were covered with a plastic film. An additional experimental study of the temperature distribution within the body, was performed for alumina samples exposed to drying in the same conditions. Four thermocouples were inserted in the sample at different height as can be observed in figure 5.11.

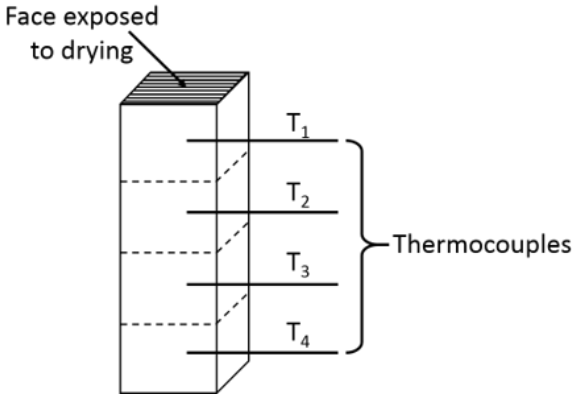

Figure 5.11: Representation of a drying experiment at 40 $°C$ with four thermocouples placed within the sample at different heights in order to record temperature evolution during drying. Only one face was exposed to drying and the other faces were surrounded by a plastic film.

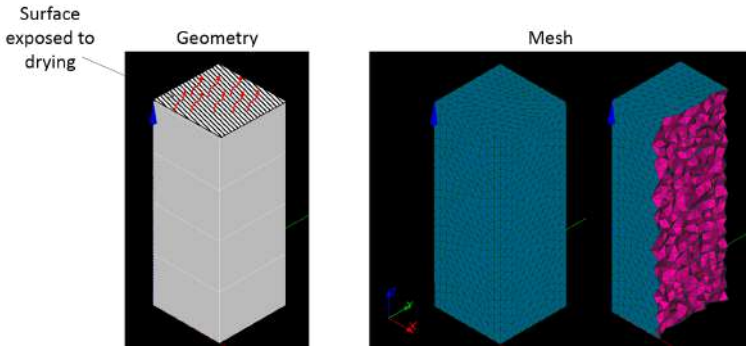

Figure 5.12: The geometry and the mesh created with Salome-Meca software of a sample with dimensions of 15 mm $\times$ 15 mm $\times$ 40 mm.

For calculations, the boundary conditions ($\partial\Omega_1$) for mass exchanges with the surrounding air were applied only on the face exposed to drying while the other faces were considered as hermetic. However equation 5.17 was added as a boundary condition ($\partial\Omega_2$) to take into account the heat exchanged with the surrounding air by convection along

the lateral surface. For the bottom surface, heat and mass fluxes were considered to be equal to zero (no exchanges with air). A geometry of 15 mm × 15 mm × 40 mm was created from 4 sub-geometries of 15 mm × 15 mm × 10 mm superimposed on each other (figure 5.12). Then this volume was meshed by three dimensional tetrahedral elements as shown in figure 5.12.

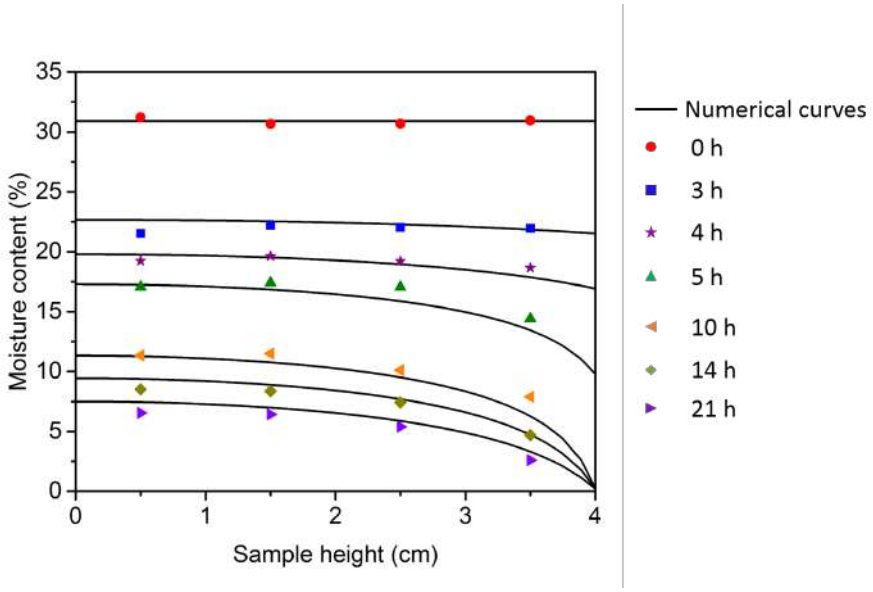

Figure 5.13: Numerical and experimental comparison of the moisture content distribution as a function of sample height for alumina, at 40 °C.

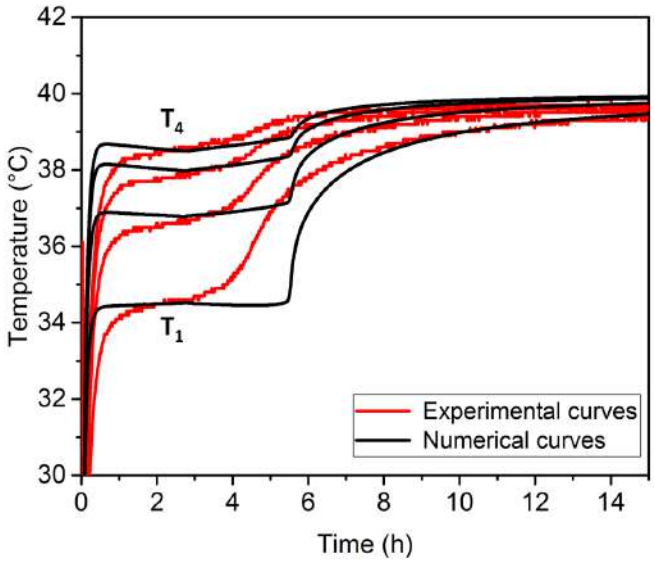

Figure 5.14: Numerical and experimental comparison of the temperature at four positions within the body as a function of drying time for alumina, at 40 °C.

Figures 5.13 and 5.14 compare the distributions of water and temperature within the alumina sample. First, the simulations show that the water distribution is uniform during the three first hours of drying which is assumed to be accompanied by shrinkage. These results are in agreement with the experimental points, since we have fixed the diffusion coefficient to get uniform concentrations. Then after 4 hours a difference in concentration as a function of position in the porous body appears. The model is able to reproduce water concentration gradients observed experimentally. On the other hand, the temperature curves show the same profile of evolution for the four thermocouples. A significant thermal gradient is revealed which transports heat to the evaporating exposed surface. All profiles maintain a constant value during approximately 4 hours which is longer than the experimental observations. Then, the temperature of the body rises to reach that of the surrounding air at the end of drying. It can also be noted that during the CRP, the temperature differences between the thermocouple positions are not constant, which means that the thermal gradient is not uniform along the z direction (height). This is explained by the heat convection exchanges with the lateral surface.

5.4 Conclusion and discussion

In this final chapter a macroscopic three dimensional numerical model has been developed in order to predict temperature and concentration in a ceramic green body. This model based on a coupling of heat and mass equations presents a simplification of the drying behaviour of such complex systems (ceramic bodies), but its strength is that the changes of the governing physical properties with moisture content are taken into account. Resolution of these equations has been made using the finite element method (FEM). First a comparison is made with analytical calculations of a simple situation of convective drying. The close agreement in values enabled us to validate the model. Then, in order to evaluate the influence of shrinkage on moisture content as drying proceeds a second comparison between predictions for variable and invariable geometry has shown a small difference. In a working approximation, this can be neglected. After these verifications, comparisons with experimental results have shown that in the case of only convective drying, the evaporation rates and surfaces temperatures during the first stage of drying (CRP) are independent of the material properties but can be controlled by drying conditions such as, temperature, relative humidity and velocity of air currents. The evaporation rate can also be increased by supplying heat through conduction in addition to convection. For this, the sample is placed on a hot plate. Furthermore, in this situation, as thermal conductivity of alumina is higher than kaolin during the CRP, the heat transfer is greater which leads to a faster drying. Finally, predictions of moisture content and temperature distributions within the body were compared to experimental studies. Providing accurate values for the diffusion coefficient are used as input data,

good predictions of moisture content distribution are achieved.

From the examination of numerous situations of drying we concluded that the proposed model has practical applications such as, determination of the time needed to dry the green body in order to reduce the energy consumption, evaluation of the influence of the process variables (drying conditions) on temperature and moisture distributions. Furthermore, monitoring parameters such as sample temperature and moisture content in real time can be a good means to assess progress in the drying step with eventual feedback in process control.

Conclusions

The drying step in fabrication of ceramic products is a complicated operation primarily due to the simultaneous heat and mass transfers involved accompanied by dimensional variation of the body. Future innovations for greater efficiency of processing could exploit a computer controlled feedback loop with input of data indicating progress of the drying step. A procedure to monitor in real time the drying parameters of sample temperature, moisture content and dimension changes was developed as well as a macroscopic numerical model. In order to refine the numerical model, studies were made of the distribution of water in the green body and the dependence of physical properties on moisture content. This approach is summarized in the following schematic presentation:

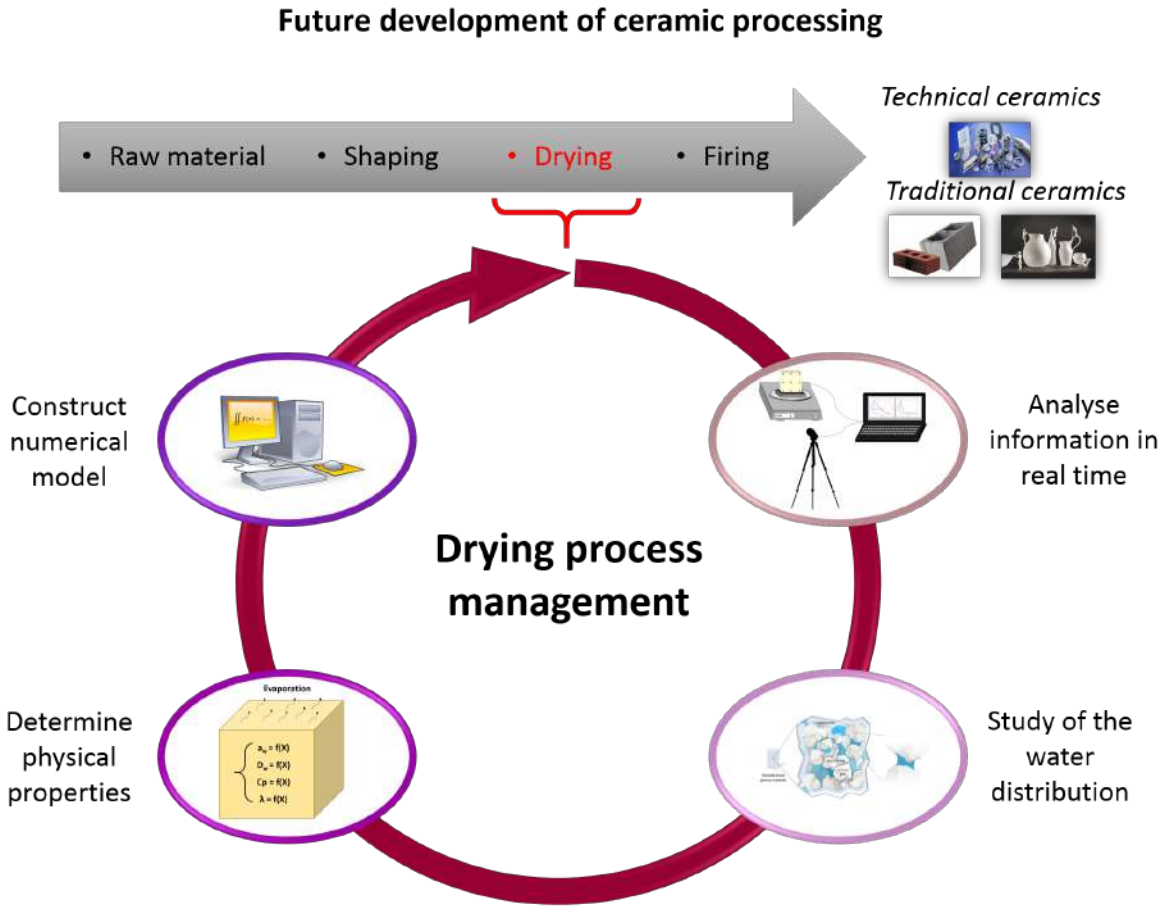

Figure 5.15: Schematic representation of this work context and the procedure followed to satisfy the main objective.

Using an experimental approach, the macroscopic drying behaviour of two different materials: alumina and kaolin was examined. First the surface temperature, the moisture content and the length changes have been monitored for similar samples in the same conditions (constant temperature and relative humidity). Results for these two materials have been analyzed in the context of the different stages of drying described in the literature. No difference related to the first stage named the CRP has been noticed.

Furthermore, the shrinkage for both materials ends during the CRP. However the second stage of drying known by the FRP takes more time in the case of kaolin clay compared to alumina. This can be related to the interactions between clay particles and water as explained in the literature by Ford [8]. In order to further investigations on this topic, the behaviour of a third material 'montmorillonite' dried in the same conditions as for alumina and kaolin has been analyzed and some differences were indeed found. In the case of montmorillonite, water interacts strongly with the particles. It is located between particles and also within the particle itself. As a consequence, transport of water out of the body during drying is more difficult. Furthermore, shrinkage can not be related in a simple way to the different stages of drying. Finally in this section, it is shown that for standard materials like alumina and kaolin the evaporation rate, especially in the first stage, is controlled by temperature and relative humidity. This will determine the duration of the drying step in an industrial process.

In order to characterize the shrinkage of ceramic pastes in different directions has been assessed in real time during drying . An optical method based on tracking of marks has been developed to measure linear shrinkage simultaneously in two dimensions. To illustrate the interest of such a method in the field of ceramics, kaolin and alumina pastes were characterized. Results obtained with this method are found to be in good agreement with those obtained with a LVDT sensor which is a one dimensional method. We have shown that pressing or extruding a ceramic paste could lead to strong anisotropic shrinkage. For instance, the overall shrinkage of kaolin, obtained by pressing or by extrusion, can be 1.8 times greater depending on the direction, while for alumina it is significantly less. The anisotropic shrinkage is related to the orientation and morphology of anisometric grains inducing a larger water/solid ratio along one direction compared to the other directions.

Following the investigation of the macroscopic drying behaviour of alumina and kaolin, we then examined the spatial distributions of water within the green body at different scales during drying. This work brings new information but basically confirms the general picture of drying established in the literature. For "slow" drying corresponding to removal of water by natural convection, during the first stage involving shrinkage, the distribution of water in the ceramic body is uniform. Then during the second stage of drying, when the body volume is fixed and water evaporates from the pores in the interior of the body, the distribution of water within the sample varies with position. A gradient in water concentration is revealed between emptied zones next to the drying surface and the body interior where water is removed more slowly. ESEM observations show at the grain scale that the water starts to empty from the larger pores first and that the smaller pores empty later on during the drying process. Then in the final stage of drying,

the residual water is localized in the zones next to the solid–solid contacts between particles. This information helps to explain how physical properties vary with moisture content, particularly the effective thermal conductivity and the water diffusion coefficient.

The properties involved in the heat and mass transfers for drying including water activity, water diffusion coefficient, heat capacity and thermal conductivity were examined. First, the water activity has been assessed at two drying temperatures using different atmospheres with constant relative humidity. Then the effective diffusion coefficient of water was estimated from macroscopic weight measurement during drying. A strong dependence of this coefficient on moisture content has been observed. It decreases from $2.3 \times 10^{-6}\ m^2\ s^{-1}$ for ca. 22% of moisture content down to $1.4 \times 10^{-8}\ m^2\ s^{-1}$ for ca. 5%. These values are in rough agreement with values found in literature.

For the thermal properties, the heat capacity has been calculated as a function of the moisture content using the rule of mixtures. This property decreases as drying proceeds because of the high value of the water heat capacity compared to that of alumina and kaolin (more than four times higher). Finally, the thermal conductivity of alumina and kaolin has been described in detail. Results show that this property evolves strongly with the moisture content and exhibits 3 distinct regimes. First, the thermal conductivity increases at the beginning of drying and reaches a maximum value at the end of the shrinkage. Second, a decrease is observed, when water which evaporates is replaced by air. Finally, at the end of drying, the thermal conductivity strongly decreases as a function of weight loss. To a first approximation, the behaviour can be described by a simple model based on the Maxwell-Eucken relation but this does not take into account the role of grain-grain contacts. The thermal resistance for an equivalent plane of grain-grain contacts at different stages of drying was estimated using analytical relations. A strong increase in the calculated values is observed at the end of drying that we can attribute to the removal of water located next to the solid grain-grain contacts.

Finally, a macroscopic three dimensional numerical model has been developed in order to predict temperature and concentration in a ceramic green body. This model based on a coupling of heat and mass equations presents a simplification of the drying behaviour of such complex systems (ceramic bodies), but its strength is that the changes of the governing physical properties with moisture content are taken into account. Resolution of these equations has been made using the finite element method (FEM). Before investigating comparisons with experimental studies on kaolin and alumina samples, verification of the reliability of predictions was made. First a comparison is made with analytical calculations of a simple situation of convective drying. The close agreement in values enabled us to validate the model. Then, in order to evaluate the

influence of shrinkage on moisture content as drying proceeds a second comparison between predictions for variable and invariable geometry has shown a small difference. In a working approximation, this can be neglected. After these verifications, comparisons with experimental results have shown that in the case of only convective drying, the evaporation rates and surfaces temperatures during the first stage of drying (CRP) are independent of the material properties but can be controlled by drying conditions such as, temperature, relative humidity and velocity of air currents. The evaporation rate can also be increased by supplying heat through conduction in addition to convection. For this, the sample is placed on a hot plate. Furthermore, in this situation, as thermal conductivity of alumina is higher than kaolin during the CRP, the heat transfer is greater which leads to a faster drying. Finally, predictions of moisture content and temperature distributions within the body were compared to experimental studies. Providing accurate values for the diffusion coefficient are used as input data, good predictions of moisture content distribution are achieved.

From the examination of numerous situations of drying we concluded that the proposed model has practical applications such as, determination of the time needed to dry the green body in order to reduce the energy consumption, evaluation of the influence of the process variables (drying conditions) on temperature and moisture distributions. Furthermore, monitoring parameters such as sample temperature and moisture content in real time can be a good means to assess progress in the drying step with eventual feedback in process control.

Bibliography

[1] C. Strumillo, P.L. Jones, and Romuald Żyłła. Energy Aspects in Drying. *Handbook of Industrial Drying*, pages 1075–1101, July 2014.

[2] *Loi n 2015-992 du 17 août 2015 relative à la transition énergétique pour la croissance verte*. August 2015.

[3] Michel Kornmann. *Matériaux de construction en terre cuite, fabrication et propriétés*. March 2005.

[4] J. Kiennemann. *Comportement dans l'eau d'alumines issues du procédé Bayer : Application au coulage en bande en milieu aqueux*. thesis, Université de Limoges, Limoges, 2004.

[5] Andreas Heunisch, Armin Dellert, and Andreas Roosen. Effect of powder, binder and process parameters on anisotropic shrinkage in tape cast ceramic products. *Journal of the European Ceramic Society*, 30(16):3397–3406, December 2010.

[6] Georg Besendörfer and Andreas Roosen. Particle Shape and Size Effects on Anisotropic Shrinkage in Tape-Cast Ceramic Layers. *Journal of the American Ceramic Society*, 91(8):2514–2520, 2008.

[7] Denis A. Brosnan and Gilbert C. Robinson. *Introduction to Drying of Ceramics: With Laboratory Exercises*. Wiley-American Ceramic Society, Westerville, OH, 1 edition edition, June 2003.

[8] R. W. Ford. *Ceramics Drying*. Pergamon Press, 1986.

[9] O O. Parish and T W. Putnam. Equations for the determination of humidity from dewpoint and psychrometric data. *NASA Tech. Note*, D-8401, February 1977.

[10] Jean Vasseur. Séchage convectif par air chaud, par entraînement. *Techniques de l'Ingénieur*.

[11] George W. Scherer. Theory of Drying. *Journal of the American Ceramic Society*, 73(1):3–14, January 1990.

[12] Frank P. Incropera, David P. Dewitt, Theodore P. Bergman, and Adrienne S. Lavine, editors. *Fundamentals of Heat and Mass Transfer*. Sixth edition edition.

[13] Lucile Lallemant, Johan Petit, Sylvie Lalanne, Stéphane Landais, Sandrine Trombert, Laura Vernhet, and Rémi Viroulaud. Modeling of the green body drying step to obtain large size transparent magnesium-aluminate spinel samples. *Journal of the European Ceramic Society*, 34(3):791–799, March 2014.

[14] Johannes C. Kloppers and Detlev G. Kröger. The Lewis factor and its influence on the performance prediction of wet-cooling towers. *International Journal of Thermal Sciences*, 44(9):879–884, September 2005.

[15] Uta Telljohann, Karsten Junge, and Eckehard Specht. Moisture Diffusion Coefficients for Modeling the First and Second Drying Sections of Green Bricks. *Drying Technology*, 26(7):855–863, July 2008.

[16] A. J. J. van der Zanden and M. H. de Wit. A Procedure to Measure the Diffusion Coefficient of Water in Brick as a Function of the Water Concentration. *Drying Technology*, 30(5):526–534, April 2012.

[17] Oistein Johansen. Thermal Conductivity of Soils. page 322, July 1977.

[18] Kathleen Smits, Toshihiro Sakaki, Anuchit Limsuwat, and T Illangasekare. Thermal Conductivity of Sands under Varying Moisture and Porosity in Drainage–Wetting Cycles. *Vadose Zone Journal - VADOSE ZONE J*, 9, February 2010.

[19] Anh-Minh Tang, Yu-Jun Cui, and Trung Tinh Le. A study on the thermal conductivity of compacted bentonites. *Applied Clay Science*, 41, December 2008.

[20] B. Nait-Ali, C. Danglade, D. S. Smith, and K. Haberko. Effect of humidity on the thermal conductivity of porous zirconia ceramics. *Journal of the European Ceramic Society*, 33(13):2565–2571, November 2013.

[21] Fuguo Tong, Lanru Jing, and Robert W. Zimmerman. An effective thermal conductivity model of geological porous media for coupled thermo-hydro-mechanical systems with multiphase flow. *International Journal of Rock Mechanics and Mining Sciences*, 46(8):1358–1369, December 2009.

[22] T. K. Sherwood. The Drying of Solids—I. *Industrial & Engineering Chemistry*, 21(1):12–16, January 1929.

[23] T. K. Sherwood. The Drying of solids—II. *Industrial & Engineering Chemistry*, 21(10):976–980, October 1929.

[24] T. K. Sherwood. The Drying of Solids—III1 Mechanism of the Drying of Pulp and Paper. *Industrial & Engineering Chemistry*, 22(2):132–136, February 1930.

[25] P. Munier and J. Gérard-Hirne. La représentation graphique de la relation entre le retrait et l'humidité au cours du séchage des pâtes céramiques. *Bulletin de la Société Française de Céramique*, (25):3–10, 1954.

[26] G Tarı, J. M. F Ferreira, and O Lyckfeldt. Influence of the stabilising mechanism and solid loading on slip casting of alumina. *Journal of the European Ceramic Society*, 18(5):479–486, May 1998.

[27] F. Pardo, M. M. Jordan, and M. A. Montero. Ceramic behaviour of clays in Central Chile. *Applied Clay Science*, 157:158–164, June 2018.

[28] S. de Miranda, L. Patruno, M. Ricci, R. Saponelli, and F. Ubertini. Ceramic sanitary wares: Prediction of the deformed shape after the production process. *Journal of Materials Processing Technology*, 215:309–319, January 2015.

[29] A. Bigot. Retrait au séchage des kaolins et des argiles. *Comptes rendus de l'Académie des Sciences*, pages 755–758, March 1921.

[30] W. D. Kingery and J. Francl. Fundamental Study of Clay: XIII, Drying Behavior and Plastic Properties. *Journal of the American Ceramic Society*, 37(12):596–602, 1954.

[31] Michel Kornmann. Complementary explanation of the Bigot' curve. pages 44–53, March 2006.

[32] Ebru Mancuhan, Selin Özen, Perviz Sayan, and Sibel Titiz Sargut. Experimental investigation of green brick shrinkage behavior with Bigot's curves. *Drying Technology*, 34(13):1535–1545, October 2016.

[33] Lei Xu, Simon Davies, Andrew B. Schofield, and David A. Weitz. Dynamics of drying in 3d porous media. *Physical Review Letters*, 101(9):094502, August 2008.

[34] Igor V. Koptyug. MRI of mass transport in porous media: drying and sorption processes. *Progress in Nuclear Magnetic Resonance Spectroscopy*, 65:1–65, 2011.

[35] Michel Kornmann. Matériaux de terre cuite - Matières de base et fabrication. *Techniques de l'ingénieur*, 2009.

[36] Lucien ALVISET. Matériaux de terre cuite. *Techniques de l'ingénieur*, May 1994.

[37] David Fuks, Gennady E. Shter, Meirav Mann–Lahav, and Gideon S. Grader. Crack-Free Drying of Ceramic Foams by the Use of Viscous Cosolvents. *Journal of the American Ceramic Society*, 93(11):3632–3636, 2010.

[38] J. P Jan, S Steinemann, and P Dinichert. The density and lattice parameters of ruby. *Journal of Physics and Chemistry of Solids*, 12:349–350, 1960.

[39] Fayza Bennadji-Gridi, Agnès Smith, and Jean-Pierre Bonnet. Montmorillonite based artificial nacre prepared via a drying process. *Materials Science and Engineering: B*, 130(1):132–136, June 2006.

[40] Emiel J. M. Hensen and Berend Smit. Why Clays Swell. *The Journal of Physical Chemistry B*, 106(49):12664–12667, December 2002.

[41] Mutsumi Suzuki and Siro Maeda. On the Mechanism of Drying of Granular Beds. *Journal of Chemical Engineering of Japan*, 1(1):26–31, 1968.

[42] D. M. Worrall. *Clays and Ceramic Raw Materials*. 1986.

[43] N. Bretagne, V. Valle, and J. C. Dupré. Development of the marks tracking technique for strain field and volume variation measurements. *NDT and E International*, 4(38):290–298, 2005.

[44] Chao-Sheng Tang, Bin Shi, Chun Liu, Wen-Bin Suo, and Lei Gao. Experimental characterization of shrinkage and desiccation cracking in thin clay layer. *Applied Clay Science*, 52(1):69–77, April 2011.

[45] F Yılmaztürk, S Kulur, and Bekir Pekmezci. Measurement of shrinkage in concrete samples by using digital photogrammetric methods. *The International Archives of the Photogrammtry, Remote Sensing and Spatial Information Sciences*, 34, January 2004.

[46] S. Hafner. Fast imaging in liquids and solids with the Back-projection Low Angle ShoT (BLAST) technique. *Magnetic Resonance Imaging*, 12(7):1047–1051, 1994.

[47] M. Weiger, K. P. Pruessmann, and F. Hennel. MRI with zero echo time: hard versus sweep pulse excitation. *Magnetic Resonance in Medicine*, 66(2):379–389, August 2011.

[48] M. Weiger and K. P. Pruessmann. MRI with Zero Echo Time. In *eMagRes*. American Cancer Society, 2012.

[49] W. Dreher, I. Bardenhagen, L. Huang, and M. Bäumer. On the suppression of background signals originating from NMR hardware components. Application to zero echo time imaging and relaxation time analysis. *Magnetic Resonance Imaging*, 34(3):264–270, April 2016.

[50] M. A. Bernstein, K. F. King, and X. J. Zhou. *Handbook of MRI Pulse Sequences*, volume Chapter 13.2 (gridding reconstruction). Elsevier Academic Press, 2004.

[51] J. M. Pauly. Gridding & the NUFFT for Non-Cartesian Image Reconstruction. *In: Proceedings of the 21st Annual Meeting of ISMRM, Salt LakeCity*, Utah:45, 2013.

[52] S. Hayashi, T. Ueda, K. Hayamizu, and E. Akiba. NMR study of kaolinite. 1. Silicon-29, aluminum-27, and proton spectra. *The Journal of Physical Chemistry*, 96(26):10922–10928, December 1992.

[53] Stéphane Poyet. Experimental investigation of the effect of temperature on the first desorption isotherm of concrete. *Cement and Concrete Research*, 39(11):1052–1059, November 2009.

[54] R. Moreira, F. Chenlo, M. D. Torres, and D. M. Prieto. Water adsorption and desorption isotherms of chestnut and wheat flours. *Industrial Crops and Products*, 32(3):252–257, November 2010.

[55] Lewis Greenspan. Humidity fixed points of binary saturated aqueous solutions. *Journal of research of the National Bureau of Standards. A, Physics and chemistry*, page 1, 1977.

[56] Zdeněk P. Bažant and Werapol Thonguthai. Pore Pressure and Drying of Concrete at High Temperature. *Journal of the Engineering Mechanics Division*, 104(5):1059–1079, 1978.

[57] J. Philibert. *Atom movements diffusion and mass transport in solids*. EDP Sciences, Les Ulis, France, 1995.

[58] Ottmar Knacke, Oswald Kubaschewski, and Klaus Hesselmann. *Thermochemical properties of inorganic substances*. Springer-Verlag, 1991.

[59] Aurélie Michot. *Caractéristiques thermophysiques de matériaux à base d'argile : évolution avec des traitements thermiques jusqu'à 1400C*. PhD Thesis, 2008.

[60] Silas E. Gustafsson. Transient plane source techniques for thermal conductivity and thermal diffusivity measurements of solid materials. *Review of Scientific Instruments*, 62(3):797–804, 1991.

[61] James Clerk Maxwell. *A treatise on electricity and magnetism*. Clarendon Press, Oxford, 1892.

[62] Z. Hashin and S. Shtrikman. A Variational Approach to the Theory of the Effective Magnetic Permeability of Multiphase Materials. *Journal of Applied Physics*, 33(10):3125–3131, 1962.

[63] David S. Smith, Sylvain Fayette, Sylvie Grandjean, Christian Martin, Rainer Telle, and Thorsten Tonnessen. Thermal Resistance of Grain Boundaries in Alumina Ceramics and Refractories. *Journal of the American Ceramic Society*, 86(1):105–111, 2003.

[64] *Revised release on the iaps formulation 1985 for the thermal conductivity of ordinary water substance*. September 2008.

[65] P. G. Collishaw and J. R. G. Evans. An assessment of expressions for the apparent thermal conductivity of cellular materials. *Journal of Materials Science*, 29(2):486–498, 1994.

[66] Efim Litovsky, Michael Shapiro, and Arthur Shavit. Gas Pressure and Temperature Dependences of Thermal Conductivity of Porous Ceramic Materials: Part 2, Refractories and Ceramics with Porosity Exceeding 30%. *Journal of the American Ceramic Society*, 79(5):1366–1376, 1996.

[67] Rolf Landauer. The Electrical Resistance of Binary Metallic Mixtures. *Journal of Applied Physics*, 23(7):779–784, 1952.

[68] James K. Carson, Simon J. Lovatt, David J. Tanner, and Andrew C. Cleland. Thermal conductivity bounds for isotropic, porous materials. *International Journal of Heat and Mass Transfer*, 48(11):2150–2158, 2005.

[69] Mouna Jabli Zouaoui, Benoit Nait-Ali, Nicolas Glandut, and David S. Smith. Effect of humidity on the dielectric constant and electrical impedance of mesoporous zirconia ceramics. *Journal of the European Ceramic Society*, 36(1):163–169, 2016.

[70] Ahmet Kaya, Orhan Aydın, and Ibrahim Dincer. Numerical modeling of heat and mass transfer during forced convection drying of rectangular moist objects. *International Journal of Heat and Mass Transfer*, 49(17):3094–3103, August 2006.

[71] Masoud Jabbari and Jesper Hattel. Modeling coupled heat and mass transfer during drying in tape casting with a simple ceramics–water system. *Drying Technology*, 34(2):244–253, January 2016.

[72] Ahmet Kaya, Orhan Aydın, and Ibrahim Dincer. Heat and Mass Transfer Modeling of Recirculating Flows During Air Drying of Moist Objects for Various Dryer Configurations. *Numerical Heat Transfer, Part A: Applications*, 53(1):18–34, October 2007.

[73] V. P. Chandra Mohan and Prabal Talukdar. Three dimensional numerical modeling of simultaneous heat and moisture transfer in a moist object subjected to convective drying. *International Journal of Heat and Mass Transfer*, 53(21):4638–4650, October 2010.

[74] K. Khalili, M. Bagherian, and S. Khisheh. Numerical Simulation of Drying Ceramic Using Finite Element and Machine Vision. *Procedia Technology*, 12:388–393, January 2014.

[75] N. Wang and J. G. Brennan. A mathematical model of simultaneous heat and moisture transfer during drying of potato. *Journal of Food Engineering*, 24(1):47–60, January 1995.

[76] Miloš Vasić, Željko Grbavčić, and Zagorka Radojević. Determination of the moisture diffusivity coefficient and mathematical modeling of drying. *Chemical Engineering and Processing: Process Intensification*, 76:33–44, February 2014.

[77] Garth. Wells Wells, Kent-Andre Mardal, and Anders Logg, editors. *Automated Solution of Differential Equations by the Finite Element Method - The FEniCS Book*.

[78] Susanne Brenner and Ridgway Scott. *The Mathematical Theory of Finite Element Methods*. Texts in Applied Mathematics. Springer-Verlag, New York, 3 edition, 2008.

[79] Yves Jannot. *L'air humide*.

[80] C. R. Oswin. The kinetics of package life. III. The isotherm. *Journal of the Society of Chemical Industry*, 65(12):419–421, 1946.